

PLASMA-ASSISTED COMBUSTION IN A SUPERSONIC FLOW

**A DISSERTATION
SUBMITTED TO THE DEPARTMENT OF MECHANICAL
ENGINEERING
AND THE COMMITTEE ON GRADUATE STUDIES
OF STANFORD UNIVERSITY
IN PARTIAL FULFILLMENT OF THE REQUIREMENTS
FOR THE DEGREE OF
DOCTOR OF PHILOSOPHY**

Hyungrok Do

May 2009

UMI Number: 3363959

Copyright 2009 by
Do, Hyungrok

INFORMATION TO USERS

The quality of this reproduction is dependent upon the quality of the copy submitted. Broken or indistinct print, colored or poor quality illustrations and photographs, print bleed-through, substandard margins, and improper alignment can adversely affect reproduction.

In the unlikely event that the author did not send a complete manuscript and there are missing pages, these will be noted. Also, if unauthorized copyright material had to be removed, a note will indicate the deletion.

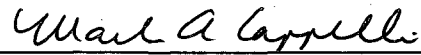
UMI[®]

UMI Microform 3363959
Copyright 2009 by ProQuest LLC
All rights reserved. This microform edition is protected against
unauthorized copying under Title 17, United States Code.

ProQuest LLC
789 East Eisenhower Parkway
P.O. Box 1346
Ann Arbor, MI 48106-1346

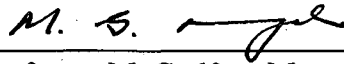
© Copyright by Hyungrok Do 2009
All Rights Reserved

I certify that I have read this dissertation and that, in my opinion, it is fully adequate in scope and quality as a dissertation for the degree of Doctor of Philosophy.



Professor Mark A. Cappelli
Doctoral Dissertation Advisor

I certify that I have read this dissertation and that, in my opinion, it is fully adequate in scope and quality as a dissertation for the degree of Doctor of Philosophy.



Professor M. Godfrey Mungal
Co-Advisor

I certify that I have read this dissertation and that, in my opinion, it is fully adequate in scope and quality as a dissertation for the degree of Doctor of Philosophy.



Professor Ronald K. Hanson

Approved for the Stanford University Committee on Graduate Studies.



Abstract

In this study, a nanosecond pulsed plasma discharge is used to ignite jet flames (hydrogen and ethylene) in supersonic crossflows. The nonequilibrium plasma is produced by repetitive pulses of 15 kV peak voltage, 20 ns pulse width and 50 kHz repetition rate. Sonic or subsonic fuel jets are injected into an air or a pure oxygen supersonic free stream flow of Mach numbers $Ma = 1.7$ to $Ma = 3.0$. The flow pattern and shockwaves, induced by the fuel jets and flow disturbances originating from the surface geometric alterations of the test model are characterized by Schlieren imaging. Planar laser induced fluorescence and emission spectroscopy are employed for imaging the distribution of OH radicals depicting fuel/oxidizer reaction regions.

Two geometric configurations of the test model are utilized with the application of the pulsed plasma, which are a cavity model and a flat wall model. The cavity provides a recirculation region where cavity flames are ignited and sustained. The cavity flame is found to be enhanced by the application of the pulsed plasma in the cavity. An investigation of the time evolution of the cavity flame reveals that the flame enhancement is primarily caused by the reduction of ignition delay time by the plasma. In the flat wall model experiment, the fuel injection nozzles and electrodes are mounted flush with the surface of a flat wall, oriented to be parallel to the flow to minimize stagnation pressure losses associated with generated shockwaves. A configuration combining an upstream subsonic oblique jet and a downstream sonic transverse jet is shown to provide an adequate flow condition for jet flame ignition. The OH fluorescence images of the region in the vicinity of the discharge confirms jet flame ignition by the plasma. Similar trends are observed in both of hydrogen and ethylene fuel injection experiments with the two test models.

The experimental results with the hydrogen fuel jets are validated using a numerical approach. The pulsed plasma is modeled as a radical source providing radicals to a flammable gas mixture periodically. The reactions following the radical production are simulated by a MATLAB based code, Cantera. The reduction of the ignition delay and the jet flame ignition by the plasma on the flat wall are successfully

validated by the method. In addition, the effects of the plasma operation conditions (e.g., plasma power and frequency) are investigated. The results suggest that higher plasma power further reduces the ignition delay time and the radical production by the pulsed plasma of a fixed power varies inversely or proportionally with the plasma frequency depending on the initial temperature of gas mixture.

Table of Contents

Abstract.....	iv
Table of Contents	vi
List of Tables.....	ix
List of Captions	x
Chapter 1 Introduction	1
1.1. Motivation	1
1.2. Background.....	6
1.2.1. Nonequilibrium Pulsed Plasma	6
1.2.2. Flame Stabilization Using Nonequilibrium Plasma	11
1.2.3. Flame Stabilization in Supersonic Flows	13
1.3. Aims and Scope	15
Chapter 2 Experimental Setup	17
2.1. Expansion Tube	17
2.1.1. Expansion Tube Body	19
2.1.2. Control System	20
2.1.3. Operation	22
2.2. Jet in Crossflow Model.....	24
2.2.1. Cavity Model	25
2.2.2. Flat Plate Model	27
2.2.3. Fuel Delivery System	28
2.3. Plasma Generation System.....	32
2.4. Synchronization System	33
2.5. OH PLIF/Emission Spectroscopy System.....	35
2.6. Schlieren System	36
Chapter 3 Plasma Assisted Cavity Flame Stabilization	39
3.1. Application of a Pulsed Plasma in a Cavity	39
3.2. Oblique Fuel Jet Injection	40
3.2.1. Development of a Sonic Jet.....	40

3.2.2. Jet Injection into a Supersonic Crossflow	41
3.3. Jet Flame Ignition in a Cavity	43
3.3.1. Auto Ignition	43
3.3.2. Ignition Delay of a Cavity Flame	45
3.4. Plasma Effect on a Cavity Flame	47
3.4.1. Cavity Flame Enhancement by a Pulsed Plasma Discharge	47
3.4.2. Reduction of Ignition Delay Time	49
3.4.3. Ethylene Jet Flame Ignition	51
3.5. Effects of Jet Injection Momentum	52
3.5.1. Jet Penetration	53
3.5.2. Effects on Cavity Flames	54
3.6. Drawbacks of Cavity Flame Stabilization Methods	55
3.6.1. Stagnation Pressure Loss	56
3.6.2. Localized Plasma Effect	56
3.7. Summary	57
Chapter 4 Plasma Assisted Flame Stabilization on a Flat Wall	59
4.1. Flat Wall Flame Stabilization	59
4.2. Single Fuel Jet Injection	61
4.3. Dual Fuel Jet Injection	63
4.3.1. Subsonic Oblique Upstream Jet	64
4.3.2. Sonic Transverse Downstream Jet	64
4.3.3. Plasma Application between the Two Jets	66
4.3.4. Plasma Ignited Upstream Jet Flame	69
4.3.5. Ignition of Downstream Jet Flame	70
4.3.6. Sustainability of Plasma Assisted Flame	73
4.3.7. Ethylene Jet Flame Ignition	75
4.4. Summary	76
Chapter 5 Modeling and Simulation	79
5.1. Modeling of the Pulsed Plasma	80
5.1.1. Assumptions	81

5.1.2. Electron Energy Distribution Function	82
5.1.3. Initial Yield of Dissociated Species	83
5.2. Reaction Kinetics Calculation	84
5.3. Perfectly Stirred Reactor with Pulsed Plasma	85
5.3.1. Assumptions and Simulation Procedure.....	85
5.3.2. Effect on Ignition Delay	86
5.3.3. Effect of Plasma Power	90
5.3.4. Effect of Plasma Frequency.....	91
5.4. Modeling of Dual Fuel Jet Injection.....	98
5.4.1. Assumptions and Simulation Procedure.....	98
5.4.2. Ignition of the Pilot Flame by the Pulsed Plasma.....	100
5.4.3. Ignition of the Downstream Jet Flame by the Pilot Flame.....	103
5.4.4. Effect of Heat Addition	104
5.5. Summary.....	106
Chapter 6 Conclusions	109
6.1. Experimental Results.....	109
6.1.1. Cavity Flame Stabilization	109
6.1.2. Flat Wall Flame Stabilization.....	110
6.2. Modeling and Simulation Results.....	111
6.3. Recommendations for Future Research.....	113
Appendix A High Speed Switch Circuit	116
A.1. Field-Effect Transistor (FET).....	116
A.2. High Speed Switch Circuit	117
Appendix B Nanosecond Pulse Generator.....	119
Appendix C Electromagnetic Interference Shielding	120
List of References.....	122

List of Tables

<i>Number</i>	<i>Page</i>
Table 2.1 Conditions of a supersonic combustor corresponding to flight conditions..	17
Table 2.2 Pressures of the three sections corresponding to flow conditions.....	23

List of Captions

<i>Number</i>	<i>Page</i>
Figure 1.1 A schematic of a scramjet engine	1
Figure 1.2 Specific impulses of turbojet, ramjet and scramjet engines as a function of flight Mach number.	3
Figure 1.3 A schematic of the dual mode ramjet/scramjet engine.	4
Figure 1.4 Number densities of the species in the plasma of H ₂ (75%)/Ar (25%) as a function of electron temperature (T _e): (a) T _e = translational temperature (T _t), (b) T _e = 2 T _t and (c) T _e = 3 T _t	8
Figure 1.5 A graph of radical concentration (n _{rad}) and discharge voltage (V) as a function of time.	10
Figure 2.1 Distance versus time diagram of a shockwave, contact surfaces and rarefaction waves in the expansion tube.	18
Figure 2.2 Stanford expansion tube facility.	19
Figure 2.3 A schematic of the expansion tube control system.	21
Figure 2.4 (a) A cavity model installed in the test section and (b) the bottom view of the model.	25
Figure 2.5 Pictures of a cavity model: (a) a schematic of the model, (b) top view, (c) front view, and (d) side view.	27
Figure 2.6 Pictures of a flat plate model: (a) a schematic of the model, (b) top view, (c) front view, and (d) side view.	28
Figure 2.7 (a) A schematic of the fuel delivery system and the expansion tube synchronization system - (1) through (12) are the signals described in Figs 2.8 (a) through (l), respectively, and (b) timing diagram of events occurring during an expansion tube operation.	29
Figure 2.8 Signals of synchronization equipments.	31
Figure 2.9 A schematic of the Schlieren system.	37
Figure 3.1 A set of time sequential Schlieren images describing an evolution of a hydrogen jet injected into a test section filled with static (U _∞ = 0) ambient air (200 torr).	41

Figure 3.2 (a) A set of time sequential Schlieren images illustrating the flow field in the presence of a supersonic freestream flow (run condition 2: $Ma \sim 2.0$, $h_0 \sim 2.0$ MJ/kg, $T_{static} \sim 1250$ K, $P_{static} \sim 16$ kPa and $U_\infty \sim 1380$ m/s) with $J_n \sim 4.5 \pm 0.1$: the test time starts at $0 \mu s$ and ends at approximately $500 \mu s$, and (b) a schematic of three shock waves induced by (i) the jet injection, (ii) the front step and (iii) the inclined back wall of the cavity..... 42

Figure 3.3 Three OH PLIF images showing auto-ignited hydrogen cavity flames in the absence of a plasma in supersonic flows of three different enthalpies: (a) run condition 8: $Ma \sim 2.9$, $h_0 \sim 3.3$ MJ/kg, $T_{static} \sim 1360$ K, $P_{static} \sim 23$ kPa and $U_\infty \sim 2370$ m/s ($J_n \sim 3 \pm 0.1$), (b) run condition 7: $Ma \sim 2.6$, $h_0 \sim 2.9$ MJ/kg, $T_{static} \sim 1330$ K, $P_{static} \sim 23$ kPa and $U_\infty \sim 2060$ m/s ($J_n \sim 4.5 \pm 0.1$) and (c) run condition 6: $Ma \sim 2.5$, $h_0 \sim 2.6$ MJ/kg, $T_{static} \sim 1300$ K, $P_{static} \sim 17$ kPa and $U_\infty \sim 1820$ m/s ($J_n \sim 5.5 \pm 0.1$). 44

Figure 3.4 Time sequential OH PLIF images in the absence of a plasma separated by $40 \mu s$ with a supersonic crossflow (run condition 7: $Ma \sim 2.6$, $h_0 \sim 2.9$ MJ/kg, $T_{static} \sim 1330$ K, $P_{static} \sim 23$ kPa and $U_\infty \sim 2060$ m/s) and a hydrogen jet ($J_n \sim 4.5 \pm 0.1$)..... 45

Figure 3.5 OH PLIF images of a cavity flame in supersonic flows of two different enthalpies: (a) without the plasma and (b) in the presence of the plasma in run condition 8 flow: $Ma \sim 2.9$, $h_0 \sim 3.3$ MJ/kg, $T_{static} \sim 1360$ K, $P_{static} \sim 23$ kPa and $U_\infty \sim 2370$ m/s (hydrogen jet, $J_n \sim 4 \pm 0.1$), and (c) without the plasma and (d) in the presence of the plasma in run condition 7 flow: $Ma \sim 2.6$, $h_0 \sim 2.9$ MJ/kg, $T_{static} \sim 1330$ K, $P_{static} \sim 23$ kPa and $U_\infty \sim 2060$ m/s (hydrogen jet, $J_n \sim 3.5 \pm 0.1$) 48

Figure 3.6 Time sequential OH PLIF images in the presence of a plasma separated by $40 \mu s$ in a run condition 7 flow: $Ma \sim 2.6$, $h_0 \sim 2.9$ MJ/kg, $T_{static} \sim 1330$ K, $P_{static} \sim 23$ kPa and $U_\infty \sim 2060$ m/s with a hydrogen jet ($J_n \sim 4.5 \pm 0.1$)..... 49

Figure 3.7 An OH PLIF image taken with a run condition 2 air flow: $Ma \sim 2.0$, $h_0 \sim 2.0$ MJ/kg, $T_{static} \sim 1250$ K, $P_{static} \sim 16$ kPa and $U_\infty \sim 1380$ m/s, and a hydrogen jet ($J_n \sim 2.5 \pm 0.1$). 50

Figure 3.8 OH PLIF images taken with a run condition 7 air flow ($Ma \sim 2.6$, $h_0 \sim 2.9$ MJ/kg, $T_{static} \sim 1330$ K, $P_{static} \sim 23$ kPa and $U_\infty \sim 2060$ m/s) with an ethylene jet injection ($J_n \sim 3 \pm 0.1$): (a) without a plasma and (c) in the presence of the plasma, and (b) a hydrogen jet injection ($J_n \sim 3.5 \pm 0.1$) without the plasma. 52

Figure 3.9 Schlieren images taken with a run condition 2 air flow ($Ma \sim 2.0$, $h_0 \sim 2.0$ MJ/kg, $T_{static} \sim 1250$ K, $P_{static} \sim 16$ kPa and $U_\infty \sim 1380$ m/s) and a hydrogen jet injection of varying J_n 53

Figure 3.10 OH PLIF images taken with a run condition 2 air flow ($Ma \sim 2.0$, $h_0 \sim 2.0$ MJ/kg, $T_{static} \sim 1250$ K, $P_{static} \sim 16$ kPa and $U_\infty \sim 1380$ m/s) and a hydrogen jet. 54

Figure 4.1 Plasma emission images (top view) taken by an intensified fast framing camera with a supersonic air flow (run condition 1: $Ma \sim 1.7$, $h_0 \sim 1.0$ MJ/kg, $T_{static} \sim 900$ K, $P_{static} \sim 25$ kPa and $U_\infty \sim 1000$ m/s): 0 μs is the beginning of the test time lasting approximately 700 μs 60

Figure 4.2 A schematic of a flow field caused by a single fuel jet injection..... 61

Figure 4.3 An OH emission image depicting a small reaction region triggered by the pulsed plasma in a supersonic oxygen crossflow (run condition 1: $Ma \sim 1.7$, $h_0 \sim 1.0$ MJ/kg, $T_{static} \sim 900$ K, $P_{static} \sim 25$ kPa and $U_\infty \sim 1000$ m/s) with $J \sim 0.1$ 62

Figure 4.4 A schematic of dual fuel jet injection model implemented with an oblique upstream jet, a transverse downstream jet and two electrodes between the two jets. 63

Figure 4.5 Two Schlieren images illustrate flow fields (run condition 2: $Ma \sim 2.0$, $h_0 \sim 2.0$ MJ/kg, $T_{static} \sim 1250$ K, $P_{static} \sim 16$ kPa and $U_\infty \sim 1380$ m/s): (a) only with the downstream jet ($J_n \sim 9.5 \pm 0.1$) injection and (b) with both of the upstream ($J_n \sim 3.5 \pm 0.1$)/downstream jets activated. Rectangular regions indicated by red dotted lines in the Schlieren images are overlapped on OH PLIF images (c) without and (d) with the upstream jet. The test gas is pure oxygen. 65

Figure 4.6 Two OH PLIF images overlapped on Schlieren images taken with pure oxygen crossflow (run condition 4: $Ma \sim 2.4$, $h_0 \sim 2.4$ MJ/kg, $T_{static} \sim 1300$ K, $P_{static} \sim 24$ kPa and $U_\infty \sim 1690$ m/s): (a) without the upstream jet ($J_n \sim 0.1$ and 60° angle) and (b) with the both jets activated, and (c) a Schlieren image confirming

the application of the upstream subsonic oblique jet and the downstream sonic transverse jet ($J_n \sim 2 \pm 0.1$) (the jets are injected into 200 torr static ambient air in the test section)..... 67

Figure 4.7 OH emission images in a supersonic oxygen crossflow (run condition 1: $Ma \sim 1.7$, $h_0 \sim 1.0$ MJ/kg, $T_{static} \sim 900$ K, $P_{static} \sim 25$ kPa and $U_\infty \sim 1000$ m/s) taken 1 μ s after a plasma pulse: (a) side view with only the upstream jet ($J_n \sim 0.1$), and (b) side view and (c) top view with both of the upstream/downstream ($J_n \sim 2 \pm 0.1$) jets injected. 68

Figure 4.8 OH PLIF images in front of the downstream jet of $J_n \sim 3 \pm 0.1$ taken (a) without the plasma and 1 μ s after a discharge pulse: (b) anode upstream and (c) cathode upstream. A typical Schlieren image taken under the same flow condition (run condition 3: $Ma \sim 2.4$, $h_0 \sim 2.4$ MJ/kg, $T_{static} \sim 1240$ K, $P_{static} \sim 18$ kPa and $U_\infty \sim 1650$ m/s) is overlapped on the PLIF images. The upstream jet injection angle is 60° from a horizontal plane and $J_n \sim 0.1$ 69

Figure 4.9 OH PLIF images taken (a) in the absence of a plasma, and (b) 1 μ s after a plasma pulse under a high enthalpy flow condition (run condition 4: $Ma \sim 2.4$, $h_0 \sim 2.4$ MJ/kg, $T_{static} \sim 1300$ K, $P_{static} \sim 24$ kPa and $U_\infty \sim 1690$ m/s). The upstream and downstream hydrogen jets are activated with corresponding jet momentum ratios $J_n \sim 0.1$ and $J_n \sim 2 \pm 0.1$ 70

Figure 4.10 OH PLIF images (Fig. 4.9) overlapped with a typical Schlieren image of the same flow condition (run condition 4: $Ma \sim 2.4$, $h_0 \sim 2.4$ MJ/kg, $T_{static} \sim 1300$ K, $P_{static} \sim 24$ kPa and $U_\infty \sim 1690$ m/s): (a) without the plasma and (b) in the presence of the plasma. The upstream and downstream hydrogen jets are activated with corresponding jet momentum ratios $J_n \sim 0.1$ and $J_n \sim 2 \pm 0.1$ 73

Figure 4.11 OH PLIF images overlapped with a Schlieren image (a) in the absence of the plasma taken 200 μ s after the beginning of the test time, and (b), (c) and (d) are taken 1 μ s after a plasma pulse: (b) at the beginning of the test time, 0 μ s, (c) 100 μ s and (d) 200 μ s after the beginning. (e) is taken 18 μ s after the plasma pulse. Pure oxygen crossflow is used (run condition 3: $Ma \sim 2.4$, $h_0 \sim 2.4$ MJ/kg, $T_{static} \sim 1240$ K, $P_{static} \sim 18$ kPa and $U_\infty \sim 1650$ m/s). The upstream and

downstream hydrogen jets are activated with corresponding jet momentum ratios $J_n \sim 0.1$ and $J_n \sim 3 \pm 0.1$	74
Figure 4.12 OH PLIF images taken (a) without and (b) in the presence of the pulsed plasma. Both of the upstream and downstream ($J_n \sim 2$) ethylene jets are injected into the oxygen crossflow (run condition 3: $Ma \sim 2.4$, $h_0 \sim 2.4$ MJ/kg, $T_{static} \sim 1240$ K, $P_{static} \sim 18$ kPa and $U_\infty \sim 1650$ m/s). J_n of the 30° angled upstream jet is approximately 0.1	76
Figure 5.1 The schematic of the simulation procedure.	79
Figure 5.2 Plasma emission pictures under varying air pressure conditions.....	80
Figure 5.3 Typical electron energy distribution functions calculated by BOLSIG.....	82
Figure 5.4 The schematic of the concept of the perfect stirred reactor (PSR).	85
Figure 5.5 Temperature of the equimolar H_2/O_2 mixture vs. time: (a) without the pulsed plasma and (b) in the presence of the plasma (50 kHz and 10 W).	87
Figure 5.6 A graph of the mole fractions of the radicals (H, O and OH) vs. time under 900 K initial temperature condition (equimolar H_2/O_2 mixture).....	88
Figure 5.7 A graph of the mole fractions of the radicals (H, O and OH) vs. time under 500 K initial temperature condition (equimolar H_2/O_2 mixture).....	90
Figure 5.8 A graph of the temperature of the equimolar H_2/O_2 mixture vs. time with the pulsed plasma (50 kHz) of varying plasma power from 10 W to 100 kW.....	91
Figure 5.9 Graphs of radical ((a) – (d): H, (e) – (h): O and (i) – (l): OH) mole fractions vs. time with the pulsed plasma of varying frequency from 10 kHz to 100 kHz under (a), (e) and (i): 500 K, (b), (f) and (j): 700 K, (c), (g) and (k): 800 K, and (d), (h) and (l): 850 K initial mixture (equimolar H_2/O_2) temperature conditions.	91
Figure 5.10 Simulation procedure and assumptions for validation of the flat wall model with the dual fuel jet injection configuration.	98
Figure 5.11 Graphs of (a) temperature and radical ((b) and (c): H, (d): O, and (e): OH) mole fractions as a function of time revealing the effect of the dissociated radicals produced by the pulsed plasma.....	100

Figure 5.12 Graphs of (a) temperature and radical ((b) H, (c) O and (d) OH) mole fractions as a function of time showing the effect of heat energy deposition (the same amount of the energy of one plasma pulse)..... 105

Figure 6.1 A schematic of the dual-jet configuration with a cavity..... 114

Figure 6.2 A schematic of the multiple oblique fuel jet injection configuration..... 115

Figure A.1 A schematic of the MOSFET (NTE 2385). 116

Figure A.2 A schematic of the high speed switching circuit..... 118

Figure B.1 A photograph of a high voltage nanosecond pulse generator (FID Technology, Model F1112). 119

Figure C.1 A photograph of a Faraday cage, a ceramic plate, a copper mesh and shielded cables..... 121

Figure C.2 A schematic of the fuel delivery system and the expansion tube synchronization system indicating the devices in a separate room (room 2) and cables (blue solid lines) underneath the floor..... 121

Chapter 1 Introduction

1.1. Motivation

The problem of igniting and sustaining combustion in high speed gas flows continues to be a critical issue in the aerospace industry. The advent of supersonic/hypersonic aircraft has prompted the demand for stable combustion in high speed flows to achieve reliable thrust over a broad range of flight conditions. Supersonic combustion is essential for air-breathing scramjet engines designed for hypersonic aircraft. The scramjet engine has drawn particular attention as it is a reusable and highly cost effective engine possibly enabling flight into low earth orbit. New cost effective transportation solutions using the scramjet engine have been developed by the United States, Russia, Japan, Australia, France and Germany (Curran (2001)) with earlier international cooperation such as the joint Russian-American scramjet flight test (Roudakov et al. (1996)). Theoretically, the scramjet engine can be used when the aircraft reaches approximately Mach 3 flight, although the engine is started at higher Mach numbers in practice. The schematic presented in Fig. 1.1 (Rogers et al. (1998)) illustrates the basic structure of the scramjet engine. The

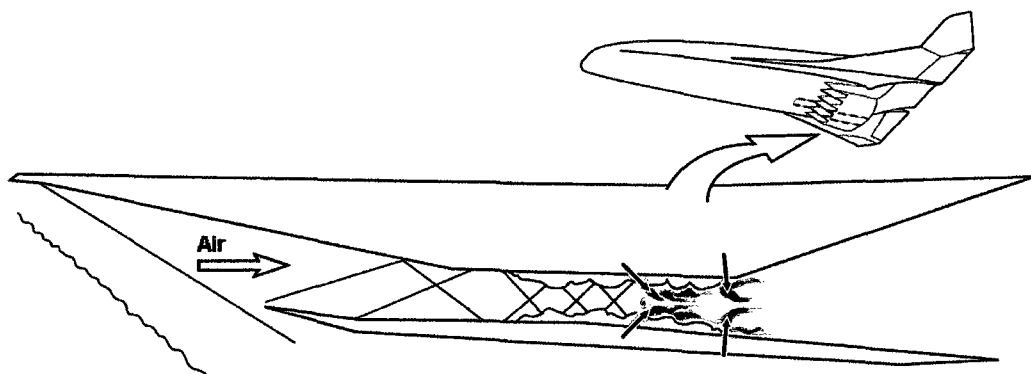


Figure 1.1 A schematic of a scramjet engine.

supersonic or hypersonic incoming ambient air is compressed through the inlet nozzle of the engine by compression shockwaves to become a high enthalpy supersonic air flow when passing through the combustor. As the air flow passes through the combustor, it mixes and burns with fuel, and expands through the aft end of the engine to produce thrust. While bluff bodies providing recirculation regions are often implemented as flame holders in subsonic flows such as in the afterburner of a turbojet engine, a greater challenge is faced in the igniting and sustaining of combustion in supersonic flows because the use of such bluff bodies leads to significant stagnation pressure losses that limit engine thrust and can also induce engine unstart. New methods are therefore sought out for igniting and sustaining ignition in supersonic flows.

Any new method of ignition and flame holding should be applicable to various combustor flow conditions such as low enthalpy and high speed supersonic flows. Both the low enthalpy and the high speed flow conditions have adverse effects on flame stabilization. The ignition delay time (τ_{ign}) in the low enthalpy gas is longer than that in the high enthalpy gas, while the flow residence time (τ_{res}) of the gas in a supersonic combustor becomes shorter as the flow speed increases. As a result, no combustion occurs when $\tau_{\text{ign}} > \tau_{\text{res}}$. In common, the hypersonic aircraft capable of $\text{Ma} = 8$ or faster flight requires a combined cycle engine operating efficiently at low Mach number flight conditions (Curran et al. (1996)). For example, turbojet engines can start the vehicle to initiate subsonic-burning ramjet mode, and then the ramjet engine further accelerates for the transition to supersonic-burning ramjet mode (scramjet). As a reference, the specific impulses of the turbojet, ramjet and scramjet engines as a function of flight Mach number are illustrated in Fig. 1.2. Sawai et al. (2003) provided the example of the practical design of the ramjet engine combined with the turbojet engine. Otherwise, the transition from the subsonic-burning ramjet mode to scramjet mode demands variable geometry nozzles. The variable inlet nozzle design shown in Fig. 1.3 was proposed for the dual mode engine operation (ramjet and scramjet modes) in the Integrated System Test of an Air breathing Rocket (ISTAR) program (Andreadis et al. (2002)). Alternatively, the design of the Dual-Combustor Ramjet

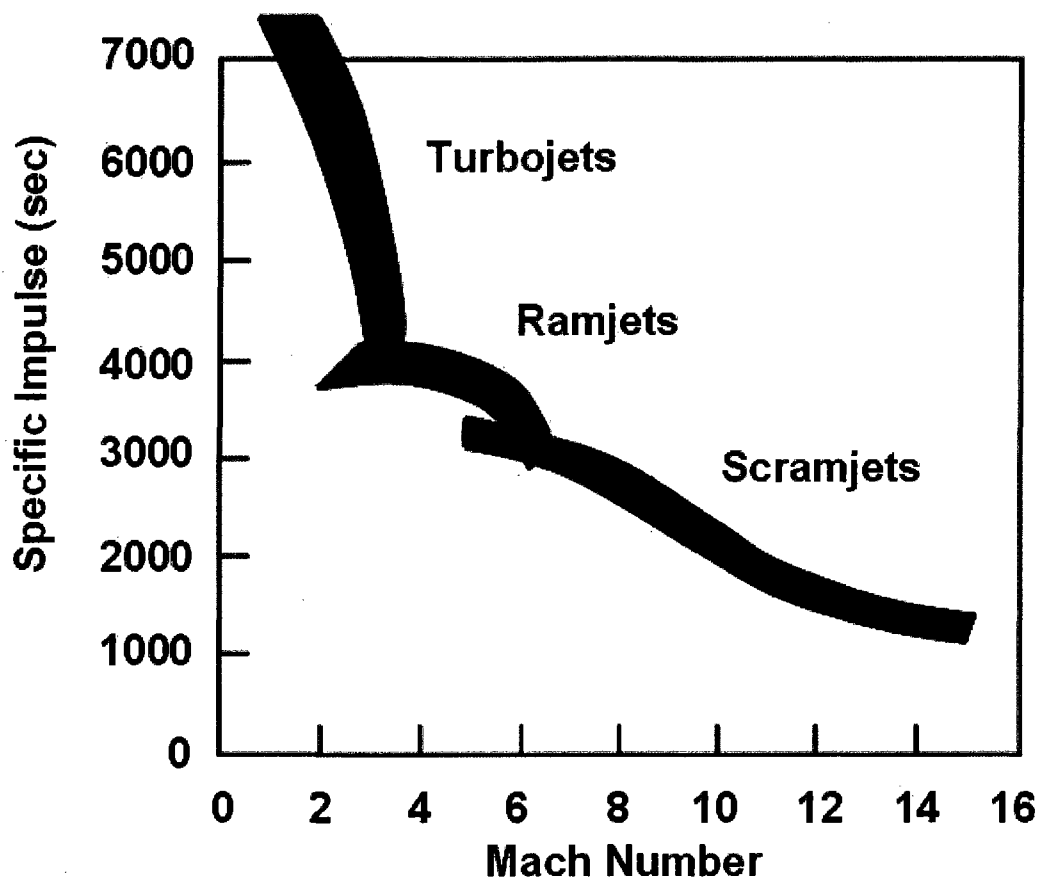


Figure 1.2 Specific impulses of turbojet, ramjet and scramjet engines as a function of flight Mach number.

(DCR) was proposed to accommodate both burning modes in an integrated engine with minimal moving parts (Waltrup (1992)). To avoid the complexity of the dual burning mode design, it is desirable to lower the minimum operating Mach number of the scramjet mode. Various attempts to achieve stable thrust of the scramjet engine under the lower flight Mach number conditions, particularly, flame stabilization methods in supersonic environments, will be presented in Section 1.2.3. Recently tested scramjet engines were loaded on rocket engines to obtain high enthalpy inlet flows directly initiating the scramjet mode. These include; HyShot (University of Queensland) on a Terrier-Orion Mk70 rocket and the X-43A (NASA) on a Pegasus rocket. In particular, the combination of scramjet power and solid rocket booster

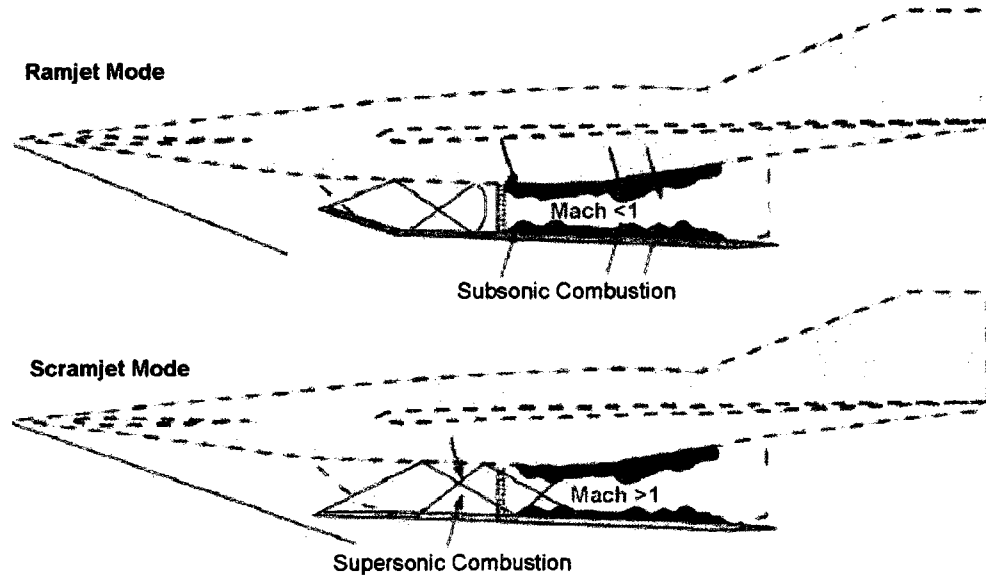


Figure 1.3 A schematic of the dual mode ramjet/scramjet engine.

acceleration is applicable to hypersonic cruise missiles because they are disposable (Kazmar (2005)). The previously proposed strategies reviewed here were concentrated on the elevation of the inlet flow enthalpy to start the scramjet engine. However, more convenient and effective solutions can be found in new flame stabilization methods applicable to low enthalpy supersonic flows.

The conventional flame stabilization methods capable of lowering the operating Mach number of the scramjet engine mostly utilize geometric alterations of the surface of the supersonic combustor. An example of such alterations includes the use of a wall cavity. These geometric alterations cause shockwaves leading to additional stagnation pressure loss in the combustor. The loss in stagnation pressure in a scramjet engine is primarily due to shockwaves, air/fuel combustion, and skin friction. The stagnation pressure loss rapidly increases with the flight Mach number resulting in very low thrust under hypersonic flight conditions or insufficient thrust to accelerate the vehicle to the hypersonic Mach numbers (Emanuel (2003)). Therefore, minimizing stagnation pressure loss is crucial to achieve maximized thrust especially for hypersonic aircraft. In general, any shockwaves induced inside and outside of the engine cause stagnation pressure loss of the inlet flow. The shockwaves are mostly

induced by the geometry of the engine's inner surface, struts and the fuel jet injection in the combustor. Therefore, minimal geometric alterations, with ideally smooth inner surfaces, are desirable. However, various geometric alterations are applied on the combustor's surface to provide slow flow recirculation regions for flame stabilization. In short, new flame stabilization methods with minimal geometric alterations are required to maximize aircraft thrust.

The choice of a simple and energy efficient method of flame stabilization is essential to maximize the mobility and the cruising range of the aircraft. As previously mentioned, under higher enthalpy flow conditions, it is easier to stabilize flames due to the shorter ignition delay time. Therefore, energy deposition into the flow passing through the combustor, elevating the flow enthalpy, will provide favorable flow conditions for flame stabilization. However, the means of energy deposition needs to be prompt and efficient because the flow residence time in the scramjet engine is very short. In addition, flame stabilization methods that provide minimal energy deposition into the flow are desirable to achieve overall high energy conversion efficiency. The effect of energy deposition into non-flammable supersonic/hypersonic flows was investigated using electric arc discharges (Satheesh et al. (2007)), lasers (Adelgren et al. (2003)) and microwaves (Knight et al. (2007)) for local flow control reducing drag or modifying scramjet inlet flows. Satheesh et al (2007) has shown that the local energy deposition in front of a blunt body reduces the drag by 50 % in argon supersonic flows, an effect attributed to thermal heating by the discharge. Besides, the energy deposition into the highly flammable gas flows in the combustor is capable of initiating combustion reaction without a high power energy source. In our previous studies (Kim et al. (2006)), the highly energy efficient nonequilibrium nanosecond pulsed plasma is shown to be able to initiate and sustain combustion reactions under the harsh conditions where flames cannot be ignited nor stabilized. The nanosecond pulsed plasma can deposit energy into the flow during the extremely short pulse width (~ 10 ns). Incidentally, the pulsed plasma generation system is simple and portable because the pulsed plasma usually consumes very low energy compared to the energy

of the combustion reaction initiated by the plasma (the ratio is on the order of 10^{-5} ; see Chapter 4).

In this thesis, jet flame stabilization methods in supersonic environments are presented using energy efficient nonequilibrium pulsed plasmas generated by a simple high voltage pulsing system. In particular, we focus on configurations that may minimize stagnation pressure losses.

1.2. Background

This dissertation is an experimental study of two different flame stabilization methods in supersonic flow environments. Both methods utilize a nonequilibrium pulsed plasma which has been used to stabilize flames in various flow conditions, mostly in subsonic flows, for the last few decades. In previous research, the use of nonequilibrium plasmas was proven to be a promising technique for flame stabilization due to its unique characteristics such as efficient radical production in the plasma region. This section will present a review of the previous research involving the characteristics of the pulsed plasma and its application for flame stabilization.

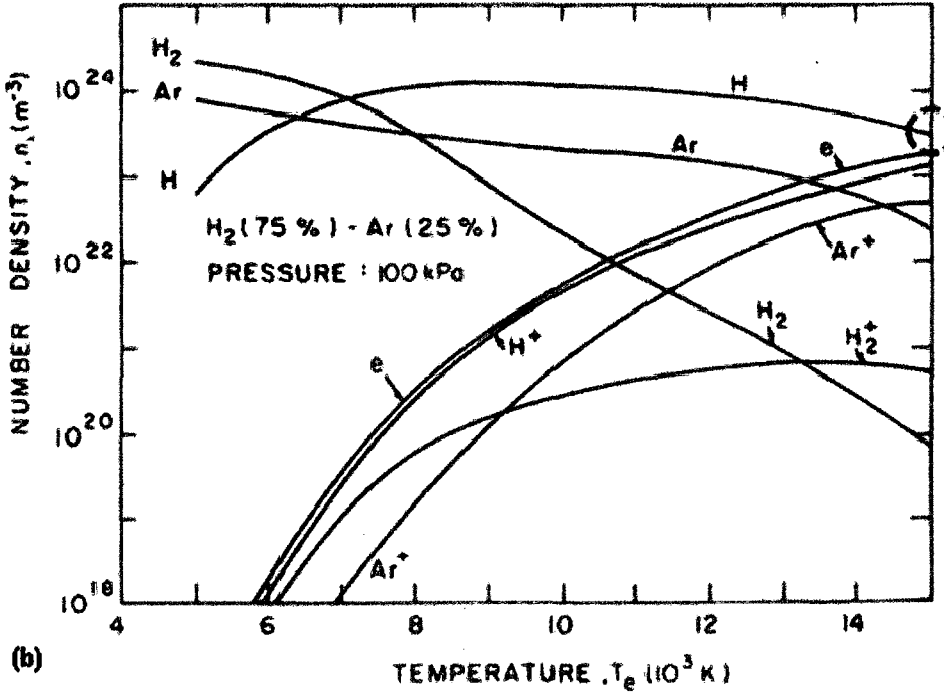
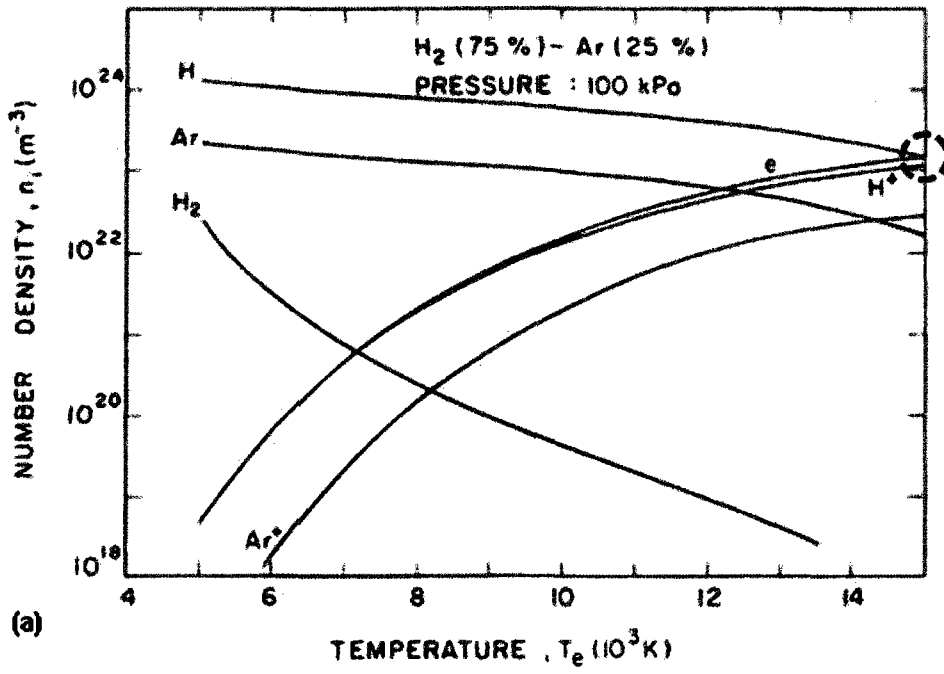
1.2.1. Nonequilibrium Pulsed Plasma

A nonequilibrium plasma is characterized by a gas medium with vastly different temperatures (or average energy) in its constituent fluids (e.g., the electrons, ions, neutrals). This nonequilibrium characteristic originates from the unusually high energy electrons produced as a result of ohmic heating as a result of the high electric field (potential) applied across electrodes. The disparity in mass between the electron and atomic/molecular species results in collision between the electron and the heavy species (atom and molecules) that is not effective in elevating the kinetic energy of the heavy species (translational energy) whereas the electron energy is more easily transferred to the internal energy mode of the heavy species. Therefore, the internal

energies are usually higher than the translational energy in nonequilibrium discharges. In our previous study (Kim et al. (2006)), the vibrational temperature of the N_2 molecules in a nanosecond pulsed plasma is estimated to be approximately 4000 K although the translational temperature rise above ambient is relatively small (less than 100 K).

The degree of nonequilibrium depends on the collision frequency between the electrons and the heavy species. As this collision frequency increases, the difference between the electron temperature and the heavy species translational temperature decreases, as more energy is transferred to the energy of translation of the heavy species, reducing the electron temperature (and hence the temperatures of internal energy modes) and increasing the heavy species translational temperature. In the limit, as the temperatures approach each other, we are said to be in the thermal plasma limit. The transition from the nonthermal (highly nonequilibrium state) to thermal plasma mostly occurs under high electron density (high current) and relatively high gas pressure conditions that raise the collision frequency as discussed by Boulos et al. (1994). A thermal plasma consumes more energy when compared to a nonthermal plasma because the thermal plasma requires higher current with higher voltage and, obviously, a large amount of the electron energy in the thermal plasma is deposited into the gas medium in the form of the heat energy (translational temperature elevation).

The nonequilibrium plasma is energy efficient in producing dissociated radicals from neutral molecular parent species, if the plasma has a sufficiently high electron temperature, high enough to dissociate the molecules. Efficient radical formation by dissociation of a parent molecular species by nonequilibrium plasmas has been observed under low pressure gas conditions by numerous researchers, including Naidis (1997) and Brown et al. (2007). In Fig. 1.4 (Boulos et al. (1994); pp. 258 – 259), the number densities of the various species in a plasma (H_2/Ar), including dissociated/ionized species by electron impact, are presented as a function of electron temperature (T_e) under various translational temperature (T_t) conditions: (a) $T_e = T_t$, (b) $T_e = 2 T_t$ and (c) $T_e = 3 T_t$. Under a fixed electron temperature condition at 15000



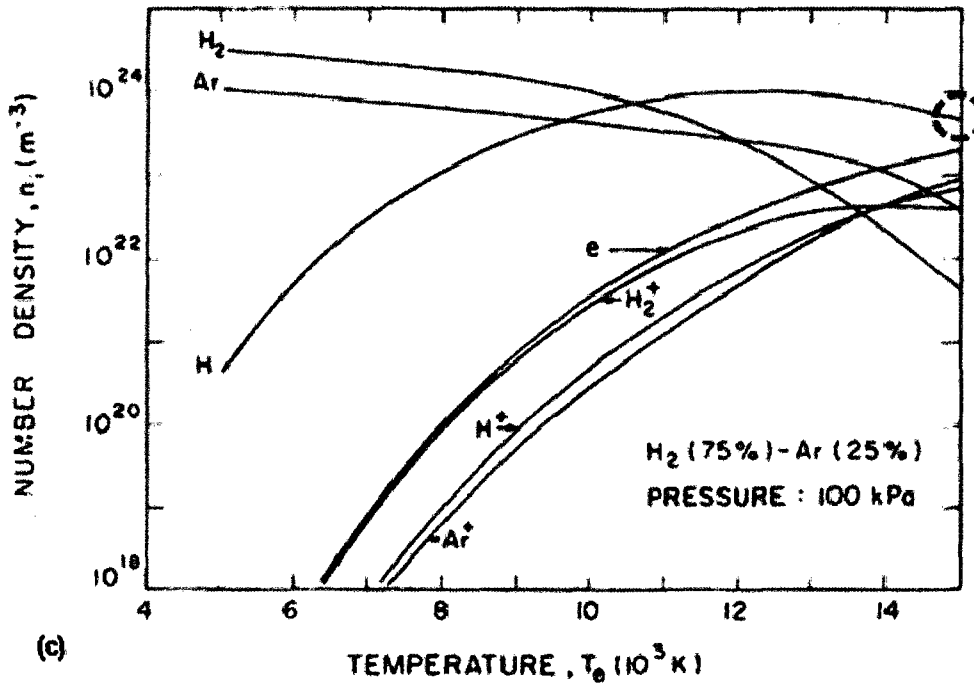


Figure 1.4 Number densities of the species in the plasma of H₂ (75%)/Ar (25%) as a function of electron temperature (T_e): (a) $T_e =$ translational temperature (T_t), (b) $T_e = 2 T_t$ and (c) $T_e = 3 T_t$.

K in the red dotted circles in Figs 1.4 (a), (b) and (c), the translational temperature of a hydrogen (75 %)/argon (25 %) mixture varies from 15000 K (Fig. 1.4 (a)) to 5000 K (Fig. 1.4 (c)). In these different translational temperature cases, the dissociated hydrogen atom's number density stays almost unchanged (all of the number densities are on the order of 10^{23} per cubic meter), which means that, under the high electron temperature conditions, the effect of the translational temperature of the gas medium on the dissociation reaction is almost negligible. A way to achieve the high electron temperature without elevating the translational temperature of the gas medium is the use of a nanosecond pulsed plasma.

The nanosecond pulsed plasma (10 ns pulse width) used in this study is a highly nonequilibrium plasma. The typical (measured) peak voltage and peak current of the discharge pulse are 15 kV and 15 A, respectively. More detailed specifications

of the pulsed plasma will be presented in Chapter 2. The short pulse width of the plasma pulse suppresses the excess of the total current that would otherwise cause the transition to the thermal plasma state (Lutz (1973)) and the increase in translational temperature is negligible. However, the plasma pulses are capable of producing radicals, including dissociated, ionized and excited species, because the electron temperature is sufficiently high enough due to the high electric field at the peaks of the plasma pulses. The electron temperature of the pulsed plasma used in the current study is estimated to be approximately 9×10^4 K (the estimation will be explained in section 4.3.5). If the pulse repetition rate is high enough to sustain or build up the radical concentration between the plasma pulses (the time between pulses is less than the characteristic recombination time), the pulsed plasma is much more energy efficient in producing radicals than the thermal plasma or the continuous plasma such as direct current (DC) and radio frequency (RF) plasmas. Figure 1.5 shows a graph of discharge voltage and radical concentration in a pulsed plasma discharge as a function of time. Green and red curves represent the discharge voltage and the radical concentration,

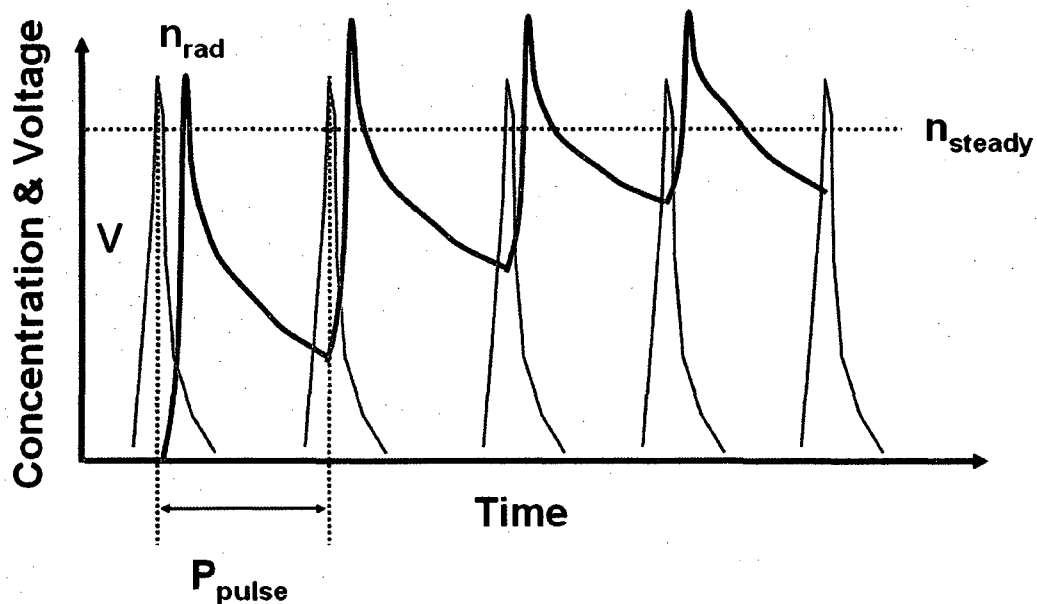


Figure 1.5 A graph of radical concentration (n_{rad}) and discharge voltage (V) as a function of time.

respectively. As illustrated in the graph, sudden radical concentration rises follow the voltage pulses while there is a drop in between pulses due to radical recombination. Nevertheless, the concentration will approach a certain steady value (n_{steady}) depicted by blue dotted line when the pulse period (P_{pulse}) is shorter than radical recombination time scale. Similar trend is observed in the numerical study of a pulsed plasma model presented in Chapter 5. The effectiveness of nonequilibrium pulsed plasmas on the production of dissociated and ionized species has also been shown by Naidis (1997), Fons et al. (1994), Macheret et al. (2002) and Bychkov et al. (2007).

1.2.2. Flame Stabilization Using Nonequilibrium Plasma

The nonequilibrium pulsed plasma is able to stabilize combustion reactions because of its capacity to efficiently produce reactive radical species. There have been numerous successful studies utilizing plasmas as a tool for flame stabilization. One of the most frequently used conventional flame ignition methods is the use of the spark plug in internal combustion engines. The spark plug produces a thermal plasma of up to 60000 K temperature (Stiesch (2003)) to initiate the combustion reaction in the engine. However, Cathey et al. (2002) have shown that the nonequilibrium pulsed plasma is more effective and energy efficient in igniting and sustaining combustion reactions in such internal combustion engines by reducing the ignition delay time to values beyond the reduction achieved by the traditional spark ignition methods. The superior ability of nonequilibrium plasmas in ignition delay reduction has also been verified numerically and experimentally by the studies of Bozhenkov et al. (2003). The ignition delay dependence on energy deposition from nonequilibrium plasmas with an emphasis on the comparing nanosecond and microsecond high voltage pulsed plasmas was studied recently by Zhukov et al. (2007).

Methane flame stabilization using a nonequilibrium pulsed plasma was investigated recently in experiments carried out at Stanford (Kim et al. (2008)). As mentioned previously, radicals produced by the plasma play an important role in igniting and sustaining combustion reactions. However, it was shown in these recent

studies that the radicals are not directly responsible for igniting flames. Instead, they are critical to the chemistry that results in the reforming of the fuel, into stable species such as H_2 and CO . It is these intermediate species that are then responsible for flame ignition and stabilization. In this case, the pulsed plasma serves as an 'in-situ reformer' of the fuel (Kim et al. (2008)). Most previous researches have taken the plasma to be a direct ignition source by production of radicals such as OH (Liu et al. (2005), Pilla et al. (2006), Kim et al. (2007) and Mintoussov et al. (2006)). However, 'slow chemistry' (Bao et al. (2007)) or a low temperature reaction regime, sometimes referred to as a 'cool flame' (Kim et al. (2008)), is observed to take place between the plasma and the actual flame region. It is shown that the radicals cannot survive beyond the immediate vicinity of the plasma discharge, and are converted to the intermediate species that eventually make up the post-discharge region. This reforming mechanism proposed by Kim et al. (2008) cannot apply to H_2/O_2 ignition, and any plasma enhancements in this system would have to connect directly to the radical forming capacity of the plasma discharge. Helenbrook et al. (1998) found that an ignition turning point can occur solely through the interaction of radical species; the source of this turning was found to be the reaction $H + HO_2 \rightarrow 2OH$. Also, an updated comprehensive kinetic model of hydrogen combustion is presented by Li et al. (2004). In the updated kinetic model, it is shown that the role of H and O radicals in the chain reactions of the H_2/O_2 mixture is more important in the 800 K – 900 K temperature range when compared to other temperature conditions. Coincidentally, the pulsed plasma, numerically modeled in this dissertation (Chapter 5), produces H and O radicals and the most notable ignition delay reduction by the plasma is observed in that temperature range. The ignition mechanism and the reduction of the ignition delay of the H_2/O_2 mixture by the plasma, previously investigated by Popov et al. (2007) and Hayakawa et al. (1941), will be discussed in detail using the numerical method described in Chapter 5.

There have been some technical issues raised regarding the practical application of plasma methods for flame stabilization. For example, with jet diffusion flames (such as in the previous study of Kim et al. (2008)), how effective the pulsed

plasma is in aiding combustion seemed to be strongly dependent on the discharge placement. It was found that the discharge should be placed in regions of the flow field where adequate fuel and oxidizer mixing has taken place. Other factors, such as the local flow strain rate, must also be taken into consideration. In addition, usually, the plasma generation requires an electrode pair located near the flame region, which can limit its application if the plasma needs to be placed in gas flows (Bityurin et al. (2007), Kim et al. (2008) and Do et al. (2008)). Some novel designs of the electrodes such as the use of the jet nozzle as an electrode (Vincent-Randonnier et al. (2007)) are suggested to minimize the flow perturbation by the electrodes. On the other hand, laser induced plasmas (Morsy et al. (1999)) and microwave driven plasmas (Esakov et al. (2006)) do not require electrodes although waveguides, insulators and optically accessible combustor walls are essential for their application.

Practical issues arising in the application of nonequilibrium plasma discharges under supersonic flow conditions are more challenging due to the extremely high flow speed. Electrode insertion directly into the supersonic flow will itself cause strong shockwaves resulting in a stagnation pressure loss while also perturbing the flow. Also, sustaining the plasma in this flow environment itself becomes another challenging problem due to the fast radical removal from the discharge region caused by convection. Therefore, there have been various attempts (Rogers et al. (1998), Leonov et al. (2006) and Esakov et al. (2006)) at flame stabilization under these conditions using plasmas as reviewed in the next section.

1.2.3. Flame Stabilization in Supersonic Flows

Previously explored methods for igniting and sustaining combustion in supersonic gas flows mostly include either geometric surface alterations or plasma discharges.

The geometric surface alterations, such as cavities (Ben-Yakar et al. (2001), Rasmusen et al. (2005), and Gruber et al. (2004)), ramp injectors (Maddalena et al. (2005) and Anderson et al. (2005)), wall steps (Leonov et al. (2006)) and angled

combustor walls (Rogers et al. (1998)), generate recirculation regions for fuel and oxidizer to mix and reside long enough to be ignited and burned. In addition to promoting mixing, these geometric surface alterations also reduce the local flow speed and elevate the local static temperature and pressure. One of the most frequently used geometric alteration methods is the cavity flame stabilization method. Due to its convenient application (the simple variation of the ratio of the cavity length to the depth provides diverse effects on flows and flame stability) and effectiveness, numerous studies utilizing the method have been conducted. The results regarding the cavity flame stabilization methods are overviewed by Ben-Yakar et al. (2001). The flow field induced by the cavity is investigated by Kim et al. (2004), Lin et al. (2007) and Fang et al. (2008) to confirm the capability of the cavity in flame stabilization. However, these methods of enhancing combustion share an important limitation - the introduction of undesirable shockwaves due to flow disturbances. The generated shockwaves are a primary source of stagnation pressure loss.

Alternatively, plasma discharges have been used to facilitate combustion in supersonic flows. As previously mentioned, the capability of the plasma discharge has been proven under subsonic flow conditions. However, most of the plasma assisted methods applied for the ignition of diffusion flames in supersonic flows have been used in conjunction with geometric alterations. This has occurred since both of the flame stabilization methods enhance flame stability via independent approaches which can be easily combined. The plasma facilitates chemical reactions and the geometric alteration provides a favorable flow condition for flame holding. For example, in recent studies, an arc jet was injected into the downstream region of fuel injection ramp (Rogers et al. (1998)), and a quasi-direct-current (DC) discharge plasma was generated within a surface cavity (Leonov et al. (2006)). An alternative solution was found using microwave plasma discharges which were used in the absence of cavities or ramps to ignite supersonic premixed combustible gases (Esakov et al. (2006)). The microwave plasma can be applied in the middle of the supersonic flow without disturbing the flow because it does not require electrodes. However, a technique that has achieved successful ignition of diffusion flames at relatively high Mach number

without geometric variances to the flow surface has not yet been successfully demonstrated.

1.3. Aims and Scope

The ultimate goal of this study is to propose and understand an energy-efficient and effective flame stabilization method in supersonic flows that employ a nonequilibrium nanosecond pulsed plasma. The scope of the study is limited to the jet in supersonic crossflow configuration because this configuration is a common and practical fuel injection method for enhancing fuel jet mixing (Broadwell and Breidenthal (1984), and Smith and Mungal (1998)). In the current study, the jet diffusion flame in a supersonic crossflow is ignited using a pulsed plasma discharge. Also, the conventional cavity flame stabilization method is tested and it is used in conjunction with the application of the pulsed plasma. To find a better method for lessening stagnation pressure loss, the plasma is applied on a flat wall without any geometric alteration. In addition, a dual fuel jet injection configuration is proposed to provide a favorable flow condition for plasma assisted combustion in the supersonic environment.

In the experimental part of the study, nine different supersonic flow conditions are tested. The Mach number is varied from 1.7 to 3 and the flow enthalpy ranges between 1 MJ/kg and 3.8 MJ/kg. Two different gas flows are utilized, which are ambient air and pure oxygen flows. A fixed amount of power (~ 10 W) is consumed by the pulsed plasma of 50 kHz repetition rate, 10 ns pulse width, 15 A peak current and 15 kV peak voltage. In most cases, pure hydrogen gas is used as the jet fuel while ethylene gas is also tested to demonstrate the applicability of the plasma assisted combustion technique to hydrocarbon fuels.

Finally, for the investigation of the plasma assisted flame stabilization mechanism and the estimation of the prospective use of higher power pulsed plasma, modeling and simulations are conducted since the maximum power of the current

plasma generation system is only 10 W. The simplified simulation is focused on the plasma assisted ignition mechanism of a simple H_2/O_2 system.

Chapter 2 will describe the detailed experimental setup including the expansion tube providing supersonic gas flow over a relatively short time period (300 – 1000 μs), a plasma generation system, various diagnostic devices and experimental methods. A conventional cavity flame stabilization method used in conjunction with the pulsed plasma is tested and the experimental results are discussed in Chapter 3. Chapter 4 describes a new flame stabilization method that minimizes stagnation pressure loss by use of a flat wall without any geometric alteration on its surface. The experimentally proven capability of the pulsed plasma in the previous chapters is validated through the development of numerical models and the possibility of further flame stability enhancement using a higher power pulsed plasma is discussed in Chapter 5. Finally, the conclusions of the study and the suggestions for future work are presented in Chapter 6.

Chapter 2 Experimental Setup

In this chapter, experimental facilities and methods employed throughout this study are described.

2.1. Expansion Tube

An expansion tube designed and built by Heltsley et al. (2006) is used to simulate supersonic flows in the combustor of a scramjet engine. Scramjet engines are designed to power hypersonic aircraft. In common flight conditions of the aircraft, the hypersonic incoming air is compressed by an inlet nozzle to become a high enthalpy supersonic flow passing through the combustor. Table 2.1 (Heltsley et al. (2006)) shows flow conditions in the combustor corresponding to flight Mach numbers. To calculate the flow conditions in the combustor, it is assumed that a single oblique shock at the entrance of the engine reduces the Mach number of the inlet flow by a factor of three. The inlet ambient air conditions are selected from the U.S. standard atmosphere model at the altitude associated with the flight Mach number. The expansion tube serves as a wind tunnel capable of producing the high enthalpy supersonic flows found in supersonic combustors.

Flight Condition (Ma)	Combustor Condition (Ma)	Static Pressure (kPa)	Temperature (K)
4	1.33	85	670
5	1.67	78	830
6	2.00	65	990
7	2.33	55	1130
8	2.67	48	1270
9	3.00	40	1400

Table 2.1 Conditions of a supersonic combustor corresponding to flight conditions.

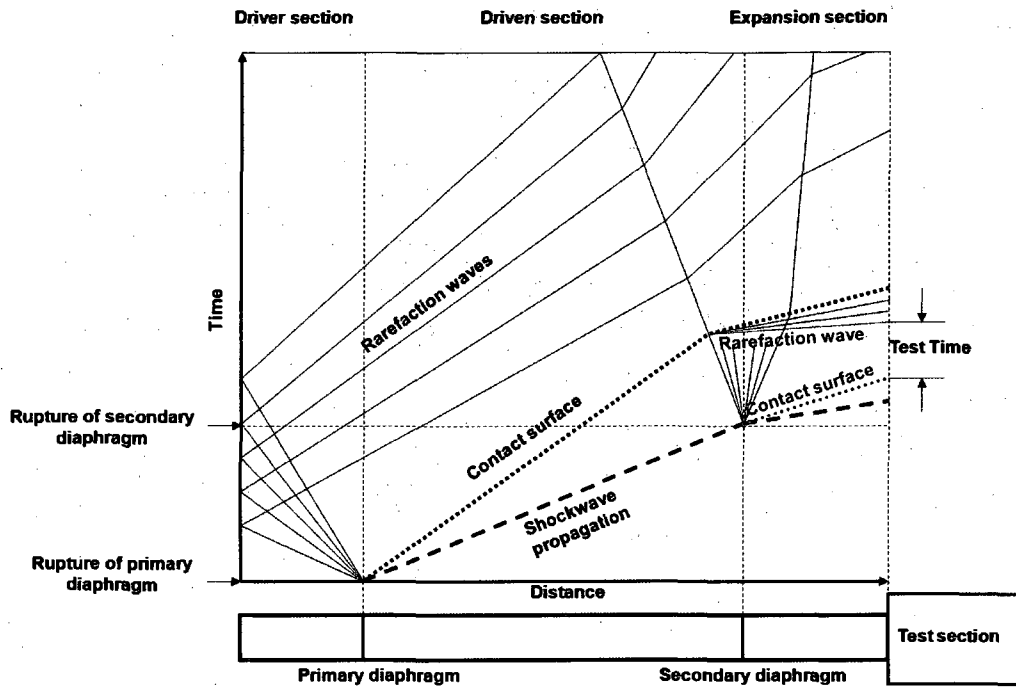


Figure 2.1 Distance versus time diagram of a shockwave, contact surfaces and rarefaction waves in the expansion tube.

Figure 2.1 shows a distance versus time diagram of shockwaves, contact surfaces, and rarefaction waves caused by ruptures of primary and secondary diaphragms of the expansion tube. The expansion tube, a circular stainless steel tube, is divided into three sections by primary/secondary diaphragms, which are driver, driven and expansion sections. The plastic diaphragms are designed to rupture at specific pressure differences between the sections. An expansion tube test begins with a rupture of the primary diaphragm caused by pressure difference between pressurized helium gas in the driver section and low pressure test gas (air or oxygen) in the driven section. Accordingly, the rupture of the primary diaphragm induces a strong shockwave. The shockwave, which precedes a contact surface of helium gas in the driver section and test gas in the driven section, travels through the driven section elevating the temperature and pressure of the test gas. When the shockwave reaches

the end of the driven section, the secondary diaphragm ruptures causing the test gas to move into the expansion section. When a contact surface (red colored dotted line in Fig. 2.1) of the test gas and the helium gas in the expansion section preceded by the shockwave arrives at the test section, a steady supersonic flow of the test gas is produced in the test section until the arrival of rarefaction waves (red colored solid line in Fig. 2.1). The test time, which is the time over which the supersonic flow of the test gas resides in the test section, varies from a few hundred microseconds to a millisecond depending on flow conditions.

2.1.1. Expansion Tube Body

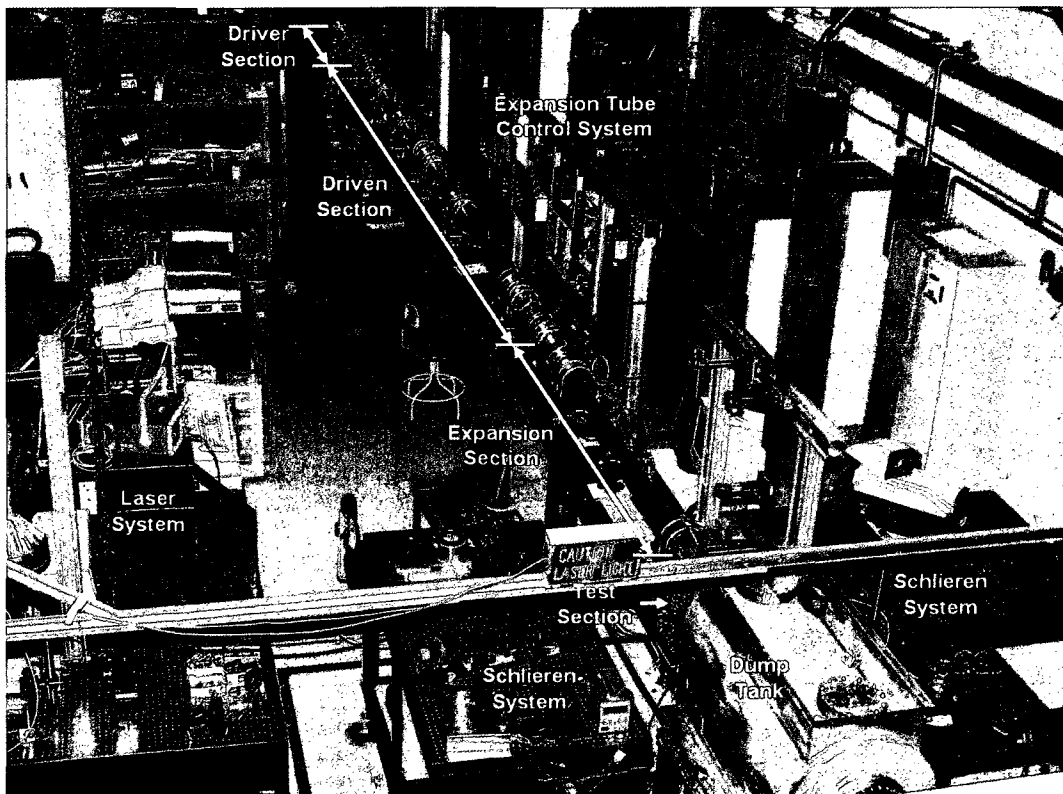


Figure 2.2 Stanford expansion tube facility.

A picture of the expansion tube facility is presented in Fig. 2.2. The expansion tube is a circular stainless steel tube (alloy 304) of 14 cm inner diameter (16.5 cm outer diameter) connected to a cylindrical dump tank (60 cm diameter and 122 cm length). The tube has three parts: the driver (2 m length), driven (7.3 m length) and expansion (2.8 m length) sections. A test section (welded stainless steel cube, 30 cm × 30 cm × 30 cm inside, 1.27 cm wall thickness) for observations and measurements is located between the expansion section and the dump tank. The test section has three optically accessible quartz windows (15 cm × 7.5 cm) and six cable/tube feed-through ports.

Each section is connected to an individual vacuum pump and a gas cylinder to provide designated static gas conditions in the tube before the operation of the facility. The static gas pressures and gas composition determine flow conditions in the test section during a test. Static gas pressures are measured by a capacitance sensing pressure transducer (Setra, Model 280E) at the driver section and two capacitance manometers (MKS, Model 690A13TRC) at the driven/expansion sections, respectively. Valve modules (details are presented in Section 2.1.2), operated by a computer based control system, are installed at the connections of devices to the expansion tube (e.g. vacuum pumps (Welch 1397: 17.7 CFM pumping speed), gas cylinders, capacitance manometers and a ventilation nozzle).

2.1.2. Control System

Figure 2.3 shows a schematic of the expansion tube control system. The system manipulates ten valve modules attached on the tube, and records pressure traces while a shockwave travels through the tube.

The computer interface for the control system is built around a Lab View (National Instruments) program. Ten virtual buttons on the control system interface operate the ten corresponding valve modules. A control box (National Instruments, NI PXI-1010) driven by the computer program generates control signals for the valve modules. Each valve module is a combination of a solenoid valve (SMC, Model

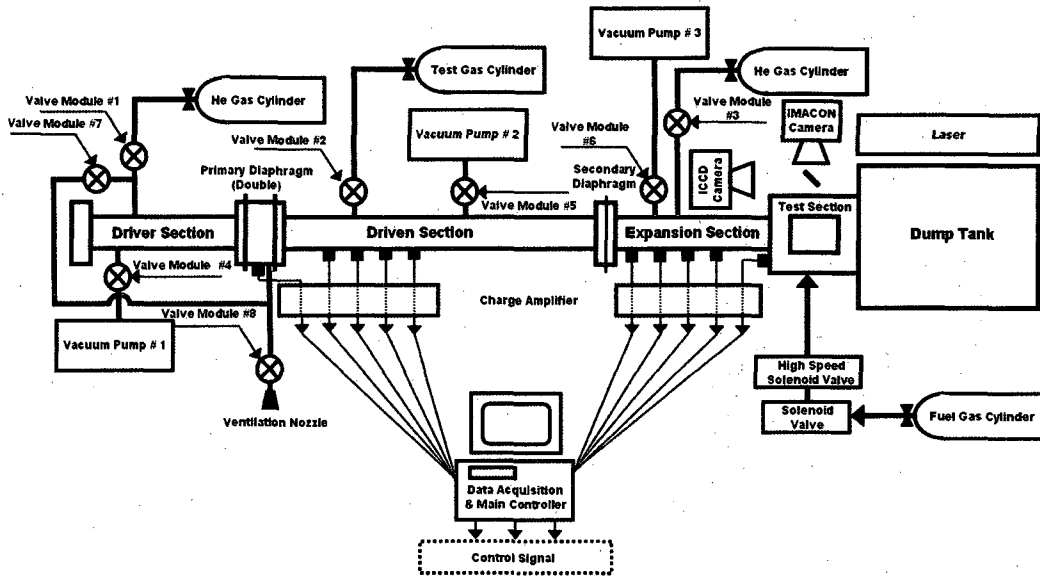


Figure 2.3 A schematic of the expansion tube control system.

NVZ110, Humphrey, Model 410 or MAC, Model 912B-PM-111CM) receiving a control signal and a pressure actuated valve (Whitey Co., Model 131 SR, Whitey Co., Model 133 SR or Swagelok, Model 135 DA) controlled by the solenoid valve: the solenoid valve opens and closes high pressure air line controlling the pressure actuated valve. Valve modules #1 through #3 serve as gas inlet controllers of driver, driven and expansion sections, respectively. Valve module #2 regulates the test gas (air or oxygen) pressure in the driven section and the other two modules (#1 and #3) control the helium gas pressure in the driver and expansion sections. Otherwise, valve module #4 through #6 are for the vacuum pumps of the driver, driven and expansion sections, respectively. The three sections are evacuated using the pumps to fill the sections with pure gases. Valve module #7 is used to adjust the pressure between two primary diaphragms (buffer section). The uses of double primary diaphragms and the buffer section will be explained in section 2.1.3. Finally, valve module #8 for the ventilation nozzle is located at the buffer section. Additional two valve modules for two capacitance manometers measuring static pressures of the driven and the expansion sections are also attached on the two sections. These two valve modules are closed during a test to protect the capacitance manometers from shockwaves. A manual

emergency stop switch (Wiremold, Plug-In Outlet Center Unit) is installed to close all of the 10 valve modules and a main fuel valve (Parker, solenoid valve) for safety. Details of the fuel delivery system and the main fuel valve will be presented in section 2.2.3.

Pressure traces are collected at ten measurement locations. Eight of these are fast response pressure sensors (PCB Piezotronics, Model 113A26) located on the inner surface of the tube (4 sensors evenly separated by 1 ft. in each of the driven and the expansion section), a pressure sensor (PCB Piezotronics, Model 113A26) at the buffer section, and a pitot tube connected to a pressure sensor (PCB Piezotronics, Model 113A26) in the test section. Raw signals from the sensors are amplified by a charge amplifier (PCB Piezotronics, Model series 481) and recorded by the data acquisition board on the computer.

2.1.3. Operation

The driver, driven and expansion sections are filled with gases at given pressures before each test. Each flow condition corresponds to a pressure ratio of the three sections as shown in table 2.2.

The thickness of a diaphragm determines the maximum sustainable pressure difference between sections before a test. The pressure difference between the driven and expansion sections is typically less than 100 torr. Hence a thin foil (1 mil Mylar polyester) is used as the secondary diaphragm to minimize enthalpy loss during the diaphragm rupturing process. The primary diaphragms are polycarbonate sheets of various thicknesses depending on desired flow conditions and corresponding pressure ratios. The 12 × 12 inch polycarbonate diaphragms are scored in a cross-shape at the center to promote a clear break. The center of the diaphragm is aligned with the tube center by two pins, placed at the connection between the driver and driven sections, passing through two holes drilled at the corners of the diaphragm.

The rupture of the primary diaphragm is triggered by two methods: the pressurization of the driver section with helium gas, or the ventilation of the

Run Condition		1	2	3	4	5	6	7	8	9
Initial Pressures	Driver Section (psia)	45	67	177	195	206	225	274	404	615
	Buffer Section (psig)	-	-	75	75	75	85	110	165	235
	Driven Section (torr)	23	10	17	19	15	19	19	22	26
	Expansion Section (torr)	56	28	29	7	27	21	21	18	20
Freestream Conditions	Mach number	1.7 ± 0.03	2.0 ± 0.03	2.4 ± 0.05	2.4 ± 0.05	2.3 ± 0.05	2.5 ± 0.05	2.6 ± 0.05	2.9 ± 0.08	3.0 ± 0.08
	Simulated flight Mach number	5.0 - 5.5	6.0 - 7.5	7.5 - 8.0	7.5 - 8.5	7.0 - 9.0	7.5 - 9.0	8.0 - 9.0	8.5 - 9.0	9.0 - 10.0
	Stagnation enthalpy (MJ/kg)	1.0 ± 0.05	2.0 ± 0.05	2.4 ± 0.08	2.4 ± 0.08	2.6 ± 0.1	2.6 ± 0.1	2.9 ± 0.15	3.3 ± 0.15	3.8 ± 0.15
	Static temperature (K)	900 ± 30	1250 ± 50	1240 ± 50	1300 ± 50	1480 ± 50	1300 ± 50	1330 ± 50	1360 ± 50	1520 ± 70
	Static pressure (kPa)	25 ± 1	16 ± 1	18 ± 1	24 ± 1	25 ± 1	17 ± 1	23 ± 1	23 ± 2	24 ± 2
	Test time (μs)	700 ± 50	500 ± 50	350 ± 50	350 ± 50	300 ± 50	300 ± 50	300 ± 50	300 ± 50	200 ± 50
	Flow velocity (m/s)	1000 ± 20	1380 ± 25	1650 ± 30	1690 ± 30	1940 ± 40	1820 ± 40	2060 ± 40	2370 ± 65	2880 ± 65
	Freestream flow path length during the test time (m)	0.7	0.7	0.6	0.6	0.6	0.5	0.6	0.7	0.6
	Freestream Re_x upstream of jet injection nozzle: $X = 0.05 \text{ m} (\times 10^5)$	1.24	0.64	0.87	1.10	1.06	0.84	1.24	1.37	1.45
	Establishment length for laminar boundary layer upstream of jet injection nozzle : 3 X (m) (Davies and Bernstein 1969)	0.15	0.15	0.15	0.15	0.15	0.15	0.15	0.15	0.15
	Effective test time: test time - establishment length/flow velocity (μs)	550	390	260	260	220	220	230	240	150
	Boundary layer thickness upstream of jet injection nozzle (mm)	0.71	0.99	0.85	0.76	0.77	0.86	0.71	0.68	0.66
	Re_D of hydrogen jet: jet to freestream momentum ratio (J) = 4 jet nozzle diameter (D) = 2 mm ($\times 10^3$)	1.39	1.23	1.99	2.65	2.54	2.04	2.98	3.71	4.14

Table 2.2 Pressures of the three sections corresponding to flow conditions.

pressurized buffer section between the double diaphragms. Pressurization of the driver section starts with a signal from the expansion tube control system which operates valve module #1 in Fig. 2.3 (driver gas inlet) and ends with a rupture of the primary diaphragm. The time duration taken for the pressurization process, usually a few seconds, is not easily controllable. Therefore, the control signal (the signal opening valve module #1) is inappropriate to be a reference signal because the reference signal should precede the rupture by a fixed time frame to obtain repeatable laser diagnostics results. A method used in this study is to generate a pulse as a reference signal when the driver section pressure exceeds a given threshold. A process controller (Omega) connected to a pressure transducer (Setra, Model 280E) at the driver section is utilized to monitor the pressure and to generate the reference signal. Alternatively, the double diaphragm configuration is convenient to set a precise diaphragm rupturing time relative to a control signal (ventilation valve (valve module #8) open signal). In the double diaphragm configuration, there is a spacer (buffer section) between the two diaphragms where the gas within it can be pressurized or ventilated. The first diaphragm dividing the driver section and the buffer section ruptures when the pressurized buffer section is ventilated. Then the shockwave induced by the rupture breaks the second diaphragm dividing the buffer section and the driven section, almost instantaneously. The time delay of diaphragm rupturing from the ventilation valve (valve module #8) open timing is minimized and fixed by adjusting the pressure difference between the driver and buffer section.

2.2. Jet in Crossflow Model

A jet in crossflow model (Fig. 2.4 (a): a cavity model) is installed in the test section. The model, simulating a wall of a supersonic combustor in a scramjet engine, is a rectangular aluminum plate (5.5 × 4 inch, 1 inch thickness) containing jet injection nozzles, electrodes and a ceramic plate embedded for electrical insulation of the electrodes. Figure 2.4 (b) shows a bottom view of the model. Four aluminum legs of half inch thickness and 3 inch height hold the models and two outer legs supports a

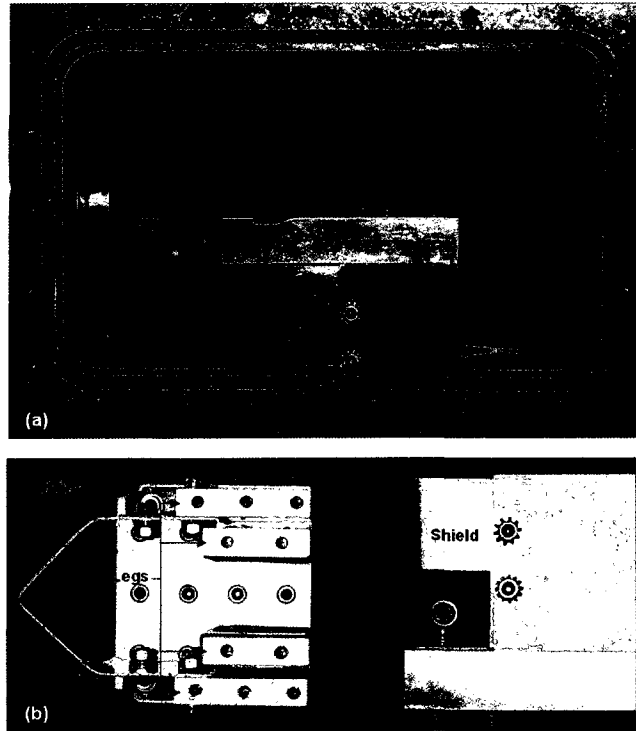


Figure 2.4 (a) A cavity model installed in the test section and (b) the bottom view of the model.

steel shield protecting the tubes, cords and connectors from the high enthalpy supersonic flow. The shield front is triangular-shaped (when viewed from the top) to reduce shock impact and drag. The model is fastened to the top of the basement legs. A heat treated 22° angle sharp leading edge (A2 tool steel) is attached on the front side of the model flush with the upper surface.

The four models tested in this study include a cavity model, a flat wall model with a single fuel jet injection nozzle, and two flat wall models with dual fuel jet injection nozzles. The two dual fuel jet injection models have different upstream jet injection angles. Details of the models are described in following sections.

2.2.1. Cavity Model

One of the most frequently used flame stabilization methods in the supersonic environment is the use of a cavity as introduced in the section 1.2.3. Ben-Yakar et al.

(2001) provided an overview of research pertaining to this method of flame stabilization. Certain characteristic cavity dimensions determine important flow parameters. For example, the flow residence time within the cavity is largely determined by the depth of the cavity (D); the mass entrainment rate by the cavity length (L); and the drag coefficient by the ratio of L/D. The overview of Ben-Yakar (2001) suggested that a cavity of 7 – 10 L/D ratio can serve as an adequate flame holder for a range of flow conditions: Ben-Yakar et al. have shown cavity flames stabilized in the supersonic flows of enthalpies higher than 4 MJ/kg. In addition, D should be determined considering a required flow residence time for ignition and flow speed – faster flow and longer ignition delay time (required flow residence time) demand a deeper cavity, while L should be chosen to provide a sufficient volume of radical production for flame propagation into the freestream.

A schematic and photographs of the cavity model are presented in Fig. 2.5. For this model, plasma-assisted flame stabilization is studied with electrodes inserted within the cavity. A ratio of $L/D = 7$ with $L = 21$ mm and $D = 3$ mm, is chosen following the guidelines of Ben-Yakar et al. (2001). As shown in Fig 2.5 (a), the front step of the cavity is vertical while back step is inclined by 25° from the horizontal plane. The cavity shaped groove perpendicular to the freestream flow direction is machined into the surface of the model (see Fig. 2.5 (b): top view of the model). Also, a cavity shaped 2×4 cm ceramic (Cotronics, 960 machinable alumina) plate with two holes (1 mm diameter) for electrode insertion is embedded at the center of the groove to electrically insulate the electrodes (1 mm diameter, 2 % thoriated tungsten rods) shown located within the cavity. The front side (2 cm width) of the ceramic plate is matched to the front step of the cavity. The electrodes, separated by 3 mm, are aligned parallel to the freestream flow direction and inserted to be flush with the ceramic plate. The upstream electrode is used as the cathode and is positioned 8 mm downstream of the front step. The oblique jet injection nozzle (1 mm diameter), angled 30° from the horizontal plane (pointing toward the downstream direction), is located 3 mm upstream of the front step of the cavity. The nozzle and two electrodes are on the streamwise directed center line of the model.

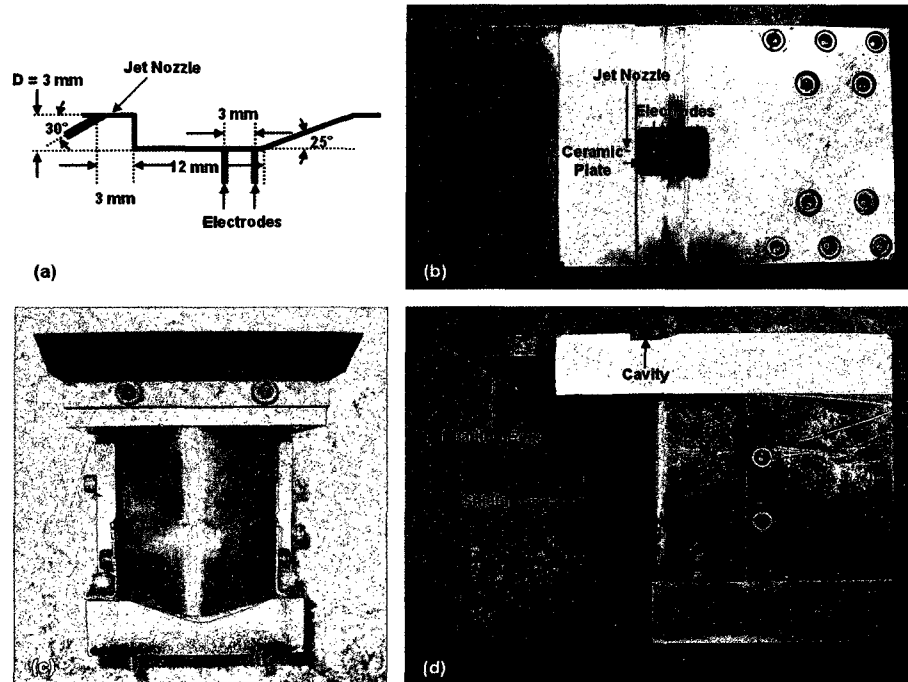


Figure 2.5 Pictures of a cavity model: (a) a schematic of the model, (b) top view, (c) front view, and (d) side view.

2.2.2. Flat Plate Model

A schematic and pictures of a flat plate model are shown in Fig. 2.6. The model has a flat surface without any geometric alteration such as a cavity. In this study, the electrodes are located flush with the model surface. Either a single nozzle (single fuel jet injection model) or two nozzles (dual fuel jet injection model) of 2 mm diameter and the two electrodes (1 mm diameter, 2 % thoriated tungsten rods) are aligned along the center line of top surface of the model oriented parallel to the freestream flow.

Single fuel jet injection model: A transverse jet injection nozzle and two electrodes are inserted through three holes of a 5 × 6.5 cm ceramic plate (Cotronics, 960 machinable alumina) embedded in the aluminum model. The nozzle, electrodes and the ceramic plate are flush with the surface of the model to avoid disturbing the

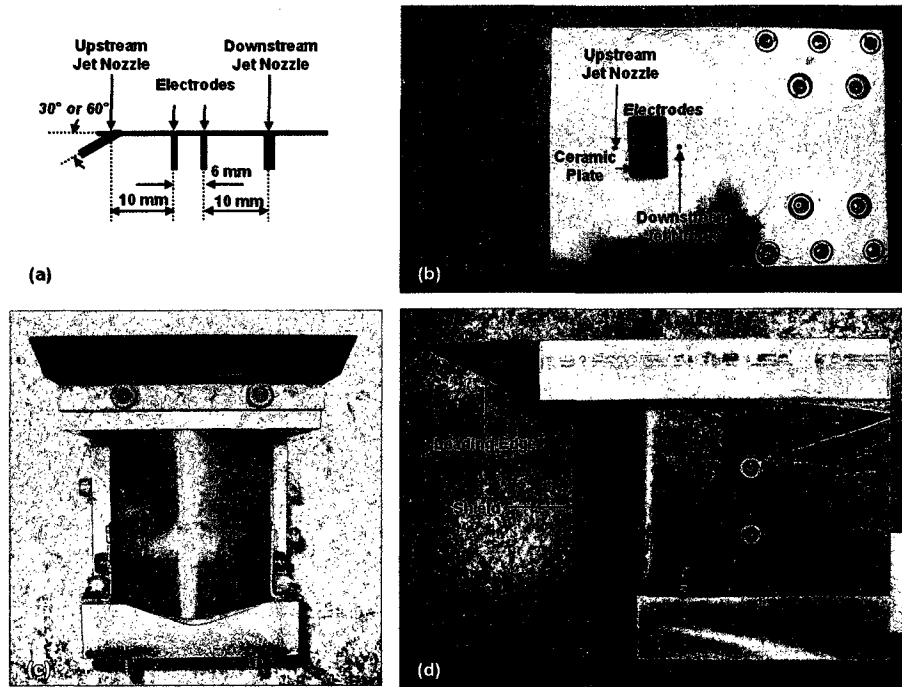
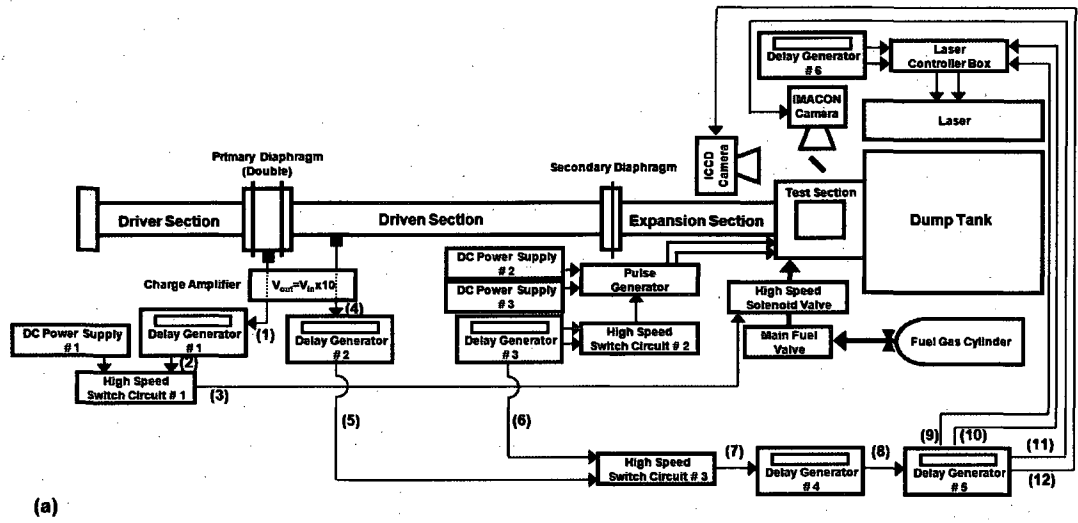


Figure 2.6 Pictures of a flat plate model: (a) a schematic of the model, (b) top view, (c) front view, and (d) side view.

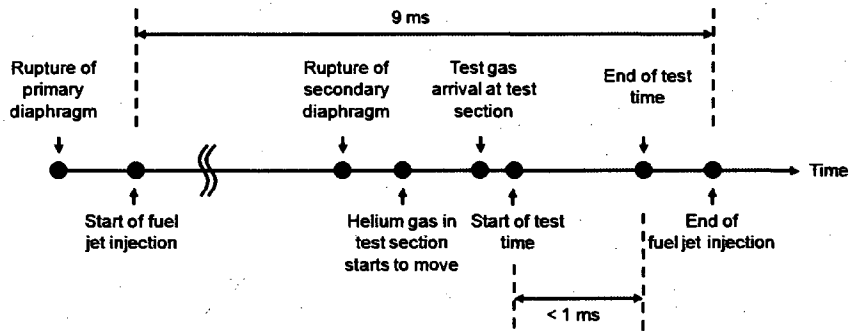
flow and generating shockwaves. The nozzle (2 mm diameter) is 14 mm upstream of the cathode and the anode is 6 mm downstream of the cathode.

Dual fuel jet injection model: An upstream oblique jet injection nozzle (2 mm diameter), two electrodes and a downstream transverse jet injection nozzle (2 mm diameter) are aligned on a streamwise directed center line of the model's surface (see Figs 2.6 (a) and (b)). The injection nozzles are drilled holes in the aluminum plate separated by 26 mm. A ceramic plate (1.5 × 2.5 cm) with two holes for accommodating the electrodes separated by 6 mm is embedded between the two nozzles. Similar to the single fuel jet injection model, the ceramic plate and the electrodes are flush with the surface of the model. The upstream jet injection nozzle is positioned 1 cm upstream of the nearest electrode.

2.2.3. Fuel Delivery System



(a)



(b)

Figure 2.7 (a) A schematic of the fuel delivery system and the expansion tube synchronization system - (1) through (12) are the signals described in Figs 2.8 (a) through (l), respectively, and (b) timing diagram of events occurring during an expansion tube operation.

Figure 2.7 (a) shows a schematic of the fuel delivery system and the expansion tube synchronization system. A fast response fuel injection/delivery system is essential for this study due to the short test time (typically, a few hundred microseconds) of the expansion tube. Therefore, a custom made high speed solenoid valve is used for fuel jet injection. Additionally, for safety, a second fuel valve (Parker, solenoid valve) is installed between the compressed fuel gas cylinder and the high speed solenoid valve. This fuel valve is opened by a manual switch just before a run to fill the tube upstream of the solenoid valve with compressed fuel gas.

The timing diagram of the systems is presented in Fig. 2.8. The signal from the pressure sensor at the buffer section (Fig. 2.8 (a)) is used as a fuel injection trigger signal, 10 times amplified by a charge amplifier (PCB Piezotronics, Model 482A16). The voltage peak from the sensor is caused by a sudden pressure rise due to a shockwave passing through the buffer section. The 50 V DC power supply (#1 in Fig. 2.7 (a), Tektronix, PS281) actuating the solenoid valve is connected to a high speed switch circuit (#1 in Fig. 2.7 (a), see Appendix A) of a MOSFET. The output of the circuit is connected to the solenoid valve. The control signal (Fig. 2.8 (b)) of the switching circuit is generated by a delay generator (#1 in Fig. 2.7 (a), SRS, DG 535) receiving a triggering signal (Fig. 2.8 (a)). 50 V DC is applied to the solenoid valve for 9 ms (Fig. 2.8 (c)) as soon as a shockwave is detected at the buffer section. The valve opening duration is set to 9 ms for safety reasons (see Fig. 2.7 (b)), to maintain a fuel concentration in the expansion tube to values lower than the lean flammability limit. A longer valve opening time results in extra fuel injection into the tube after the end of the test time.

The solenoid valve is located outside of the test section to avoid disturbances caused by plasma induced electromagnetic interferences (see Appendix C). Also, a Faraday cage made of aluminum plates houses the valve, because the solenoid valve is found to be particularly vulnerable to electromagnetic interference. On the other hand, the length of the fuel delivery tube between the solenoid valve and the jet injection nozzle is a crucial factor determining the response time of the fuel delivery system. Therefore, the length is minimized to approximately 25 cm. Since it is found that it

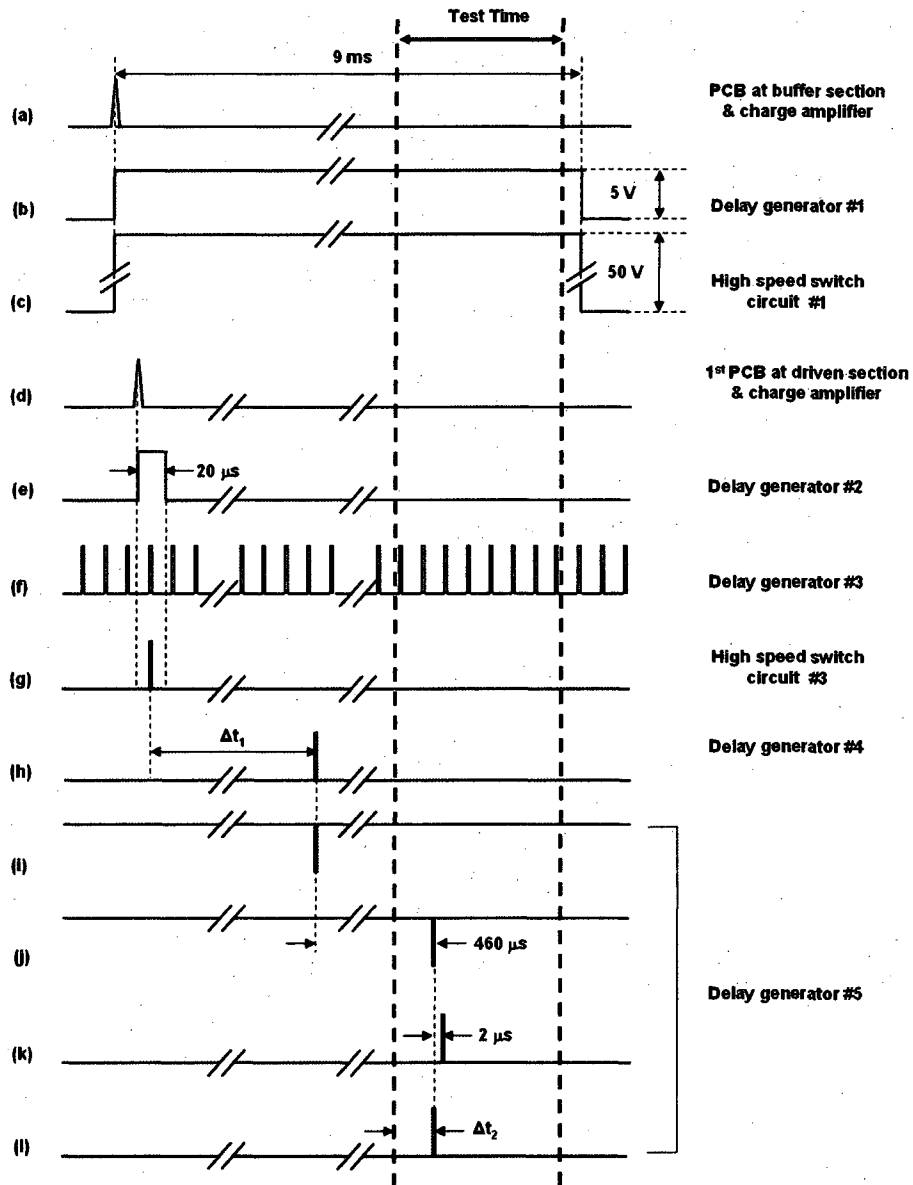


Figure 2.8 Signals of synchronization equipments.

usually takes 7 - 9 ms from the trigger time until the beginning of the test time (the arrival of test gas at the test section), the response time of the fuel delivery system should therefore be shorter than 7 ms. The resulting response time of the system for a fully developed fuel jet at the nozzle exit is estimated to be 6.5 ms (just within the 7-9 ms window) with 1300 psi hydrogen upstream pressure.

Two (or one for the single jet studies) feed-through holes of the test section are used to connect the solenoid valve to the two (or one) jet injection nozzles of the model installed inside the test section. For the dual fuel jet injection model, the gas fuel flow discharged from the solenoid valve is distributed to the two nozzles by a tee connector outside of the test section. The fuel injection is controlled by two manual valves at the two feed through holes for independent establishment of flow rates.

2.3. Plasma Generation System

A pulsed plasma is produced by high voltage pulses (typically 15 kV peak voltage, 10 ns pulse width and 50 kHz repetition rate) applied between two electrodes (2 % thoriated tungsten rods). The cathode is negatively biased (- 7.5 kV) while the anode is positively biased (+ 7.5 kV) at the peaks of the pulses. The voltage pulses are formed by a pulse generator (FID Technology, Model F1112, see Appendix B) powered by two DC power supplies and triggered by a high speed switching circuit (#2 in Fig. 2.7 (a), see Appendix A). A high voltage DC power supply (#2 in Fig. 2.7 (a), Sorensen, Model DCS600-1.7E) provides the main power consumed by the plasma and the plasma generation system. A supplemental DC power supply (#3 in Fig. 2.7 (a), HP, Model 6264B) is used for providing power to a refrigeration system for cooling the pulse generator. The high speed switching circuit produces 20 V peak voltage and 100 ns pulse width trigger signals for the pulse generator. A specialized delay generator (#3 in Fig 2.7 (a), SRS, Model DG535) equipped with a high voltage (up to 35 V) signal output generates 20 V long pulses (pulse width is fixed at 10 μ s) as well as TTL (5 V pulses with variable pulse width) control signals for the switching circuit. The switching circuit chops the long pulse (20 V, 50 kHz and 10 μ s pulse

width) to be short pulses of 100 ns pulse width gated by the TTL (5 V, 50 kHz and 100 ns pulse width) signals.

A maximum output power of the plasma generation system is used in this study, estimated to be 10 – 15 W. The power supplied by the main DC power supply (#2) is approximately 40 W. Voltage and current traces are recorded using a high voltage probe (Tektronix, Model P6051A) and a fast response Rogowski coil (Pearson current monitor, Model 2877), respectively.

Two feed through ports of the test section are used for high voltage cable electrical connections between the two electrodes of the model and the plasma generation system (located outside of the test section).

2.4. Synchronization System

A synchronization system (Fig. 2.7 (a)) built on the expansion tube facility is designed to control diagnostic equipment such as lasers, cameras and a pulsed light source of a Schlieren system. Figure 2.8 depicts the communication between the various units of the system. There are two major constraints in the timing system. One is the delay needed beyond the firing of the discharge to avoid interference from the strong plasma emission, and second, to trigger the laser system such that the measurement resides within expansion tube test time.

The pulsed plasmas are produced repetitively (at 50 kHz repetition rate) by high voltage pulses (10 ns pulse width). The plasma decays (recombines), typically, within a hundred nanoseconds, depending on species, pressure and temperature. Spontaneous fluorescence of excited species in the plasma is found to be much brighter than laser induced fluorescence (LIF) and radical (e.g. OH) emission in the absence of the plasma. Therefore, OH planar laser induced fluorescence (PLIF) and OH emission spectroscopy are conducted in between plasma pulses to study kinetics associated with combustion reactions and not that directly attributable to plasma excitation.

Measurements also need to be conducted in a window in time in which a supersonic test gas of a desired condition is flowing through the test section. Arrivals of test gas and rarefaction waves at the test section are the start and the end of the test time, respectively. The arrival times are measured by a pitot tube set in the test section.

A MOSFET based high speed switching circuit (#3 in Fig. 2.7 (a), see Appendix A) is utilized to satisfy both of the constraints by correlating the plasma pulse timing and the shock wave arrival time at a pressure sensor (precedes the start of the test time by a given time) in the driven section. The circuit receives a gate signal (Fig. 2.8 (e)) and plasma pulse signals (Fig. 2.8 (f)) to select a representative plasma pulse. The plasma pulse signals are from the delay generator #3 while the gating signal is generated by a delay generator #2 (SRS, Model DG535) as soon as a shock is detected at the first pressure sensor of the driven section (Fig. 2.8 (d)). Only one pulse (Fig. 2.8 (g)) can pass through the circuit during a 20 μ s period of the gating signal that activates the circuit. The selected pulse signal is delayed by a time interval (Δt_1) using a second delay generator #4 (SRS, Model DG535) to arrange the resulting trigger signals (Fig. 2.8 (j), (k) and (l)) within a test time. The resulting signals can be synchronized with a plasma pulse, if the time delay ($\Delta t_1 + 460 \mu$ s, where 460 μ s is the time separation between the flash lamp and the Q-switch of the Nd:YAG laser) is a multiple of the plasma pulses' period (20 μ s at 50 kHz repetition rate); a time (usually, 1 μ s; a time duration longer than plasma residence time) is added further to avoid coinciding with plasma pulses. The delayed pulse (Fig. 2.8 (h)) triggers a delay generator #5 (BNC, Model 555) to produce 4 signals needed to trigger the flash lamp (Fig. 2.8 (i)), Q switch (Fig. 2.8 (j)) of the Nd:YAG laser (Continuum Precision, Model PL8000), an intensified camera (Andor, iStar ICCD) (Fig. 2.8 (l)), and an ultra fast framing camera (Imacon 486 intensified CCD camera) (Fig. 2.8 (k)), respectively.

An additional synchronization is also needed to maintain a steady lasing power of the pulsed Nd:YAG laser. Laser specifications indicate that 10 Hz is an optimized lasing repetition rate for maximum laser power. Therefore, a pulse generator (#6 in Fig. 2.7 (a)) keeps the laser running at 10 Hz repetition rate until a fixed time (a few hundreds milliseconds) before a test begins: two 10 Hz signals separated by 460 μ s are

generated for the flash lamp and the Q-switch, respectively. A reference signal (explained in section 2.1.3) generated ahead of the bursting of the primary diaphragm stops the 10 Hz lasing and sets the laser ready to receive external signals from the delay generator #5. A toggle switch of a laser controller box turns the system on and a controller (NCC, Model T1K-1-461) in the box, triggered by the reference signal, switches the laser input from delay generator #6 (continuous 10 Hz lasing) to delay generator #5 (one lasing event per test). The intensified camera is synchronized with the lasing time (Q-switch trigger) for OH PLIF while the ultra fast framing camera for Schlieren imaging is triggered 2 μ s after the lasing time to avoid interference from the laser.

Most of the synchronization electronics is located to be approximately 20 m from the plasma generation system. Electromagnetic interference originating from the plasma generation system is strong enough to affect signals to be synchronized with the plasma pulse. Therefore, equipment vulnerable to the electromagnetic interference (high speed trigger circuits and delay generators) is moved into an adjacent room.

2.5. OH PLIF/Emission Spectroscopy System

Both OH planar laser induced fluorescence (PLIF) and OH emission spectroscopy are used to visualize the OH radical distribution. The characterization of excited (emission spectroscopy) and ground state (PLIF) OH distribution provides a qualitative indicator of the presence of combustion and the location of the flame region. A Nd:YAG laser (Continuum Precision, Model PL8000) that pumps a dye laser (Lumonics, Model HD-500) equipped with a frequency doubling unit (Lumonics, Model HyperTRAK-1000) for generating 3 – 7 mJ per pulse at 283 nm (10 Hz repetition rate), is used to excite the A-X(1,0) Q1(7) electronic transition of the OH molecule. LC5900 rhodamine 6G (Lambda Physics) dye (producing an output laser beam that peaks at a wavelength of 580 nm) is used with methanol as the solvent (53 mg per liter) for the dye laser. Five 2 inch diameter 266 nm reflectors guide the laser beam to the test section. The laser beam is transformed into a thin sheet by a set of

cylindrical concave and spherical convex lenses. The sheet of the laser beam is projected vertically, through a quartz window on the upper face of the test section, on the center line of the model's surface, in a plane coincident with the electrodes and jet injection nozzles. The location of the laser beam waist, adjusted by moving the spherical convex lens, is positioned to coincide with the surface of the model. The region of interest of a PLIF experiment (4 cm width) is determined by repositioning the cylindrical concave lens upstream of the spherical convex lens since the sheet of the laser beam becomes wider as the cylindrical lens moves further upstream. The spectrally filtered (using a narrow band pass filter from 305 to 325 nm) laser induced fluorescence is captured by an intensified camera (Andor, iStar ICCD) at right angles to the plane of the laser sheet. Spontaneous OH emission is also captured by the camera in the absence of the laser along the same direction but with a narrower band pass filter (10 nm wide) centered at 313 nm. The limiting resolution of these images is approximately 80 μm , estimated from the camera array size of 512×512 pixels imaged onto a 40×40 mm region of the flow. The images depict noncalibrated OH excited state and ground state concentration fields, which serve to provide a qualitative depiction of the flame structure. Typically, two or three OH PLIF images are taken in most of the cases to confirm the repeatability.

The intensity of the laser induced fluorescence is maximized by tuning the output wavelength of the frequency doubling unit. A methane diffusion flame burner is used as a continuous OH radical source for optimizing the wavelength of the laser. A photomultiplier, viewing the flame from the normal direction to the plane of the laser sheet, powered by a 700 V DC power supply (Power Design Inc., Model 3K10B) monitors the intensity of OH fluorescence filtered by a band pass filter centered at 313 nm. Two sequential peaks are detected separated by approximately 100 ns: the first peak caused by direct scattering from the laser beam precedes the second peak - the laser induced OH fluorescence. The intensity of the second peak is maximized by tuning the wavelength.

2.6. Schlieren System

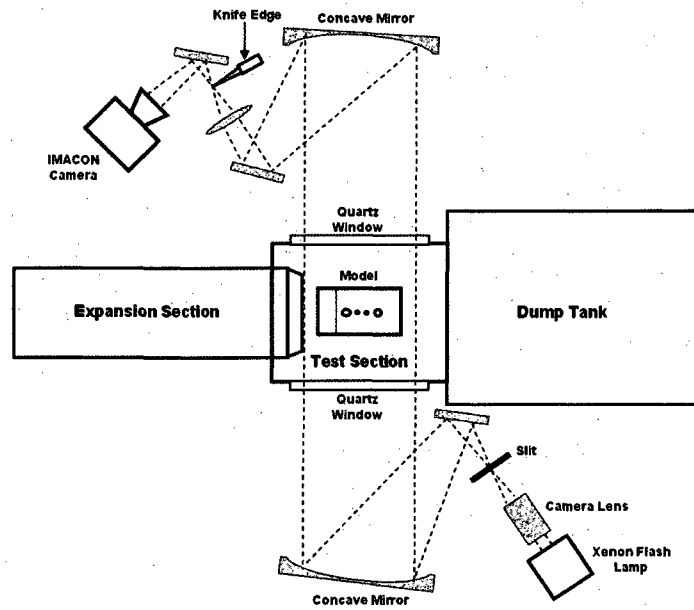


Figure 2.9 A schematic of the Schlieren system.

Schlieren imaging (Settles (2006)) is carried out with an ultra fast framing camera (Imacon 486 intensified CCD camera) and a pulsed xenon flash lamp (Hamamatsu, Model E6611). The camera can record eight frames at a maximum frame rate of 100 MHz. Schlieren imaging enables the visualization of flow features that lead to sudden changes in the refractive index, such as compressible shear layers and shock waves. Schlieren imaging is also used to determine the sonic jet momentum by characterizing the position of the sonic jet's Mach disk formed by its injection into a static ambient gas.

The configuration of the Schlieren system is shown in Fig. 2.9. The fast framing camera triggers the xenon flash lamp as soon as the camera receives a trigger signal (Fig. 2.8 (k)) from the synchronization system. Then, eight images are taken with different time delays and exposure times. The light from the flash lamp passing through a horizontal slit (5×1 mm) is adjusted to fill a concave mirror (Edmund Scientific, 8 inch diameter) using a camera lens (Vivitar, 205 mm). Two 8 inch diameter concave mirrors facing each other separated by 4.5 m make a parallel light beam passing through two quartz windows on both sides of the test section. The light,

focused onto a knife edge by the second concave mirror and a spherical convex lens, is cut in half horizontally using the knife edge and is then projected onto the CCD array of the fast framing camera.

Chapter 3 Plasma Assisted Cavity Flame Stabilization

In this chapter, experimental results are presented for flame stabilization of a fuel jet in crossflow with a cavity embedded into the model wall.

3.1. Application of a Pulsed Plasma in a Cavity

Cavity flame stabilization is one of the most widely used flame stabilization methods in supersonic flow environments. A cavity, or a typical recess in a combustor's wall, produces a recirculation zone where the flow residence time (τ_{res}) is longer than that in the supersonic freestream region. The extended τ_{res} and fuel/oxidizer mixing facilitated by the recirculation zone are beneficial for flame holding and propagation in supersonic environments. Another common example of where a recirculation zone is used to enhance flame stability is in a subsonic flow with the use of a bluff body such as V gutters in the afterburner of a turbojet engine. Such a method of recirculation is not suitable for supersonic flow. In the case of a supersonic combustor, a bluff body would induce strong normal shockwaves resulting in excessive stagnation pressure loss. A wall cavity has become more favorable, in that a cavity induces oblique shockwaves near the surface of the combustor, which result in less losses.

In this study, cavity flame stabilization is combined with the application of a pulsed plasma that is generated within the cavity itself. It is noteworthy that in the absence of recirculation of the flow, in a supersonic combustor, τ_{res} can be shorter than the inherent ignition delay time (τ_{ign}) of a fuel. The τ_{res} of a fuel/oxidizer mixture in a combustor is limited by the supersonic flow speed as well as the restricted flow path length. In typical flow and combustor scales, the mixture would not be ignited. The application of a pulsed plasma serves to reduce τ_{ign} while the addition of the cavity serves to lengthen τ_{res} . Consequently, when combined, these two modifications are expected to greatly enhance flame stability.

3.2. Oblique Fuel Jet Injection

An oblique injection nozzle (1 mm diameter) is installed upstream of a cavity to inject fuel into the supersonic flow. This oblique jet serves to enhance fuel/freestream flow mixing in comparison to the case of fuel injection inside the cavity. Oblique fuel jets are more frequently used in cavity flame stabilization than transverse jets because of several distinguishing advantages. The bow shock induced by an oblique fuel jet (inclined towards the downstream direction) is weaker than that of a transverse jet. The weaker shock causes less of a stagnation pressure loss. Additionally, it leads to a greater concentration of fuel within the cavity because the fuel jet trajectory is closer to the cavity than that of a transverse jet. Particularly for high J values (here, J is the momentum ratio of the jet to a freestream flow), the fuel jet penetration of a transverse jet into a freestream flow can be too deep for the fuel to be entrained into the cavity, while the trajectory of an oblique jet would still be close to the cavity.

3.2.1. Development of a Sonic Jet

A set of time sequential Schlieren images depicting the time evolution of a hydrogen jet injected into the test section filled with static ambient air at 200 torr are presented in Fig. 3.1. The jet is inclined to 30° relative to the wall. The jet appears at the nozzle exit 2 ms after a high speed solenoid valve controlling fuel injection is triggered. Afterwards, the jet propagates into the ambient air and the jet propagation angle is different than the angle of the jet injection nozzle (30°) due to the oblique exit condition since the direction of the jet nozzle is not perpendicular to the plane of the nozzle exit. As a result, the shear layer between the jet and the ambient air develops asymmetrically (Longmire et al. (1992)). Consequently, the jet becomes more upright (approximately 45° from a horizontal plane) after a sudden expansion (1300 psi hydrogen gas is supplied to the injection valve) at the nozzle exit. A barrel shock structure is first observed 4 ms after the opening of the solenoid valve, and becomes

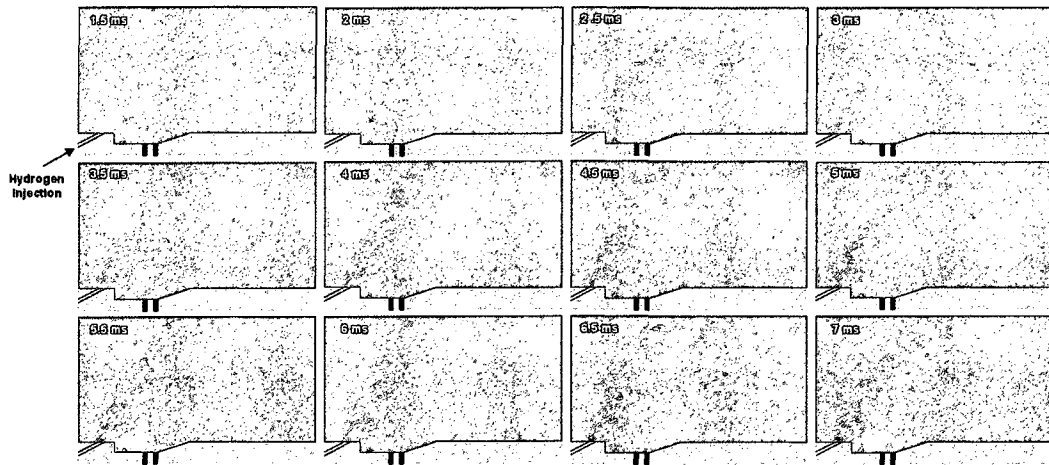


Figure 3.1 A set of time sequential Schlieren images describing an evolution of a hydrogen jet injected into a test section filled with static ($U_\infty = 0$) ambient air (200 torr).

complete and steady by approximately 6.5 ms. This suggests that the sonic jet is fully developed after 6.5 ms. Once fully developed, the location of the Mach disk at the top of the barrel shock structure can be measured to estimate the jet to freestream momentum ratio (J).

3.2.2. Jet Injection into a Supersonic Crossflow

Figure 3.2 (a) shows another set of time sequential Schlieren images illustrating the structure of the flow field with hydrogen jet injection and a cavity located downstream of the jet in the presence of a supersonic air freestream flow, $h_0 \sim 2.0$ MJ/kg (run condition 2 in table 2.2). The freestream flow direction is from left to right in all of the figures presented here. Before the beginning of the test time (0 μ s in Fig. 3.2 (a)), a fully developed hydrogen sonic jet starts to be curved towards the downstream direction by the helium gas flow that precedes the flow of the test gas. At the beginning of the test time (when the test gas arrives), three shockwaves (Fig 3.2 (b)), induced by (i) the jet injection, (ii) the front step and (iii) the inclined back wall

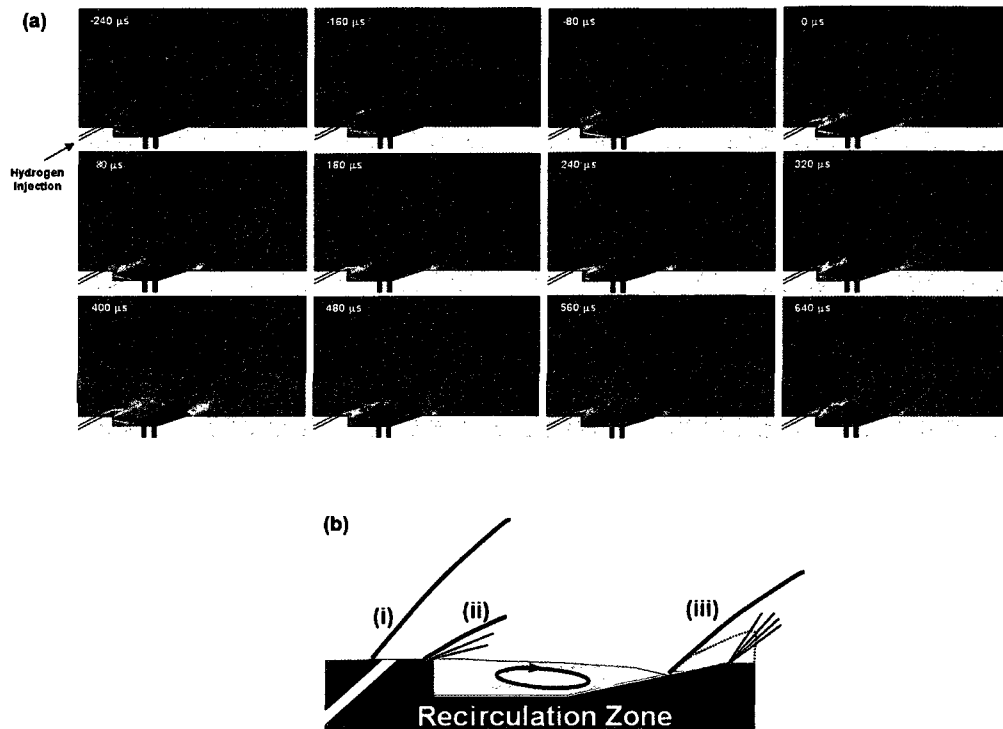


Figure 3.2 (a) A set of time sequential Schlieren images illustrating the flow field in the presence of a supersonic freestream flow (run condition 2: $Ma \sim 2.0$, $h_0 \sim 2.0$ MJ/kg, $T_{static} \sim 1250$ K, $P_{static} \sim 16$ kPa and $U_\infty \sim 1380$ m/s) with $J_n \sim 4.5 \pm 0.1$: the test time starts at $0 \mu s$ and ends at approximately $500 \mu s$, and (b) a schematic of three shock waves induced by (i) the jet injection, (ii) the front step and (iii) the inclined back wall of the cavity.

of the cavity, appear in the images. It is noteworthy that fluctuations in the angle of the first shockwave, induced by the jet injection, suggest unsteadiness in the freestream flow. This unsteadiness is distinctly unrelated to disturbances caused by complex flows in the vicinity of the cavity. Also, we observe that the jet trajectory of the fuel is bent over the shear layer of the cavity, promoting fuel entrainment across the shear layer into the cavity. As rarefaction waves and the helium gas flow from the driver

section arrives at the test section, the test time ends (at approximately 500 μ s) and the shockwaves vanish.

3.3. Jet Flame Ignition in a Cavity

A detailed description of the cavity model used in this study is presented in Section 2.2.1. As mentioned there, the cavity length (L: 21 mm) to the depth (D: 3 mm) ratio is 7 in accordance with the ratio recommended by Ben-Yakar et al. (2001). This type of cavity ($7 < L/D < 10$) is called an “open” cavity because a shear layer over the cavity reattaches on the back wall of the cavity, i.e., there is an open space in the cavity separated from a freestream region by the shear layer. Open cavities have reduced drag coefficient when compared to longer (larger L/D ratio) closed cavities, and tend to have higher mass exchange rate across the shear layer than that of shorter cavities.

3.3.1. Auto Ignition

Figure 3.3 presents OH PLIF images taken with different freestream flow conditions and jet momentum ratios (using component normal to the freestream flow, J_n , that is half of the total J due to the 30° injection relative to the horizontal plane). In Fig. 3.3 (a), we have $J_n \sim 3$, with $h_0 \sim 3.3$ MJ/kg (run condition 8) for the freestream air flow, (b) $J_n \sim 4.5$ with $h_0 \sim 2.9$ MJ/kg (run condition 7) for the air flow, and (c) $J_n \sim 5.5$ with $h_0 \sim 2.6$ MJ/kg (run condition 6) for the air flow. The images are taken 200 μ s after the beginning of the test time (the test time has a value of approximately 300 μ s

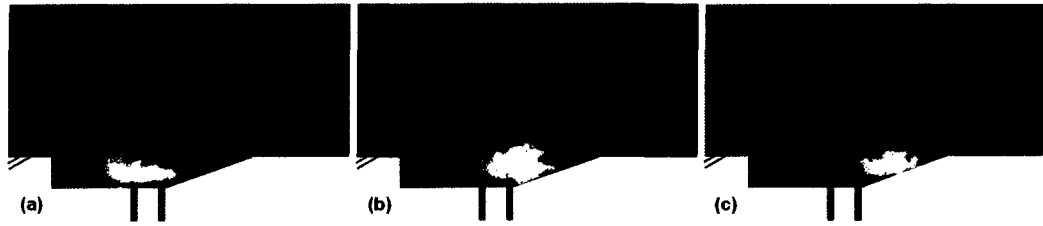


Figure 3.3 Three OH PLIF images showing auto-ignited hydrogen cavity flames in the absence of a plasma in supersonic flows of three different enthalpies: (a) run condition 8: $Ma \sim 2.9$, $h_0 \sim 3.3$ MJ/kg, $T_{static} \sim 1360$ K, $P_{static} \sim 23$ kPa and $U_\infty \sim 2370$ m/s ($J_n \sim 3 \pm 0.1$), (b) run condition 7: $Ma \sim 2.6$, $h_0 \sim 2.9$ MJ/kg, $T_{static} \sim 1330$ K, $P_{static} \sim 23$ kPa and $U_\infty \sim 2060$ m/s ($J_n \sim 4.5 \pm 0.1$) and (c) run condition 6: $Ma \sim 2.5$, $h_0 \sim 2.6$ MJ/kg, $T_{static} \sim 1300$ K, $P_{static} \sim 17$ kPa and $U_\infty \sim 1820$ m/s ($J_n \sim 5.5 \pm 0.1$).

at this flow condition). The ground state OH distributions shown in the images depict flame regions that are auto-ignited both inside and outside of the cavity. A filamentary flame is observed in the windward side of the jet (Figs 3.3 (a) and (b)) above the cavity while a stronger and broader flame is sustained in the cavity (Figs 3.3 (a), (b) and (c)). The two flames are separated by the trajectory of the fuel jet core where the fuel concentration is too high to be ignited. In studies conducted by Heltsley et al. (2006), filamentary flames are also observed in the windward side of jets in relatively high enthalpy flow conditions ($h_0 > 2.75$ MJ/kg) on a flat wall in the absence of a cavity with $J_n \sim 4$ and normal injection configurations. Coincidentally, the filamentary flames are not observed at lower enthalpy conditions (Fig. 3.3 (c): $h_0 \sim 2.6$ MJ/kg) in the current study because ignition of the filamentary flames depends on the strength of the upstream shockwave induced by the jet injection, and the shock strength increases as the flow enthalpy increases. These flames are seen to reside just behind the shockwave and are presumed to be ignited by the resulting temperature and pressure elevation. It is noteworthy that, no flame is observed in leeward side in the previous flat wall study of Heltsley et al. (2006) because the flow residence time (τ_{res}) is too

short to sustain a flame in that region in the absence of a cavity. Lower enthalpy cases are also investigated in the present study (as low as 1.0 MJ/kg, run condition 1). No detectable OH is observed in the cavity when the stagnation enthalpy of the freestream flow is lower than 2.0 MJ/kg (run conditions 1 and 2).

3.3.2. Ignition Delay of a Cavity Flame

Figure 3.4 shows a set of time sequential OH PLIF images, each separated by 40 μs , describing the time evolution of an auto-ignited flame in a cavity. The freestream flow condition is $h_0 \sim 2.9$ MJ/kg (run condition 7). A time $t = 0$ μs is used for reference, corresponding to the beginning of the test time. The first ignition event is observed to appear on the back wall of the cavity at 80 μs . This suggests that the cavity flame ignition delay time is approximately 80 μs . The ignition delay time

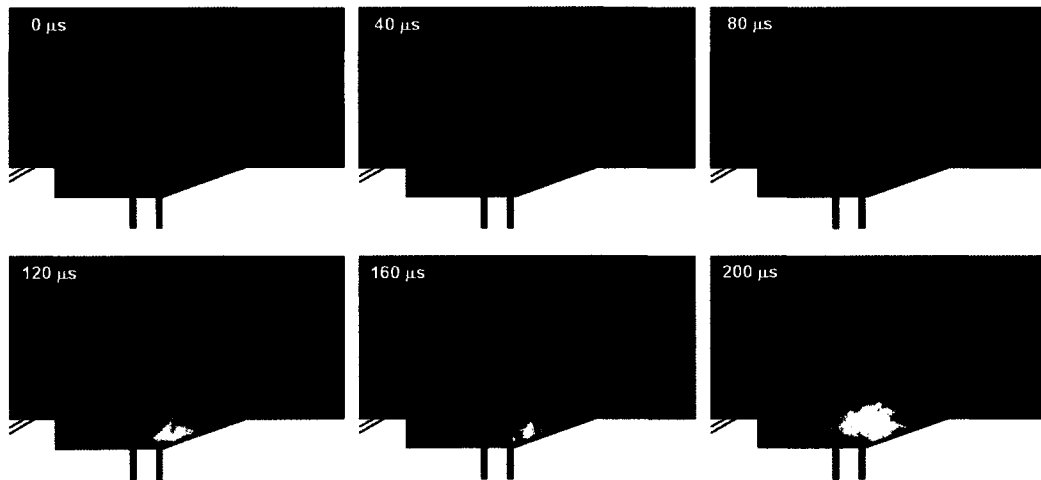


Figure 3.4 Time sequential OH PLIF images in the absence of a plasma separated by 40 μs with a supersonic crossflow (run condition 7: $Ma \sim 2.6$, $h_0 \sim 2.9$ MJ/kg, $T_{\text{static}} \sim 1330$ K, $P_{\text{static}} \sim 23$ kPa and $U_\infty \sim 2060$ m/s) and a hydrogen jet ($J_n \sim 4.5 \pm 0.1$).

referred to here (τ_{ign}) includes the mixing time and the time attributed to the kinetics of combustion reactions. In this specific configuration, complex gas mixing phenomena occur in the cavity because the expansion tube test section, where the cavity model is installed, is initially filled with helium gas before each test firing. Remnant helium gas trapped in the cavity would be mixed with the fuel/oxidizer mixture and then flows out across the cavity shear layer over. This mixing process takes a certain amount of time. However, it is noteworthy that a test run, taken with air instead of helium in the test section before the expansion tube operation, indicates that (including the helium mixing time) the test time is long enough to achieve steady combustion reaction in the cavity because no difference in flame propagation/stability is observed at a time of 200 μs in the two cases.

The cavity flame in these above cases is ignited due to the high enthalpy of the freestream flow. The high enthalpy appears to be sufficient to initiate combustion (the static temperature in the cavity and the boundary layer approaches the stagnation temperature of the freestream flow which typically exceeds 2000 K). This condition is referred to as auto-ignition. All of the freestream flows tested in this study are either high enthalpy, or high static temperature and are expected to ignite these flammable fuel gas mixtures after some finite time duration (τ_{ign}). The lowest static temperature condition generated in this study (run condition 1) is 900 K, which exceeds the auto-ignition temperature of hydrogen, known to be approximately 850 K (Alcock et al. (2001)). However, a cavity flame is not observed in this case. We attribute this to the short residence time. A flame can not be sustained if the flow residence time (τ_{res}) in the cavity is shorter than τ_{ign} . The ignition time will depend on the temperature of the flammable mixture. As the freestream flow enthalpy (or temperature) decreases, τ_{ign} will increase. A further discussion related to the temperature dependence of τ_{ign} (at a fixed pressure) will be presented within the context of model simulations in Chapter 5. The minimum enthalpy for sustaining a cavity flame is observed here to be approximately 2.0 MJ/kg (static temperature \sim 1250 K) in this study.

Some discussion is warranted about the structure of the flame propagation within the cavity. A close inspection of Fig. 3.4 reveals that the cavity flame initiates

near the back wall (at about 80 μs) and propagates both towards the front of the cavity and towards the freestream flow. However, we see that the flame does not appear to penetrate deep into the freestream flow. This limited flame propagation will be discussed in more detail in Section 3.5 below.

3.4. Plasma Effect on a Cavity Flame

The effects of a repetitively pulsed plasma (15 kV peak voltage, 10 ns pulse width and 50 kHz repetition rate) on cavity flames is investigated experimentally. The results of this study are presented in this section below. The pulsed plasma, when applied inside the cavity, is expected to initiate and enhance combustion reactions within the cavity. Dissociated and excited radical species produced by the plasma are expected to shorten the ignition delay time. A detailed discussion of the effects of plasma-dissociated species will be presented, with the help of a numerical simulation, in Chapter 5.

3.4.1. Cavity Flame Enhancement by a Pulsed Plasma Discharge

Figure 3.5 provides a comparison of auto-ignited cavity flames and plasma assisted cavity flames at two different flow conditions. Figures 3.5 (a) and (b) correspond to the case of $J_n \sim 4$ hydrogen injection and $h_0 \sim 3.3$ MJ/kg (run condition 8) air flow, while Figs 3.5 (c) and (d) correspond to $J_n \sim 3.5$ hydrogen injection and $h_0 \sim 2.9$ MJ/kg (run condition 7) air flow. All of the images are taken 200 μs after the beginning of the test time (approximately 300 μs test time at this flow condition). Figures 3.5 (a) and (c) are taken without the plasma, and (b) and (d) are in the presence of the plasma. Cavity flames in Figs 3.5 (a) and (c) are typical auto-ignited flames, residing primarily within the cavity, and with limited flame propagation into the freestream flow. The plasma enhanced cavity flames seen in Figs 3.5 (b) and (d) clearly appear to extend into the freestream flow on the leeward side of the fuel jets. The propagation of the plasma enhanced cavity flames are limited by the trajectories

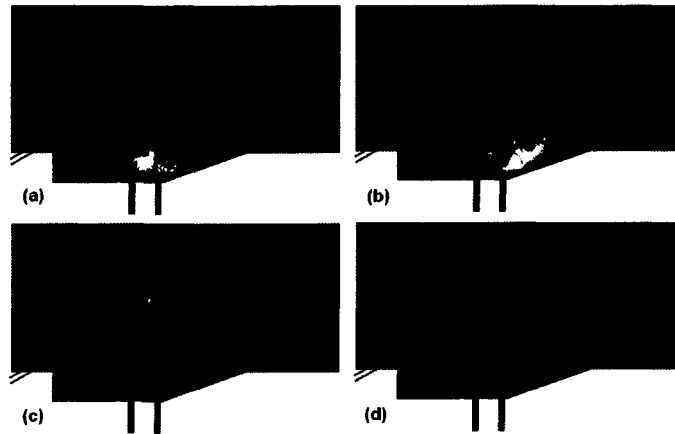


Figure 3.5 OH PLIF images of a cavity flame in supersonic flows of two different enthalpies: (a) without the plasma and (b) in the presence of the plasma in run condition 8 flow: $Ma \sim 2.9$, $h_0 \sim 3.3$ MJ/kg, $T_{static} \sim 1360$ K, $P_{static} \sim 23$ kPa and $U_\infty \sim 2370$ m/s (hydrogen jet, $J_n \sim 4 \pm 0.1$), and (c) without the plasma and (d) in the presence of the plasma in run condition 7 flow: $Ma \sim 2.6$, $h_0 \sim 2.9$ MJ/kg, $T_{static} \sim 1330$ K, $P_{static} \sim 23$ kPa and $U_\infty \sim 2060$ m/s (hydrogen jet, $J_n \sim 3.5 \pm 0.1$).

of the fuel jet cores. The fuel jet trajectory is an intrinsic limitation for flame propagation, setting a boundary of flammable regions in the flow.

The trailing flames that extend into the freestream flow provide compelling evidence that a flame holding is possible in these high speed flow regimes. As mentioned above, the flame tail resides on the leeward side of the fuel jet where the flow speed is much higher than the flow speed inside the cavity. A flame cannot survive the high speed flow in the absence of a cavity, as shown in the previous study conducted by Heltsley et al. (2006). This is despite the fact that the fuel is relatively well mixed with the freestream flow in that region. The fuel mixing (in the leeward side) of a jet in supersonic crossflow has been studied both experimentally (Fay et al. (2006)) and numerically (Kawai et al. (2007)). The flame tail can survive the high speed flow because the cavity flame and the pulsed plasma in the cavity serves as a source of heat and radicals, both capable of shortening the ignition delay time (τ_{ign}) of

the well mixed flammable mixture. The combustion mechanism can overcome the slowest initiation reaction producing radicals from a fuel/oxidizer mixture to make τ_{ign} shorter, if sufficient radicals are supplied to initiate branching/propagation reactions.

3.4.2. Reduction of Ignition Delay Time

Time sequential OH PLIF images presented in Fig. 3.6 depict the effect of the plasma on the cavity flame, through a reduction of ignition delay time (τ_{ign}) of the hydrogen jet flame inside the cavity. The images are taken in the presence of the pulsed plasma at the same freestream flow condition as in Fig. 3.4 (run condition 7). A comparison of Fig. 3.4 and Fig. 3.6 reveals two differences. The flame inside the cavity is clearly ignited at about 40 μs in the presence of the plasma, whereas it is seen to ignite at about 80 μs without the plasma (Fig. 3.4), indicating that τ_{ign} is shortened by approximately 40 μs due to the plasma. The pulsed plasma serves as a radical source in the cavity producing dissociated and excited species by high energy electron

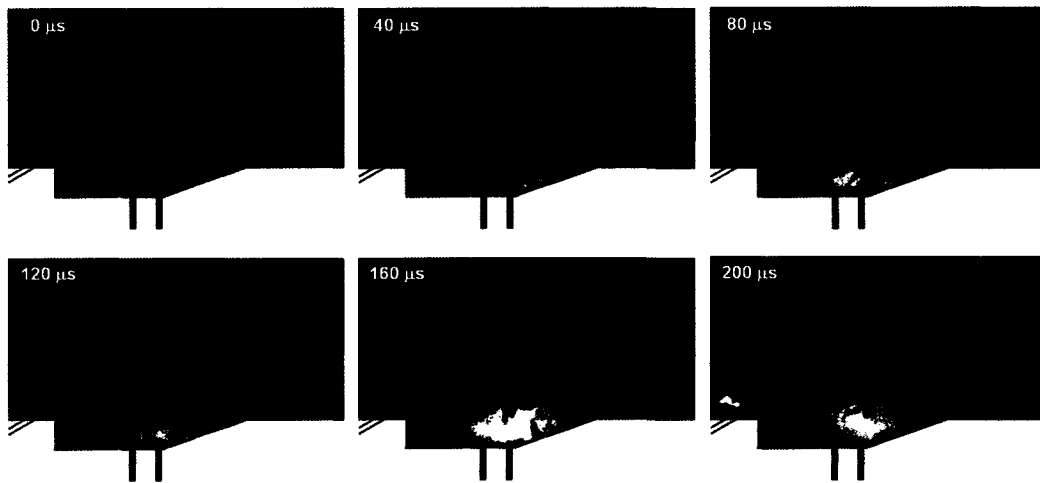


Figure 3.6 Time sequential OH PLIF images in the presence of a plasma separated by 40 μs in a run condition 7 flow: $\text{Ma} \sim 2.6$, $h_0 \sim 2.9 \text{ MJ/kg}$, $T_{\text{static}} \sim 1330 \text{ K}$, $P_{\text{static}} \sim 23 \text{ kPa}$ and $U_\infty \sim 2060 \text{ m/s}$ with a hydrogen jet ($J_n \sim 4.5 \pm 0.1$).

impact. An inspection of the images also reveals that the cavity flame initiates at the plasma region between two electrodes (which are depicted by two black solid lines at the bottom of the cavity in the 40 μs panel in Fig. 3.6), which implies that the plasma ignition is faster than the auto-ignition observed on the back wall of the cavity in Fig. 3.4 at 80 μs . As a result, the cavity flame that is ignited earlier propagates faster and deeper into the freestream flow compared to the auto-ignited flame.

An extreme case is tested in $h_0 \sim 2.0$ MJ/kg (run condition 2) air freestream flow under plasma enhancement. Figure 3.7 shows the OH PLIF image taken at 400 μs after the beginning of the test time (500 μs in run condition 2), and illustrates clearly, that a cavity flame can be ignited by the plasma enhancement. As mentioned in Section 3.3.1, auto-ignition is not observed during the test time at this flow condition. While the plasma enhancement leads to ignition, it should be mentioned that the absence of auto-ignition does not necessarily imply that ignition would not take place under sufficient test time. Two possible conditions influence the result depending on the test time duration. The first condition is (i) when the flow residence time (τ_{res}) inside the cavity is longer than the test time (τ_{test} , approximately 500 μs with run condition 2), and the second condition is (ii) when $\tau_{\text{test}} > \tau_{\text{res}}$. In the case of (i), cavity flame ignition is possible at some time later than the test time duration if τ_{ign} is shorter than τ_{res} ($\tau_{\text{res}} > \tau_{\text{ign}} > \tau_{\text{test}}$). However, in the case of (ii), a cavity flame will not



Figure 3.7 An OH PLIF image taken with a run condition 2 air flow: $Ma \sim 2.0$, $h_0 \sim 2.0$ MJ/kg, $T_{\text{static}} \sim 1250$ K, $P_{\text{static}} \sim 16$ kPa and $U_{\infty} \sim 1380$ m/s, and a hydrogen jet ($J_n \sim 2.5 \pm 0.1$).

be ignited because it is obvious that τ_{ign} is longer than τ_{res} ($\tau_{\text{ign}} > \tau_{\text{test}} > \tau_{\text{res}}$ OR $\tau_{\text{test}} > \tau_{\text{ign}} > \tau_{\text{res}}$). Regardless of the scenarios, cavity flame ignition would be observed if the pulsed plasma can make τ_{ign} shorter than the test time as well as τ_{res} in the cavity.

The OH PLIF image presented in Fig. 3.7 shows a cavity flame ignited by the pulsed plasma at the freestream flow run condition 2. It is noteworthy that a strong OH intensity region is observed adjacent to the cathode (region within the blue dotted circle in Fig 3.7). This is further evidence supporting theory that the plasma initiates ignition of the cavity flame. Most of the radicals produced by the plasma discharge originate from a small region very near the cathode (cathode sheath) because of the high energy electrons accelerated in that region. The high energy electrons are produced by a strong electric field induced by a voltage drop across the cathode sheath, while the voltage drop at the anode is correspondingly smaller in comparison to the cathode voltage drop (Wronski et al. (2005), Fabela et al. (2007), and Zissis et al. (2007)). Consequently, the cavity flame is ignited in the cathode region producing a combustion kernel that then propagates to fill the entire cavity region.

3.4.3. Ethylene Jet Flame Ignition

Similar studies were carried out with ethylene fuel injection to validate the applicability of this plasma-assisted combustion process to a broader range of hydrocarbon fuels of lower flame speed and longer ignition delay time. Figure 3.8 shows OH PLIF images taken without the discharge plasma (Fig. 3.8 (a)) and in the presence of the plasma (Fig. 3.8 (c)) with ethylene injection ($J_n \sim 3$). The freestream flow corresponds to run condition 7 ($h_0 \sim 2.9$ MJ/kg). The images are taken 200 μs after the beginning of the test time (of approximately 300 μs).

The OH PLIF signal observed from within the cavity in the absence of the plasma (Fig. 3.8 (a)) is comparable to the background noise intensity, whereas a flame is auto-ignited with hydrogen fuel jet injection ($J_n \sim 3.5$) under the same flow condition (Fig. 3.8 (b)). We attribute this difference to the general findings that the

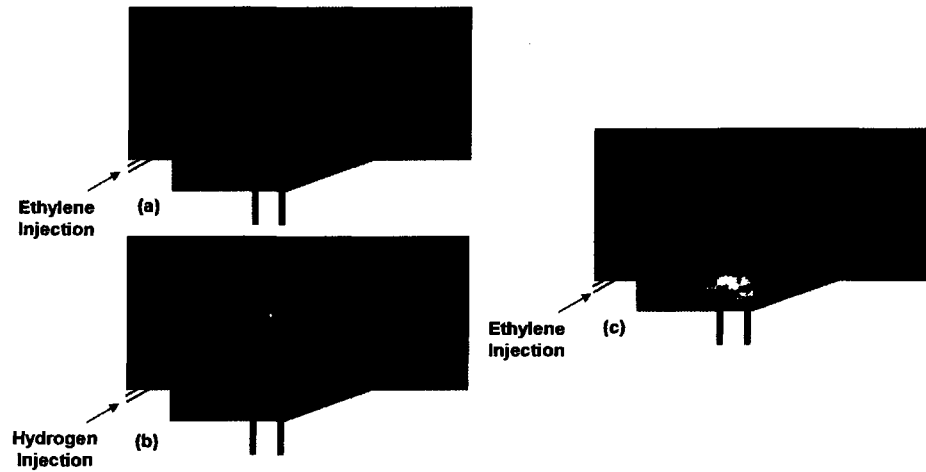


Figure 3.8 OH PLIF images taken with a run condition 7 air flow ($Ma \sim 2.6$, $h_0 \sim 2.9$ MJ/kg, $T_{static} \sim 1330$ K, $P_{static} \sim 23$ kPa and $U_\infty \sim 2060$ m/s) with an ethylene jet injection ($J_n \sim 3 \pm 0.1$): (a) without a plasma and (c) in the presence of the plasma, and (b) a hydrogen jet injection ($J_n \sim 3.5 \pm 0.1$) without the plasma.

ignition delay times (τ_{ign}) of hydrocarbon fuels (such as ethylene) are longer than those of hydrogen (Gokulakrishnan et al. (2006)). Therefore, flame holding in a supersonic environment is more difficult to achieve in the case of a hydrocarbon fuel injection compared to the hydrogen case.

Figure 3.8 (c) depicts a cavity flame of an ethylene fuel jet ignited by the pulsed plasma under the same conditions of Fig. 3.8 (a). Filamentary flames in the windward side of the jet as observed with hydrogen injection are not seen in the ethylene jet injection case. However, it is quite apparent that a flame is ignited inside the cavity and a tail of this flame propagates into the freestream flow. However, the extended flame does appear weak and filamentary in structure.

3.5. Effects of Jet Injection Momentum

As discussed in Section 3.4.1, jet injection momentum is one of several parameters that affect the propagation of the flame into a freestream flow. Flame propagation into the free stream is crucial to obtaining high combustion efficiency and the concomitant release of the maximum energy. In this section, we describe the results of studies of flame propagation in which the jet injection momentum is varied.

3.5.1. Jet Penetration

Figure 3.9 presents a set of Schlieren images depicting varying jet penetration into a freestream flow as a function of normal jet injection to freestream momentum ratio (J_n). The freestream flow corresponds to run condition 2 ($h_0 \sim 2.0$ MJ/kg). The momentum ratio, J_n , of a sonic hydrogen jet is varied from 2 to 10.5 at fixed injection angle of 30° . As shown in the images, jet penetration becomes deeper with increasing J_n . Deeper jet penetration is expected to extend the flame region out of the cavity as discussed in Section 3.4.1, only if the discharge plasma enhanced cavity flame provides enough seeding of radicals to ignite a well mixed fuel/oxidizer freestream.

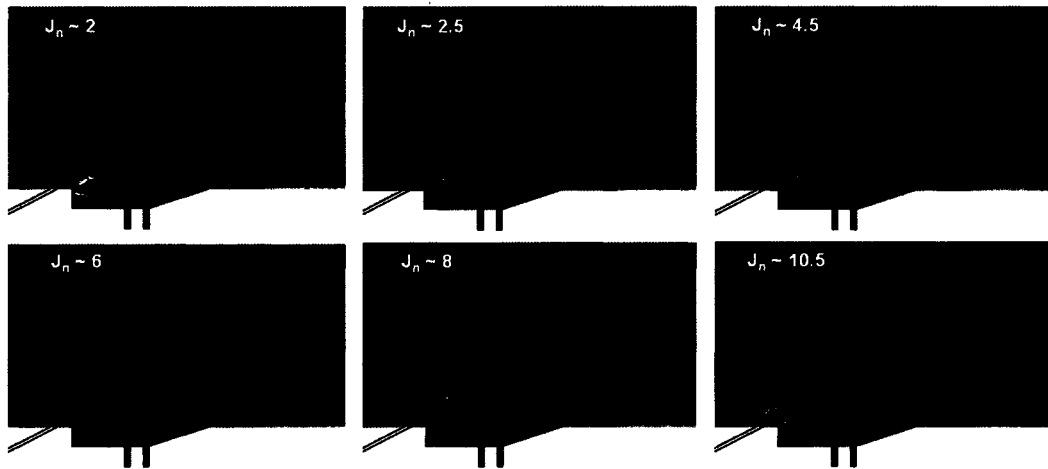


Figure 3.9 Schlieren images taken with a run condition 2 air flow ($Ma \sim 2.0$, $h_0 \sim 2.0$ MJ/kg, $T_{static} \sim 1250$ K, $P_{static} \sim 16$ kPa and $U_\infty \sim 1380$ m/s) and a hydrogen jet injection of varying J_n .

The increment of J_n also implies an increase in the fuel mass flow rate in addition to the increased jet penetration, which should also serve to increase the combustion energy release. Cavity flames captured for each of these values of J_n under the same flow condition are described in the next section.

3.5.2. Effects on Cavity Flames

OH PLIF images in Fig. 3.10 depict cavity flames that are ignited by the pulsed discharge plasma under the same flow conditions as in Fig. 3.9. All of the images are taken 400 μ s after the beginning of the test time (approximately 500 μ s test time in this case). The OH PLIF images have an adjusted scale to bring out the features, due to the overall weaker signal intensity when compared to the previous high enthalpy cases (e.g. run condition 8 or 7: $h_0 \sim 3.3$ or 2.9 MJ/kg). The intensity scale in Fig. 3.10 is approximately one seventh of that of Fig. 3.5. It is apparent from this figure that the lowest value of J_n (~ 2) produces the strongest flame in the cavity although the flame does not appear to propagate into the freestream flow. It seems as

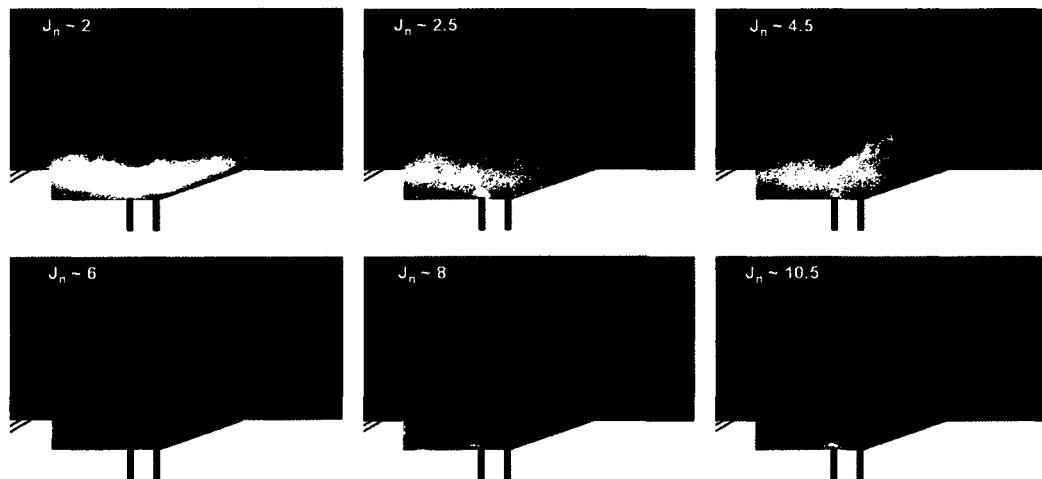


Figure 3.10 OH PLIF images taken with a run condition 2 air flow ($Ma \sim 2.0$, $h_0 \sim 2.0$ MJ/kg, $T_{static} \sim 1250$ K, $P_{static} \sim 16$ kPa and $U_\infty \sim 1380$ m/s) and a hydrogen jet.

though the flame boundary above the cavity is delineated by the trajectory of the jet core. As J_n is increased, the boundary of the flammable mixture region in the leeward side of the jet (the trajectory of the jet core) extends into the freestream region as shown in Fig. 3.9. However, cavity flame propagation into the freestream is still not very apparent with the higher J_n . Even more apparent is that the cavity flame becomes weaker with increasing J_n . This trend is attributed to a lower fuel concentration in the cavity with increasing J_n . We find therefore, that the cavity flame's role as a radical source to pilot flame propagation into the free stream diminishes with increasing J_n .

A fuel jet injection of high J_n values has merits as discussed in the previous section (3.5.1) although it also has a limitation lessening the role of the cavity flame as a radical source for flame propagation. Consequently, these two constraints opposing each other demand the choice of a moderate value of J_n , or the use of an alternative method of controlling two important roles of the fuel jet, namely the seeding of the cavity with fuels to produce, through combustion inside the cavity, a cavity flame that serves as an effective radical source; and the seeding of the freestream to produce a well mixed flow that facilitates the propagation of the cavity flame into the freestream. We have found that the lowest value of J_n that results in significant flame propagation behind the cavity is $J_n \sim 3.5$, as seen in Fig. 3.5 (d). On the other hand, relatively strong OH signal (indicative of strong combustion) is observed inside the cavity with J_n lower than 4.5, as seen in Fig. 3.10, although higher enthalpy conditions or a stronger plasma source would be required to ignite the whole flammable freestream region in this case. In short, an optimized choice of J_n between 3.5 and 4.5 would be preferred with the current cavity configuration.

3.6. Drawbacks of Cavity Flame Stabilization Methods

As observed in the previous sections, the cavity flame stabilization method combined with the use of a pulsed plasma discharge was successful in igniting/sustaining flames within the cavity. Nevertheless, drawbacks associated with this method were also found. These include stagnation pressure loss caused by cavity

induced shockwaves and localized flame holding adjacent to the cavity (i.e., the lack of flame propagation into the freestream). This section briefly reviews these drawbacks.

3.6.1. Stagnation Pressure Loss

An inherent disadvantage in the use of cavity flame stabilization methods (with or without plasmas) is a stagnation pressure loss caused by the cavity. In general, any shockwave present in the inlet to, or within a combustor causes stagnation pressure loss. Shockwaves caused by fuel injection into supersonic flows are unavoidable. The use of oblique jet injection is a way to lessen the loss from the fuel jet injection. It is also unavoidable to induce shockwaves from geometric alterations of a combustor's surface (such as the introduction of a cavity) if a recirculation zone is required for flame holding. In this study, a recess in the surface (a cavity) is used rather than a protrusion or a bluff body (Jeong et al. (2006)), with a resulting cavity that has an inclined back wall in order to minimize the stagnation pressure loss. However, even with this inclined back wall, the cavity introduces a finite loss, and hence creates more loss, of course, than that of a flat surface. Chapter 4 describes a configuration that uses two fuel jets injected through a flat wall, in conjunction with discharge plasma-enhancement to ignite and stabilize jet flames in supersonic cross flows.

3.6.2. Localized Plasma Effect

Effects of a pulsed discharge plasma applied inside of a cavity are limited by the highly localized nature of the flame region within the cavity. The cavity flame is confined mostly in the cavity region due to a lack of radical supply from the cavity flame or an upper limit of J_n for producing an effective radical source in the cavity as discussed in Section 3.5.2. As a result, the plasma effects, which are combustion reaction enhancement and reduction of ignition delay time, are also localized in the cavity.

3.7. Summary

In this chapter, a cavity flame stabilization method assisted by a pulsed discharge plasma in supersonic flows is studied experimentally. Results of this chapter are summarized as follows:

- A cavity flame in the leeward side of a hydrogen jet is auto-ignited during the expansion tube test time (300 – 500 μ s) when an enthalpy of a freestream flow is higher than 2 MJ/kg.
- A filamentary flame in the windward side of a hydrogen jet is observed when the enthalpy of the freestream flow is higher than 3 MJ/kg.
- A pulsed discharge plasma inside the cavity enhances an auto-ignited cavity flame and reduces the ignition delay time of the jet flame.
- An ethylene jet flame inside a cavity is ignited by the pulsed plasma.
- The plasma assisted cavity flame stabilization method is identified to have some drawbacks - a stagnation pressure loss from the cavity induced shockwaves and a localized plasma effect in the vicinity of the cavity.

The observations reveal that an application of a pulsed discharge plasma in a cavity is effective in flame holding in a supersonic flow although the flame stabilization method utilizing a cavity has inherent deficiencies. An alternative method that is introduced in Chapter 4 employs a dual fuel jet configuration without the use of a cavity. Such a configuration overcomes these deficiencies introduced by cavities for flame stabilization. A flat wall without a cavity is expected to result in lesser stagnation pressure loss. Also, as described in the next chapter, an additional (non-

tilted) downstream fuel jet is used to enhance the propagation of the flame into the freestream flows.

Chapter 4 Plasma Assisted Flame Stabilization on a Flat Wall

In this chapter, experimental results using a jet in crossflow model of a flat wall without any geometric alterations of the surface (e.g., cavities) are presented.

4.1. Flat Wall Flame Stabilization

The flat and smooth wall surface of a supersonic combustor is ideal for minimizing the stagnation pressure loss of a supersonic flow that travels through the combustor. However, it is quite challenging to hold a flame in a supersonic flow without a region of reduced velocity or recirculation provided by geometric alterations such as a cavity. In Chapter 3, the effects of a cavity on the flame holding mechanism in a supersonic environment are discussed. It is seen that the slow flow of the cavity flame serves as a radical source shortening the ignition delay time (τ_{ign}) of the supersonic flow of flammable mixtures. Thus, to hold a flame on a flat wall, an effective radical source capable of surviving supersonic freestream flow conditions without the presence of a cavity is essential. The plasma discharge itself can serve as the radical source on the flat wall because it does not require the slow flow region to be sustained.

Plasma emission images in Fig. 4.1 (top view) taken by an intensified fast framing camera with a supersonic flow (run condition 1 in table 2.2: $h_0 \sim 1$ MJ/kg) reveal that the pulsed plasma survives the supersonic flow on the flat plate. The direction of the supersonic flow is from left to the right in all of the images presented in this chapter. The exposure time of the image is set to 40 μs to capture at least two plasma pulses (50 kHz repetition rate) in a single camera frame without spectral filtering. The time $t = 0$ μs is the beginning of the test time. Before the start of the test time (at - 300 μs), a diffuse discharge emission is observed while more intense streamers are produced between the 6 mm separated electrodes during the test time period (approximately 700 μs time duration). When the helium gas following the air test gas arrives at the test section, the discharge becomes dimmer and again more

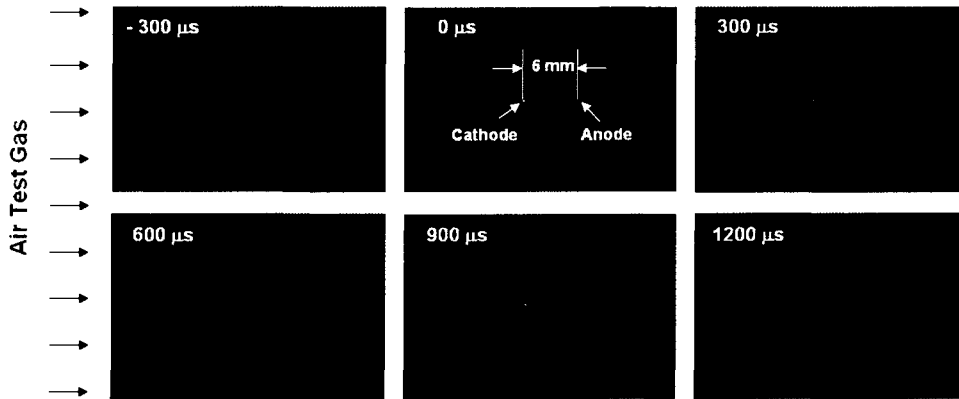


Figure 4.1 Plasma emission images (top view) taken by an intensified fast framing camera with a supersonic air flow (run condition 1: $Ma \sim 1.7$, $h_0 \sim 1.0$ MJ/kg, $T_{static} \sim 900$ K, $P_{static} \sim 25$ kPa and $U_\infty \sim 1000$ m/s): $0 \mu s$ is the beginning of the test time lasting approximately $700 \mu s$.

diffuse. This confirms that the pulsed plasma is sustained in the boundary layer region of the supersonic flow in the absence of the slow flow region such as a cavity. Further improvement of the role of the plasma as the radical source is achievable by providing a reactive gas mixture in the plasma region because the reactions of the gas mixture triggered by the plasma would produce extra radicals in addition to the plasma excited or dissociated species. Therefore, the pulsed plasma should be applied in the leeward side of a fuel jet where a well mixed flammable gas mixture exists.

With a few exceptions, oxygen is used as the test gas for runs described throughout this chapter for facilitating combustion reaction because it provides the most likely means of successfully achieving flame holding in these severe conditions for the case of a flat wall. For a comparison, some tests were carried out with air to study plasma-assisted combustion under more practical conditions. The comparison of these two different test gas cases will confirm that oxygen produces more pronounced effects even at the relatively low pulsed plasma average power employed (~ 10 W).

4.2. Single Fuel Jet Injection

The schematic presented in Fig. 4.2 qualitatively describes the flow field caused by a single transverse fuel jet injection in a supersonic flow including recirculation zones, barrel shock, Mach disk and the bow shock. A boundary layer forming at the sharp leading edge of the model thickens and separates from the surface due to interactions with the bow shock induced by the jet injection. The small recirculation zone (separation bubble) located at the boundary layer separation point can serve as a means of igniting the flow since this is where there is mixing of the hot boundary layer gas with the fuel, but only if the enthalpy of the freestream flow is high enough to initiate combustion reactions. Flame ignition initiating near this separated flow region was observed in previous studies (Heltsley et al. (2008)) when the supersonic flow enthalpy was greater than 2.5 MJ/kg. The red colored region in the leeward side of the jet, between two electrodes marked by black solid lines, serves to show where the plasma is applied to initiate combustion reactions under conditions where auto-ignition is not observed.

Figure 4.3 is an OH emission image depicting a small reaction region triggered by the pulsed plasma in a supersonic oxygen crossflow (run condition 1: $h_0 \sim 1$ MJ/kg). The spontaneous emission directly excited by the discharge plasma is not seen in the

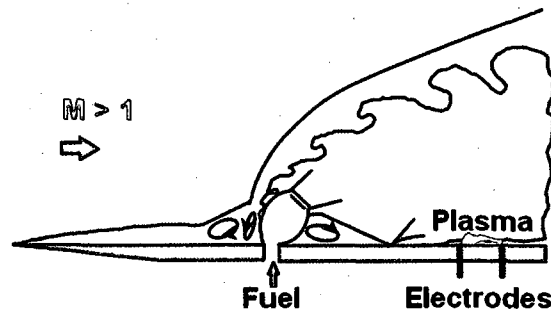


Figure 4.2 A schematic of a flow field caused by a single fuel jet injection.

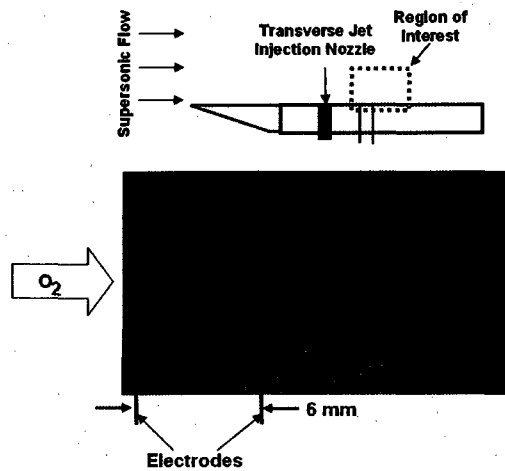


Figure 4.3 An OH emission image depicting a small reaction region triggered by the pulsed plasma in a supersonic oxygen crossflow (run condition 1: $Ma \sim 1.7$, $h_0 \sim 1.0$ MJ/kg, $T_{static} \sim 900$ K, $P_{static} \sim 25$ kPa and $U_\infty \sim 1000$ m/s) with $J \sim 0.1$.

image due to its relatively short lifetime, as this image is taken $1 \mu s$ after the plasma pulse. The OH emission seen in these conditions provides evidence that the pulsed plasma is capable of initiating reactions in the fuel/freestream flow mixture although this reactive region appears to stay close to the surface. The momentum ratio is $J \sim 0.1$ for the conditions corresponding to this figure, which places the jet flow in the subsonic jet regime. This ratio is found to maximize the OH emission intensity. Spontaneous OH emission is not observed at a time of $1 \mu s$ after the plasma pulse with ratios $J > 0.2$.

The fuel jet serves to provide a combustible mixture close to the wall in the vicinity of the discharge, where ignition can take place. This is similar to the crucial role played by the cavity flame stabilization, as discussed in Chapter 3, where fuel and air are entrained in the cavity and ignited by the discharge. The second important role played by the fuel jet injection is to penetrate and seed the freestream with fuel so that the plasma-ignited flame can propagate into the supersonic flow. However, with the low J 's (< 0.2) used, and in the absence of a cavity, it is difficult to enhance flame

propagation into the supersonic freestream flow, because the jet fuel resides only near the surface region. To overcome these limitations, which cannot be addressed with a single fuel jet injection configuration, a second additional fuel jet is introduced downstream of the discharge, is ignited by the plasma-activated upstream jet flame, and serves to promote flame propagation as described in the following section below. In essence, the dual fuel jet configuration enables to separately control of ignition and flame propagation.

4.3. Dual Fuel Jet Injection

Figure 4.4 shows a schematic of a dual fuel jet injection model implemented with an oblique upstream jet nozzle, a transverse downstream jet nozzle and two electrodes between the two nozzles. The dual jet configuration is designed to separate the two roles played by a single fuel jet with the addition of the second transverse fuel jet downstream of the electrodes. The upstream jet is used for the production of the radical source and the downstream jet is added for the enhancement of flame propagation. Based on the observations in the previous section, the enhancement of the radical source is expected by applying the pulsed plasma in the leeward side of the

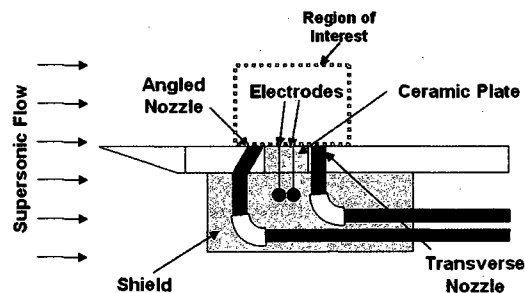


Figure 4.4 A schematic of dual fuel jet injection model implemented with an oblique upstream jet, a transverse downstream jet and two electrodes between the two jets.

upstream jet. A red dotted rectangle in Fig. 4.4 indicates the region of interest that is accessible by diagnostic components such as a laser sheet for exciting ground state OH, an intensified camera for OH PLIF and a fast framing camera for Schlieren imaging.

4.3.1. Subsonic Oblique Upstream Jet

As mentioned above, the role of the upstream jet is to provide an effective radical source when combined with the plasma discharge. The enhancement of flame propagation into a freestream flow is not considered as an issue for the upstream jet. Since momentum is not needed for penetration of the cross flow, the upstream jet is chosen to be subsonic and is directed such that it makes an oblique angle relative to the cross flow. In Section 4.2 above, we described how the reactions triggered by the plasma are maximized when the upstream jet is in the subsonic jet regime. The use of the oblique jet increases the fuel concentration at the plasma region in the leeward side of the jet. Furthermore, oblique jet injection lessens the stagnation pressure loss caused by the jet induced shockwave when compared to that of a transverse jet. Two different oblique jet injection angles are tested in this study. These are jet nozzles inclined by 30° and 60° from a horizontal plane towards the downstream direction.

4.3.2. Sonic Transverse Downstream Jet

The use of the downstream jet is to enhance flame propagation and extend localized plasma effects into the freestream flow. This downstream fuel jet is capable of producing radicals in concert with the upstream jet. Accordingly, the plasma assisted upstream jet flame serving as a radical source or a pilot flame is expected to be able to ignite and enhance the downstream jet flame.

The use of the transverse sonic jet serves another purpose. Undoubtedly, deep jet penetration is not achievable with a subsonic jet, and transverse injection guarantees the deepest jet penetration into a freestream flow for a fixed fuel flow rate. In addition, an extra recirculation zone, induced by the downstream jet injection,

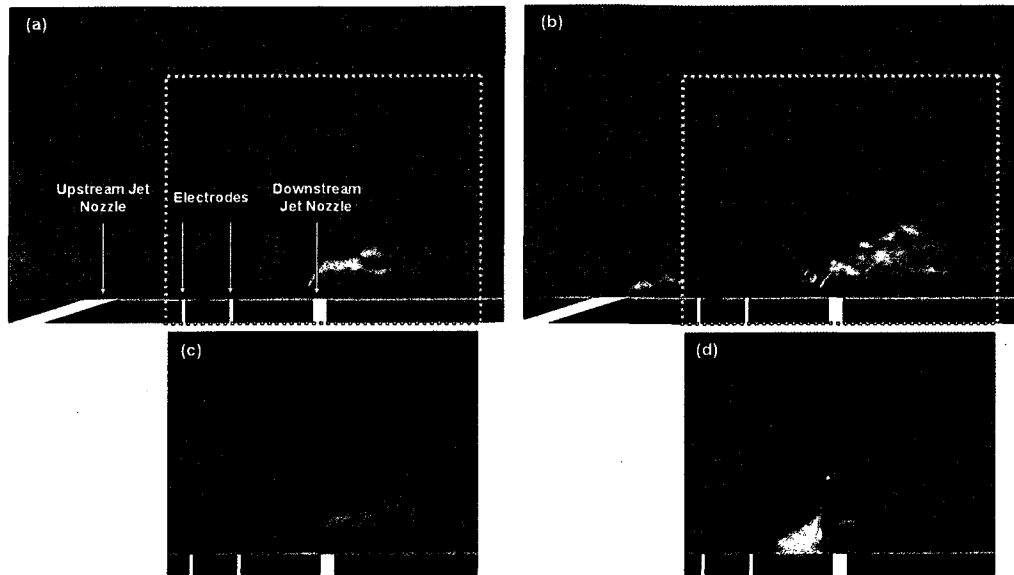


Figure 4.5 Two Schlieren images illustrate flow fields (run condition 2: $Ma \sim 2.0$, $h_0 \sim 2.0$ MJ/kg, $T_{static} \sim 1250$ K, $P_{static} \sim 16$ kPa and $U_\infty \sim 1380$ m/s): (a) only with the downstream jet ($J_n \sim 9.5 \pm 0.1$) injection and (b) with both of the upstream ($J_n \sim 3.5 \pm 0.1$)/downstream jets activated. Rectangular regions indicated by red dotted lines in the Schlieren images are overlapped on OH PLIF images (c) without and (d) with the upstream jet. The test gas is pure oxygen.

further enhances the plasma-assisted combustion process. The existence of the extra recirculation zone is beneficial for the production of an efficient radical source in front of the downstream jet.

Flame ignition/enhancement by the extra recirculation zone is observed in Fig. 4.5 (run condition 2: $h_0 \sim 2.0$ MJ/kg, pure oxygen crossflow) even in the absence of the plasma, when a 30° angled oblique upstream jet is injected. Two Schlieren images serve to illustrate flow fields first with only the downstream jet injected (Fig. 4.5 (a)) and then with both jets activated (Fig. 4.5 (b)). Rectangular regions indicated by red dotted lines in the Schlieren images (Figs 4.5 (a) and (b)) are superimposed onto the corresponding OH PLIF images (Figs 4.5 (c) and (d)). The jet momentum ratios of the

upstream and downstream jets are $J_n \sim 3.5$ and $J_n \sim 9.5$, respectively. As shown in Fig. 4.5 (b), the intersection of the jet trajectories is located in the region adjacent to the second recirculation zone. The relatively strong flame observed at the recirculation zone in Fig. 4.5 (d) enhances the combustion of the downstream jet fuel and is clearly stronger when compared to the weak fragmented flame in Fig. 4.5 (c), i.e., when there is no upstream jet. For the cases illustrated in here, the upstream fuel jet is injected into the boundary layer region having high static temperature and slow flow speed. Then, the fuel containing mixture in the boundary layer is compressed by the bow shock induced by the downstream jet and becomes part of the recirculation zone. Ultimately, the high temperature flammable mixture is ignited while residing in this region.

Ignition in the region without a plasma is not seen when the upstream jet is injected at 60° angle as shown in Fig. 4.6 (OH PLIF images overlapped onto Schlieren images taken with pure oxygen crossflow (run condition 4: $h_0 \sim 2.4$ MJ/kg): Figs 4.6 (a) without the upstream jet, and (b) with both jets active) because the fuel is not put into the high temperature boundary layer region effectively. In this case, a subsonic upstream oblique jet ($J_n \sim 0.1$) and a sonic downstream transverse jet ($J_n \sim 2$) are injected which are illustrated in a Schlieren image presented in Fig. 4.6 (c). The two jets are injected into 200 torr static ambient air in the test section. A Mach disk indicating a sonic jet is observed in the downstream jet while no clear compression shock such as Mach disk is observed in the oblique upstream jet. The use of the subsonic upstream jet is required to provide the reaction region triggered by the plasma discharge as shown in Section 4.2 with the J lower than 0.2. It is noteworthy that the subsonic upstream jet even eliminates the weak OH signal in the adjacent to the recirculation region appearing without the upstream jet as shown in Fig. 4.6 (a), because the upstream jet induced shockwave weakens the shock in the downstream. Nevertheless, the plasma can enhance the role of the boundary layer in this case.

4.3.3. Plasma Application between the Two Jets

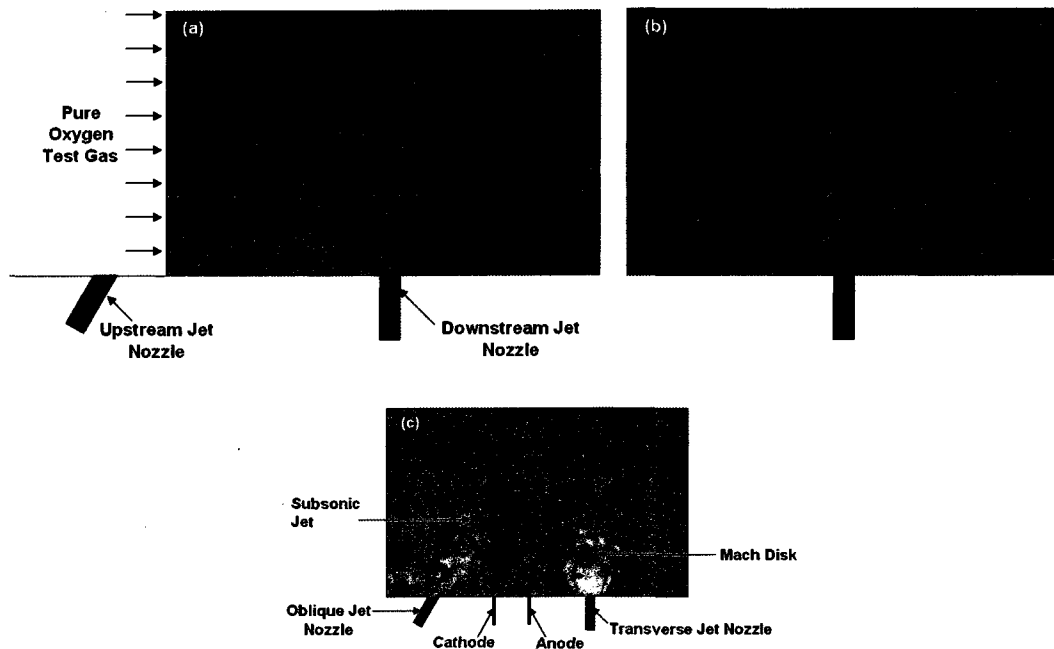


Figure 4.6 Two OH PLIF images overlapped on Schlieren images taken with pure oxygen crossflow (run condition 4: $Ma \sim 2.4$, $h_0 \sim 2.4$ MJ/kg, $T_{static} \sim 1300$ K, $P_{static} \sim 24$ kPa and $U_\infty \sim 1690$ m/s): (a) without the upstream jet ($J_n \sim 0.1$ and 60° angle) and (b) with the both jets activated, and (c) a Schlieren image confirming the application of the upstream subsonic oblique jet and the downstream sonic transverse jet ($J_n \sim 2 \pm 0.1$) (the jets are injected into 200 torr static ambient air in the test section).

Figure 4.7 depicts representative OH emission images in a supersonic oxygen crossflow (run condition 1: $h_0 \sim 1.0$ MJ/kg) taken $1 \mu s$ after a plasma pulse. A time-averaged photograph of the discharge indicates that it is observed to be a streamer of approximately 1 mm in diameter (spanning 6 mm between the electrodes) extending up to 2 mm above the surface. The boundary layer thickness is estimated to be on the order of 0.1 mm at the location of the discharge (we are assuming a laminar boundary layer with $Re_x < 200,000$ (Goldfeld and Orlik (2005)), where x is the distance between

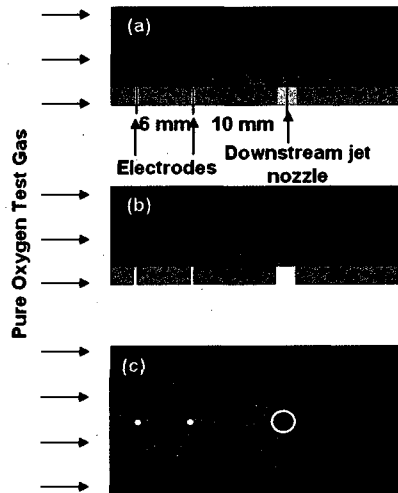


Figure 4.7 OH emission images in a supersonic oxygen crossflow (run condition 1: $Ma \sim 1.7$, $h_0 \sim 1.0$ MJ/kg, $T_{\text{static}} \sim 900$ K, $P_{\text{static}} \sim 25$ kPa and $U_{\infty} \sim 1000$ m/s) taken $1 \mu\text{s}$ after a plasma pulse: (a) side view with only the upstream jet ($J_n \sim 0.1$), and (b) side view and (c) top view with both of the upstream/downstream ($J_n \sim 2 \pm 0.1$) jets injected.

the leading edge of the model and the upstream electrode (cathode)). Figure 4.7 (a) is taken with only the upstream hydrogen jet injection (60° angle from a horizontal plane toward downstream). The momentum ratio of the upstream jet is approximately $J_n \sim 0.1$. In contrast, Figs. 4.7 (b) and (c) are corresponding images of OH emission (side and top views, respectively), when both the upstream and downstream hydrogen jets activated. The momentum ratio of the downstream jet is $J_n \sim 2$. In both cases (Fig. 4.7 (a) and (b)), the excited OH emission appears to be strongest very near the wall surface downstream of the electrode pair. The radicals do not penetrate deeper into the crossflow because the upstream hydrogen jet momentum ratio is too low. It is noteworthy that no OH emission is detected without the plasma. Therefore, this emission originates from excited OH that is produced as a result of plasma excitation and convected by the flow, since the excited $A^2\Sigma^+$ state has a relatively long lifetime. We cannot rule out the possibility of the production of an initial flame kernel,

however, ground state OH is not detected far from the surface by PLIF imaging under these conditions, confirming that a flame has not propagated into the free stream.

Consequently, the OH radicals seen in the emission images are produced by the pulsed plasma from the oxygen crossflow mixed primarily with hydrogen supplied through the upstream jet nozzle. In Fig. 4.7 (a), we see that in the absence of a downstream jet, the radicals spread over a wide range far downstream of the electrodes, while a stronger and narrower OH emission region is observed between the electrode pair and the downstream jet nozzle (Fig. 4.7 (b)) with both of the jets activated. Figure 4.7 (c) confirms that the downstream jet blocks the crossflow and provides a small recirculation region in front of the bow shock induced by the jet.

4.3.4. Plasma Ignited Upstream Jet Flame

The effect of the pulsed plasma on the upstream jet flame is illustrated in detail with a higher enthalpy supersonic crossflow by the OH PLIF images in Fig. 4.8. The upstream jet injection angle is 60° from a horizontal plane ($J_n \sim 0.1$) with pure oxygen

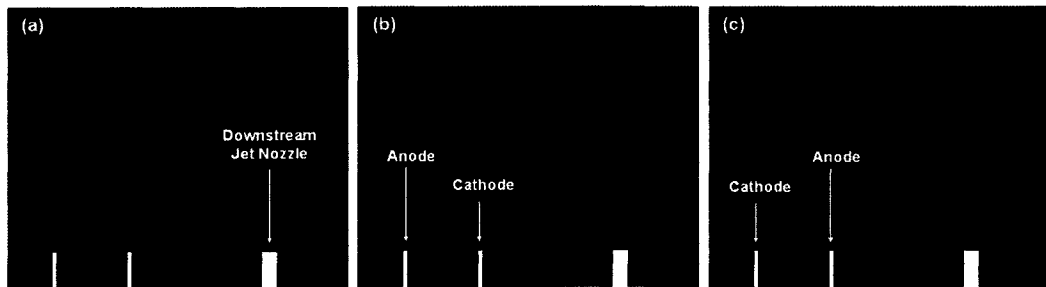


Figure 4.8 OH PLIF images in front of the downstream jet of $J_n \sim 3 \pm 0.1$ taken (a) without the plasma and $1 \mu\text{s}$ after a discharge pulse: (b) anode upstream and (c) cathode upstream. A typical Schlieren image taken under the same flow condition (run condition 3: $Ma \sim 2.4$, $h_0 \sim 2.4 \text{ MJ/kg}$, $T_{\text{static}} \sim 1240 \text{ K}$, $P_{\text{static}} \sim 18 \text{ kPa}$ and $U_\infty \sim 1650 \text{ m/s}$) is overlapped on the PLIF images. The upstream jet injection angle is 60° from a horizontal plane and $J_n \sim 0.1$.

crossflow (run condition 3: $h_0 \sim 2.4$ MJ/kg). The OH images showing the small region near the electrodes and the downstream jet of $J_n \sim 3$ are taken without the plasma (Fig. 4.8 (a)) and 1 μ s after the discharge pulse (Figs 4.8 (b): anode upstream and (c): cathode upstream). The OH PLIF images are superimposed onto a Schlieren image taken under the same flow condition. Weak OH signal is detected near the surface in a high temperature boundary layer region (Fig. 4.8 (a)) while a strong flame is observed in Fig. 4.8 (c). The results reveal that the pulsed plasma is capable of enhancing the weak combustion reaction to be a more effective radical source in front of the downstream jet. In addition, the comparison of Figs 4.8 (b) and (c) shows that the cathode in the upstream is better than the downstream cathode for reaction enhancement under the current flow condition.

4.3.5. Ignition of Downstream Jet Flame

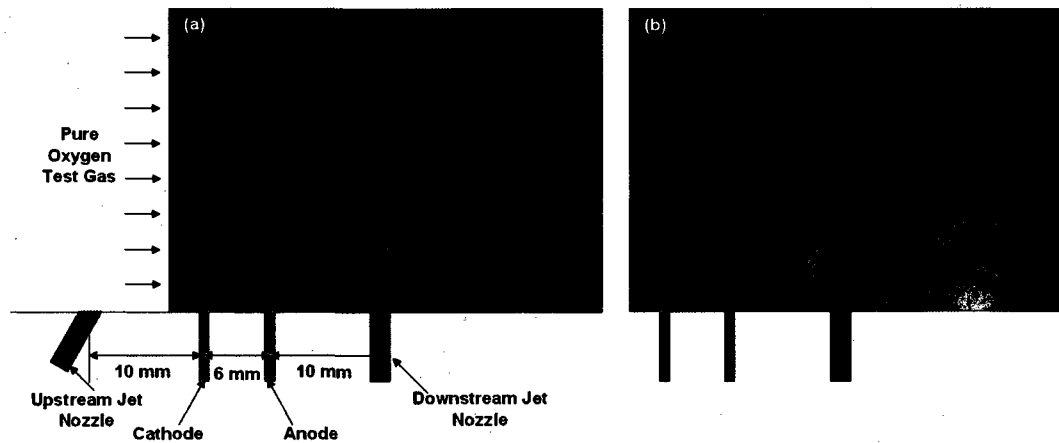


Figure 4.9 OH PLIF images taken (a) in the absence of a plasma, and (b) 1 μ s after a plasma pulse under a high enthalpy flow condition (run condition 4: $Ma \sim 2.4$, $h_0 \sim 2.4$ MJ/kg, $T_{static} \sim 1300$ K, $P_{static} \sim 24$ kPa and $U_\infty \sim 1690$ m/s). The upstream and downstream hydrogen jets are activated with corresponding jet momentum ratios $J_n \sim 0.1$ and $J_n \sim 2 \pm 0.1$.

Figure 4.9 presents typical OH PLIF images of ground state OH radicals taken in the absence of a plasma (Fig. 4.9 (a)), and 1 μ s after a plasma pulse (Fig. 4.9 (b)) under high enthalpy supersonic crossflow conditions (run condition 4: $h_0 \sim 2.4$ MJ/kg). In each case, both the upstream and downstream hydrogen jets are activated, with corresponding jet momentum ratios $J_n \sim 0.1$ and $J_n \sim 2$, respectively. We estimate that the ratio of energy deposition by the plasma to the total crossflow enthalpy is on the order of 10^{-6} . The flow enthalpy is estimated considering the flow processed through the test section during one plasma pulse period (20 μ s with 50 kHz repetition rate, 50 J/period) and the pulse energy of 0.2 mJ (10 W power and 50 kHz). We see that a small, fragmented OH region is apparent on the windward side of the downstream jet, in Fig. 4.9 (a), suggesting the presence of a weak, auto-ignited downstream jet flame. In contrast, in the presence of the plasma, there is a more intense OH region distributed over a wider area in both the windward and leeward side of the downstream jet, confirming the existence of a stronger jet flame that appears to propagate into the supersonic crossflow. Clearly, the ignition and stabilization of this flame is only achieved by the use of the plasma under these flow conditions. Recall from the emission images shown in Fig. 4.7, that the presence of the downstream jet served to produce a region rich in plasma activated species just upstream of, and around, this fuel jet. As shown in the PLIF images in Fig 4.9 (b), combustion is clearly taking place in this region and the flame extends well into the freestream, suggesting that this region in front of the bow shock, may serve to pilot the resulting jet flame.

Based on the lower heating value (LHV ~ 120 MJ/kg) of the hydrogen fuel, we estimate that only one part in 10^5 of the fuel's energy release is used by the plasma to ignite the flame (assuming that the fuel is completely consumed: the combustion energy of the hydrogen fuel injected during a pulse period ~ 5.4 J and the energy of a plasma pulse is 0.2 mJ). The fraction of the discharge deposited energy that is used in dissociation and production of radicals depends on the characteristics of the discharge. The reduced electric field of the plasma is approximately 300 Td, resulting in an electron temperature (in an equimolar H_2/O_2 mixture) of 8 eV, as estimated from the electron energy distribution function (EEDF) derived from the solution of the

Boltzmann equation using the commercially-available Boltzmann solver BOLSIG (Boeuf et al. (1996)). The method of Penetrante et al. (1996) with available dissociation cross sections and the EEDF provides initial yields of dissociated species. If these species are produced within the discharge volume of approximately 6 mm^3 during the duration of the discharge pulse by electron impact dissociation, the dissociation rate coefficients and resulting radical concentrations permit an estimate of the electron number density during the discharge pulse, which we calculate to be approximately 10^{18} m^{-3} . A more detailed description of these and related simulations is presented in Chapter 5.

The nature of the post-discharge flow field and its interaction with the associated shock is believed to play an important role in the flame ignition mechanism. A superposition of typical pulsed Schlieren images with the OH PLIF images of Fig. 4.9, assists in trying to understand this relationship by revealing interesting flow features. These superimposed images are presented in Fig. 4.10. Figure 4.10 (a), combines a typical Schlieren image with the PLIF image (discharge off) of Fig. 4.9 (a), while Fig. 4.10 (b), combines the same Schlieren image with the PLIF image (discharge on) of Fig. 4.9 (b).

As illustrated in Fig. 4.10 (a), there is evidence of an auto-ignited flame just behind the bow shock where we expect the pressure and temperature to be elevated by the shockwave. Note however, that there is no detectable OH in the leeward side of the jet where the fuel and crossflow are expected to be well mixed in the jet wake (Kawai and Lele (2007)). It seems that despite this auto-ignition behind the bow shock, the flame is marginally stable, and does not propagate into the freestream to consume a significant fraction of the jet fuel. This is contrasted with the case in the presence of the discharge, illustrated in Fig. 4.10 (b). In the presence of the plasma, we see that the flame is auto-ignited behind the bow shock, but it is attached to the strong combustion region in front of the bow shock, and we also find that there is evidence of even stronger OH signals in the leeward side of the jet in comparison to the windward side, signifying the presence of combustion in the jet wake. The results of the discharge-off case indicate that the auto-ignition is triggered by the shockwave, and it is very likely

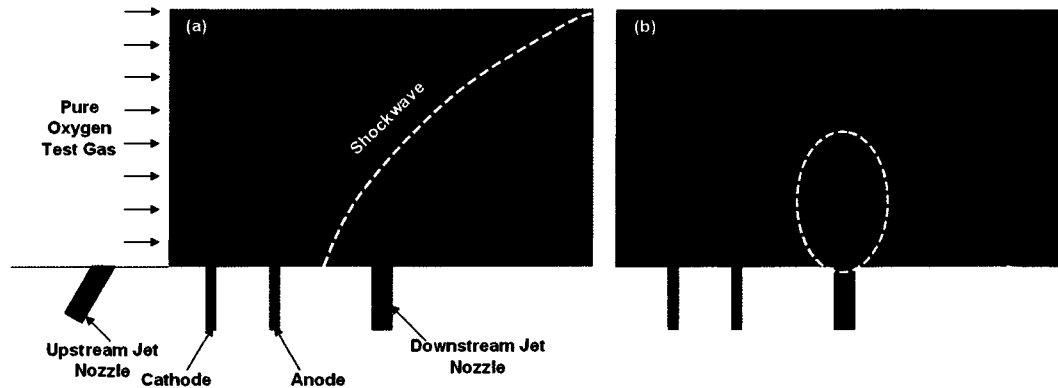


Figure 4.10 OH PLIF images (Fig. 4.9) overlapped with a typical Schlieren image of the same flow condition (run condition 4: $Ma \sim 2.4$, $h_0 \sim 2.4$ MJ/kg, $T_{static} \sim 1300$ K, $P_{static} \sim 24$ kPa and $U_\infty \sim 1690$ m/s): (a) without the plasma and (b) in the presence of the plasma. The upstream and downstream hydrogen jets are activated with corresponding jet momentum ratios $J_n \sim 0.1$ and $J_n \sim 2 \pm 0.1$.

that even with the discharge plasma activation, the strength of the shock may be an important parameter in determining auto-ignition conditions. As mentioned above, the shockwave raises the temperature and pressure, notably in the region adjacent to the boundary of hydrogen and oxygen in the windward side. Interestingly, the plasma triggered pilot in the recirculation region in front of the bow shock appears to penetrate across the shockwave into this marginally auto-ignitable mixture, and seems to be directly connected to the post-shock jet flame (region highlighted by the white circle in Fig. 4.10 (b)). It is also possible that the strong combustion occurring in the leeward side of the jet is also partially dependent on the production of this plasma-activated pilot flame, since the species in this upstream region can flow around the bow shock (Fig. 4.7 (c)), and also can traverse the shock and flow around the jet to penetrate into the hydrogen/oxygen mixture in the leeward side.

4.3.6. Sustainability of Plasma Assisted Flame

A set of time sequential OH PLIF images in Fig. 4.11 reveals the capability of the pulsed plasma to sustain the plasma assisted jet flame during the whole test time even between the plasma pulses. Both of the upstream (60° angle, $J_n \sim 0.1$) and downstream jets ($J_n \sim 3$) are injected into the high enthalpy oxygen freestream flow (run condition 3: $h_0 \sim 2.4$ MJ/kg). Figure 4.11 (a) shows filamentary auto-ignited downstream jet flame in the absence of the plasma, taken $200 \mu\text{s}$ after beginning of the test time, while, in Figs 4.11 (b), (c) and (d) taken $1 \mu\text{s}$ after the discharge pulse (at the

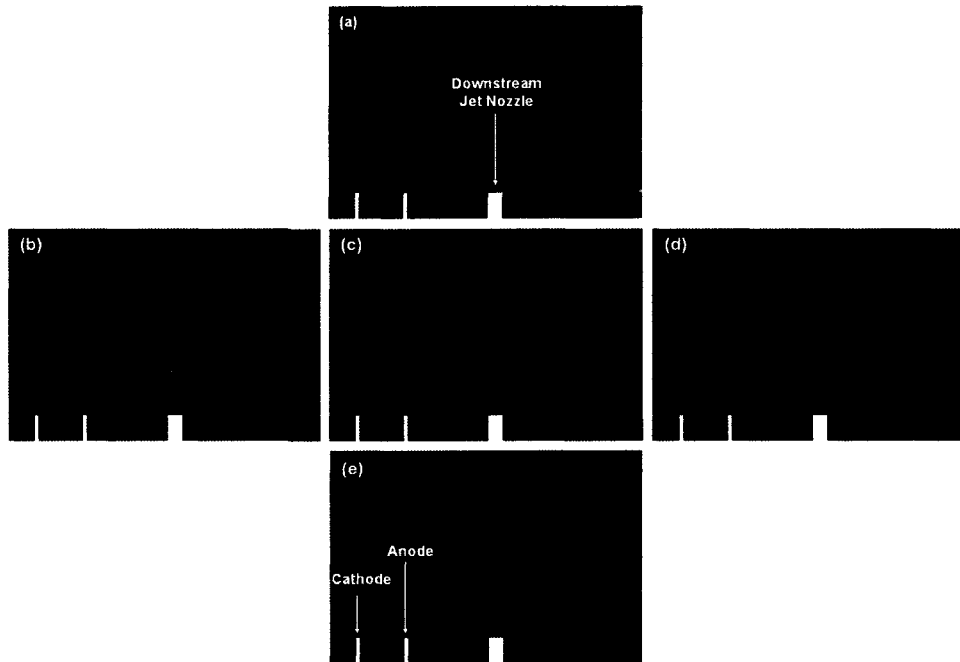


Figure 4.11 OH PLIF images overlapped with a Schlieren image (a) in the absence of the plasma taken $200 \mu\text{s}$ after the beginning of the test time, and (b), (c) and (d) are taken $1 \mu\text{s}$ after a plasma pulse: (b) at the beginning of the test time, $0 \mu\text{s}$, (c) $100 \mu\text{s}$ and (d) $200 \mu\text{s}$ after the beginning. (e) is taken $18 \mu\text{s}$ after the plasma pulse. Pure oxygen crossflow is used (run condition 3: $Ma \sim 2.4$, $h_0 \sim 2.4$ MJ/kg, $T_{\text{static}} \sim 1240$ K, $P_{\text{static}} \sim 18$ kPa and $U_\infty \sim 1650$ m/s). The upstream and downstream hydrogen jets are activated with corresponding jet momentum ratios $J_n \sim 0.1$ and $J_n \sim 3 \pm 0.1$.

beginning of the test time, 0 μs (Fig. 4.11 (b)), and 100 μs (Fig. 4.11 (c)) and 200 μs (Fig. 4.11 (d)) after the beginning), plasma enhanced pilot flames and stronger downstream jet flames in the leeward side as well as in the windward side of the jet are observed. It is evident that the plasma assisted flame is sustained during the whole test time that is approximately 350 μs in the flow condition. Also, it is noteworthy that the plasma enhanced flame appears at the start of the test time (at 0 μs in Fig. 4.11 (b)) while a cavity flame is ignited 40 μs after the beginning of the test time even in higher enthalpy freestream flow condition. This may be due to different gas mixing and convection speed. As mentioned in Section 3.3.2, remnant helium gas trapped in the cavity would dilute the entrained fuel/oxidizer mixture for a while to delay the ignition. Also, the convection speed carrying radicals produced by the plasma and the flame is faster in the case of the flat wall when compared to the speed in the presence of the cavity. Consequently, the effect of the plasma can be disseminated faster than the cavity case. Another notable observation in the OH PLIF images in Figs 4.11 (b), (c) and (d) is that the flame on the leeward side of the downstream jet gets stronger as time progresses.

Figure 4.11 (e) is taken 18 μs after the plasma pulse to further confirm the flame sustaining capability of the pulsed plasma between the plasma pulses. As shown in the OH PLIF image, the flame in the windward side of the downstream jet is stronger than the auto-ignited flame in Fig. 4.11 (a), which implies that a 20 μs pulse period (50 kHz plasma repetition rate) is short enough to sustain the plasma assisted flame between the pulses. It is noteworthy that only one plasma pulse is responsible for the plasma assisted flame observed in the instantaneous OH PLIF image because the flow residence time in the region of interest of the image is fairly short for the flow to be affected by multiple pulses. The freestream flow travels 2 – 3 cm during a pulse period (20 μs) which is longer than the distance between the cathode and the downstream jet nozzle (1.6 cm).

4.3.7. Ethylene Jet Flame Ignition

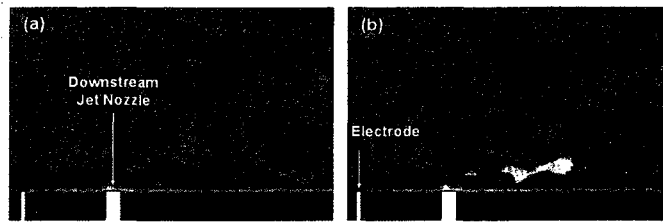


Figure 4.12 OH PLIF images taken (a) without and (b) in the presence of the pulsed plasma. Both of the upstream and downstream ($J_n \sim 2$) ethylene jets are injected into the oxygen crossflow (run condition 3: $Ma \sim 2.4$, $h_0 \sim 2.4$ MJ/kg, $T_{static} \sim 1240$ K, $P_{static} \sim 18$ kPa and $U_\infty \sim 1650$ m/s). J_n of the 30° angled upstream jet is approximately 0.1.

Figure 4.12 presents OH PLIF images taken (a) without and (b) in the presence of the pulsed plasma with ethylene fuel jet injection. Both of the upstream (30° angled from a horizontal plane towards the downstream, $J_n \sim 0.1$) and downstream ($J_n \sim 2$) ethylene jets are injected into the oxygen crossflow of run condition 3. The maximum J achievable with the current fuel delivery system is approximately 2 because the pressure drop when using ethylene gas through the fuel delivery system is greater than that of hydrogen. No detectable OH was observed with higher enthalpy flows ($h_0 > 3.5$ MJ/kg) and ethylene jets of higher J 's as reported previously (Heltsley et al. (2008)). As shown in Fig. 4.12 (a), the flame is not ignited without the plasma while a downstream jet flame is ignited in the presence of the plasma (Fig. 4.12 (b)).

As discussed in Section 4.3.2, the lower injection angle (30° angle in this case) or lower J of the upstream jet enhances fuel entrainment into the hot boundary layer region on the surface. Ethylene, having longer ignition delay time than hydrogen, supplied by the upstream jet may be assisted in ignition by the high temperature gas in the boundary layer as well as the pulsed plasma.

4.4. Summary

The method introduced in this chapter utilizing no geometric alteration on the flat wall was successful in holding hydrogen and ethylene flames assisted by pulsed plasmas in supersonic oxygen crossflow. The experimental results with the jet in crossflow model of the flat wall are summarized as follows:

- A method of dual fuel jet injection on a flat wall was proposed, serving to separate the two roles of a single fuel jet. These roles are the production of the radical source and the enhancement of flame propagation into the supersonic freestream.
- The pulsed plasma was applied in the leeward side of the upstream jet to ignite/enhance a pilot flame that then serves as a radical source for downstream jet flame ignition.
- The plasma assisted pilot flame was effective in enhancing/sustaining the downstream jet flames in the windward/leeward side of the jet during the whole test time even between the plasma pulses when the repetition rate of the plasma pulse is 50 kHz.
- Ethylene jet flames were also ignited by this method under conditions where auto-ignition was not previously seen.

The experimental results presented in this chapter revealed the capability of the dual jet injection configuration on the flat wall assisted by a pulsed plasma, igniting and sustaining jet flames with minimized stagnation pressure loss. These results suggest the possible application of the method to more severe combustor conditions such as lower enthalpy and ambient air flows when the plasma operating condition is further optimized. The use of various plasma operating conditions can be estimated utilizing a numerical method presented in the next chapter. In Chapter 5, the plasma assisted flame stabilization mechanism will be investigated numerically and the effect

of plasma operating conditions including the frequency and the power of the plasma discharge on flame stability will be discussed.

Chapter 5 Modeling and Simulation

In this chapter, the results of a numerical modeling study of the pulsed plasma discharge and the reaction kinetics calculation of plasma assisted combustion are presented. The modeling and the simulations are targeted at the estimation of the prospective use of a high power pulsed plasma, and the validation of the plasma assisted flame stabilization mechanism depicted in the experimental results.

The diagram in Fig. 5.1 summarizes the general procedure of the simulation used here. The procedure starts with the modeling of the pulsed plasma. The pulsed plasma is a highly nonequilibrium plasma, requiring the solution of the Boltzmann equation. The electron energy distribution derived from the Boltzmann equation provides the rate coefficients of the electron impact dissociation reactions utilizing dissociation cross sections obtained from the literature (Corrigan (1961) and Vroom et al. (1969)). The rate coefficients, in accordance with the simplified initial yield calculation method proposed by Penetrante et al. (1996), allow us to calculate the concentrations of the species dissociated by the pulsed plasma (e.g. O and H from the parent species, H_2 and O_2). Then, the dissociated species are seeded into a flammable H_2/O_2 mixture under the flow or the static conditions of interest. The reaction kinetics calculation of the dissociated species and the flammable mixture is facilitated by the use of a MATLAB based code implemented with the Cantera toolbox developed by D. Goodwin (available at <http://www.cantera.org>). The Cantera program used in this

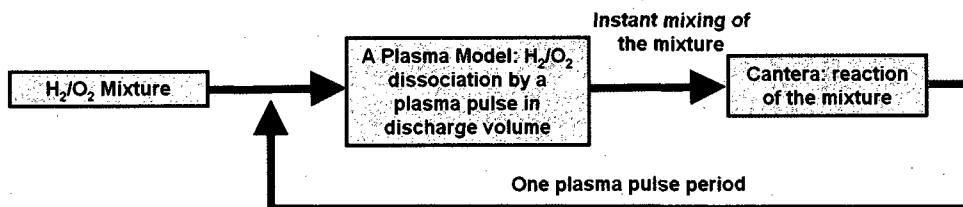


Figure 5.1 The schematic of the simulation procedure.

study is an open source software package, compatible with MATLAB, Python, C++ or Fortran, developed to solve problems involving chemical kinetics and chemical thermodynamics. In addition, for the validation of the experimental results presented in Chapter 4, a set of flow conditions and simplifying assumptions are included in the code.

The detailed assumptions and procedures used in the simulation will be presented in the following sections.

5.1. Modeling of the Pulsed Plasma

Figure 5.2 presents time averaged plasma emission images taken with increasing pressure in ambient air inside the test section without any spectral filtering. The distance between the two electrodes is 3 mm and the diameter of the electrodes (2 % thoriated tungsten rods) is 1 mm. A Cannon EOS 400D camera with 50 ms exposure time is used to acquire these photographs. The diffuse plasma seen under low pressure conditions (30 torr and 100 torr in Fig. 5.2) transitions to the intense streamer that appears to arc over the surface of the model as the pressure increases. The spontaneous emission of the plasma region originates from the excited species produced by the pulsed discharge (50 kHz repetition rate, 10 ns pulse width, 15 kV peak voltage and 15 A peak current). The pulsed plasma is capable of producing excited, ionized and dissociated species from a medium of neutral/ground state molecules. These radical species are more reactive than the neutral/ground state molecules although the translational/rotational temperature of the species may not be strongly elevated by the plasma. In a previous study utilizing the same plasma under at



Figure 5.2 Plasma emission pictures under varying air pressure conditions.

atmospheric pressure and room temperature condition, the vibrational temperature of the nitrogen molecule is found to be approximately 4000 K while its rotational temperature is less than 400 K (Kim et al. (2006)), suggesting that the pulsed plasma is a highly nonequilibrium plasma.

5.1.1. Assumptions

The key simplifying assumption made in this chapter is the omission of the excited and the ionized species while retaining the dissociated species. As discussed in the previous chapters, the pulsed plasma is considered to serve a primary function as a radical source to initiate combustion reactions.

The parameters determining the characteristics of the plasma are based on experimental discharge conditions. As briefly discussed in Section 4.3.5, the reduced electric field (E/N , where, E is the electric field applied between the electrode pair and N is the number density of the neutral molecules in the plasma region) of the pulsed plasma is estimated to be approximately 300 Td ($1 \text{ Td} = 10^{-17} \text{ V}\cdot\text{cm}^2$), based on the discharge conditions of 15 kV, 30 kPa, 300 K and 6 mm electrode separation. The reduced electric field is one of the key parameters controlling the electron energy distribution function (EEDF), which can be determined from a solution of the Boltzmann equation. The nominal plasma power consumed in the plasma region between the electrodes is taken to be 10 W, and is estimated from the typical experimental discharge voltage and current traces.

For further simplification, we neglect the secondary electron impact reactions with product gas species and radicals formed during the discharge (e.g., H_2O , OH and H_2O_2). This assumption can be justified for two reasons. First, the plasma pulse width is much less than the time needed to form these species, and second, especially under such high speed flow conditions, because the species produced by any one discharge pulse (including those formed from the primary products of hydrogen and oxygen dissociation) are likely to be swept away from the plasma region by convection during the time between pulses (the pulse period). Even in a static condition, the results of the

simulation (to be presented in the Section 5.3.2) reveal that, in most cases analyzed in the current study, only a few plasma pulses are responsible for ignition. During the time of a few pulse periods (20 μ s with 50 kHz frequency), the initial gas composition remains almost unchanged. It is noteworthy that the mole fraction of the radicals produced by one plasma pulse is on the order of 10^{-6} at a power of 10 W, which does not make a notable change in the mixture composition. Once the mixture is ignited, then the radical production of the pulsed plasma is negligible due to the exponentially increasing radical concentrations from the branching/propagation reactions of the combustion reaction mechanism.

5.1.2. Electron Energy Distribution Function

The EEDF is derived from the solution of the Boltzmann equation using the commercially-available Boltzmann solver BOLSIG (Boeuf et al. (1996)). The EEDF provides a probability distribution of electron number density as a function of electron energy. A typical EEDF, with various reduced electric fields and a representative gas concentration (equimolar H_2/O_2), calculated by BOLSIG is presented in Fig. 5.3. The

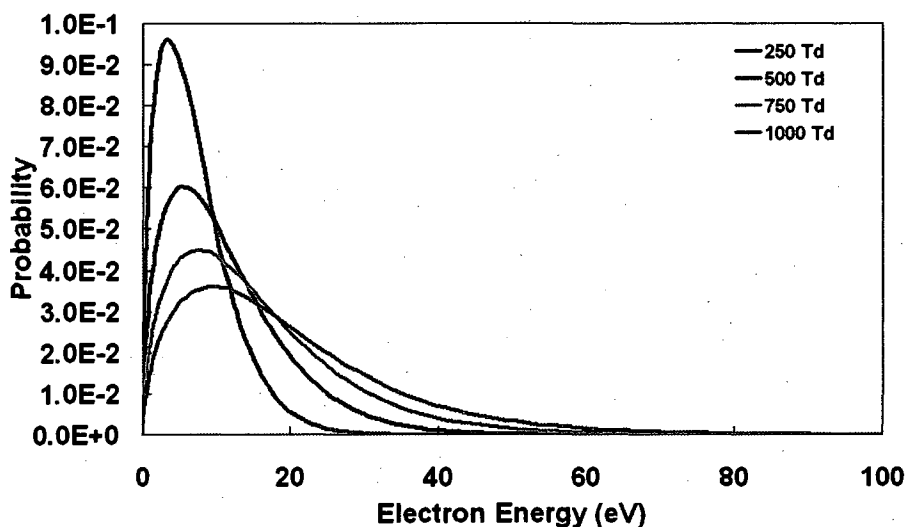
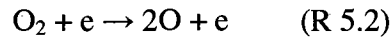
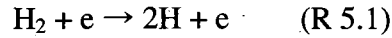


Figure 5.3 Typical electron energy distribution functions calculated by BOLSIG.

portion of the high energy electrons in the electron pool of the plasma gets larger with the increase of the reduced electric field. The EEDF determines the product species composition of the reactions involving electron impacts, such as ionization, excitation and dissociation, although only the dissociated species are considered in this study.

The EEDF is a function of the initial gas composition as well as the reduced electric field. Therefore, the database of the EEDF as a function of the gas composition is built for the calculations under various initial conditions. The EEDF, combined with the cross section data of the electron impact dissociation reactions, is used to calculate the dissociation reaction rate coefficients; only the H₂ and O₂ dissociation reactions (R 5.1 and R 5.2) by electron impact are considered in the current study.



5.1.3. Initial Yield of Dissociated Species

The initial yield of the radicals dissociated by the pulsed plasma is estimated by the method proposed by Penetrante et al. (1996). The method requires the parameters obtained from the BOLSIG code (electron drift velocity (V_d) and EEDF (f_e)) and the cross section data ($\sigma_{hydrogen}$ and σ_{oxygen}) of the electron impact dissociation reactions (R 5.1 and R 5.2). The rate coefficient of the dissociation reactions ($k_{hydrogen}$ and k_{oxygen}) can be derived from the following equation:

$$k = \int_0^{\infty} \sqrt{\frac{2\varepsilon}{m_e}} \sigma(\varepsilon) f_e(\varepsilon) d\varepsilon \quad (\text{Eq. 5.1})$$

Where ε is the electron energy and m_e is the electron mass. The method is proposed to calculate the number of dissociation reactions caused by the plasma as a function of

the energy consumption. The number of dissociation reactions in a plasma of 100 eV energy consumption (G) is calculated as follows:

$$G = 100 \frac{k}{V_d \frac{E}{N}} \quad (\text{Eq. 5.2})$$

Where E/N is the reduced electric field. The pulsed plasma of 10 W power (2×10^{-4} J per pulse) is used in this study and 100 eV is equivalent to 1.602×10^{-17} J. Therefore, $1.248 \times 10^{13} \times G$ is the number of the dissociation reactions caused by one plasma pulse. If the medium is a mixture (e.g. H_2/O_2 mixture), then the mole fractions of the parent species (C_{hydrogen} and C_{oxygen}) need to be incorporated to calculate the number of the specific dissociation reactions; the number can be easily converted to the number of dissociated radicals. For example, the number of hydrogen atoms produced by the plasma pulse (N_H) is calculated as follows:

$$N_H = 2 \times 1.248 \times 10^{13} \times C_{\text{hydrogen}} \times G_{\text{hydrogen}} \quad (\text{Eq. 5.3})$$

Where G_{hydrogen} is derived from k_{hydrogen} and the number is doubled because each reaction produces two H atoms.

5.2. Reaction Kinetics Calculation

The reactions following or preceding the radical production of the pulsed plasma are simulated using a MATLAB code utilizing the Cantera toolbox. The chemistry set of the species and the reactions employed in the calculation is obtained from h2air_highT.xml file available on the Cantera web site (<http://www.cantera.org>).

Each calculation step is separated by 20 ns. A Cantera function, netProdRate, calculates the rate of production of each product species at each time step. The rates of the productions, assumed to be constant during the 20 ns time duration between the

time steps, are used to calculate the gas composition at the next time step. The calculations are conducted under constant enthalpy conditions except the time steps when the dissociated radicals produced by the plasma are seeded. To comply with the constant enthalpy assumption, the temperature of the next time step is selected, while holding constant, the enthalpy of the mixture.

5.3. Perfectly Stirred Reactor with Pulsed Plasma

A perfectly stirred reactor (PSR) with instant mixing is utilized to simulate the reaction mechanism driven by the pulsed plasma. The pulsed plasma in the simulation procedure is treated a simple radical source providing dissociated radicals (e.g. O and H) into the mixture. In the case of the PSR simulation, the mixture in the reactor is affected by multiple plasma pulses as in the cavity experiment (Chapter 3) because the simulation is subjected to the slow flow speed conditions (e.g., in a cavity) which have much longer flow residence time in the reactor than a pulse period (20 μ s with 50 kHz repetition rate).

5.3.1. Assumptions and Simulation Procedure

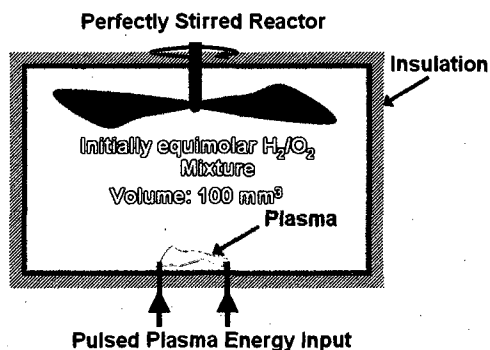


Figure 5.4 The schematic of the concept of the perfect stirred reactor (PSR).

Figure 5.4 describes the concept of the PSR (100 mm³ nominal volume: the volume of the cavity affected by the plasma - approximately 50 mm² cavity area and 2 mm depth) used in this calculation. The mixture in the reactor is assumed to be uniform at any instant and the dissociated radicals seeded by the plasma are instantly distributed throughout the volume. The reactor is thermally insulated besides the energy input from the pulsed plasma. The energy supplied by one plasma pulse is 0.2 mJ (10 W and 50 kHz pulsed plasma). The energy input is simulated by adding dissociated radicals (e.g. H and O atoms) into the reactor without elevating the temperature.

The plasma model described in Section 5.1 is employed and the amount of dissociated radicals calculated from the model is supplied to the reactor each pulse period (20 μs with 50 kHz repetition rate). Reactions occurring during the pulse period are simulated by the method presented in Section 5.2. The simulation spans 200 μs time duration while total ten plasma pulses, in the case of the 50 kHz pulsed plasma, generate radicals from the equimolar H₂/O₂ mixture.

5.3.2. Effect on Ignition Delay

A graph presented in Fig. 5.5 confirms the result experimentally proven in Chapter 3, which is the effect of the pulsed plasma, shortening ignition delay time of a flammable mixture. Figure 5.5 (a) shows the temperature histories of the mixture in the absence of the plasma under various initial mixture temperature conditions while the temperature histories in the presence of the plasma are presented in Fig. 5.5 (b), the first plasma pulse is applied at 20 μs after the start of the time duration. The plasma pulses are indicated by the black upward arrows in Fig. 5.5 (b). The abrupt temperature rises appearing in the graphs indicate the ignition of the mixture in the reactor. As shown in Fig. 5.5 (a), the ignition delay time shortens with an increase in the initial mixture temperature. The ignition delay time is approximately 30 μs at a 1300 K initial temperature condition while the mixture is not ignited in 200 μs when the mixture temperature is lower than 900 K. On the other hand, faster ignitions are

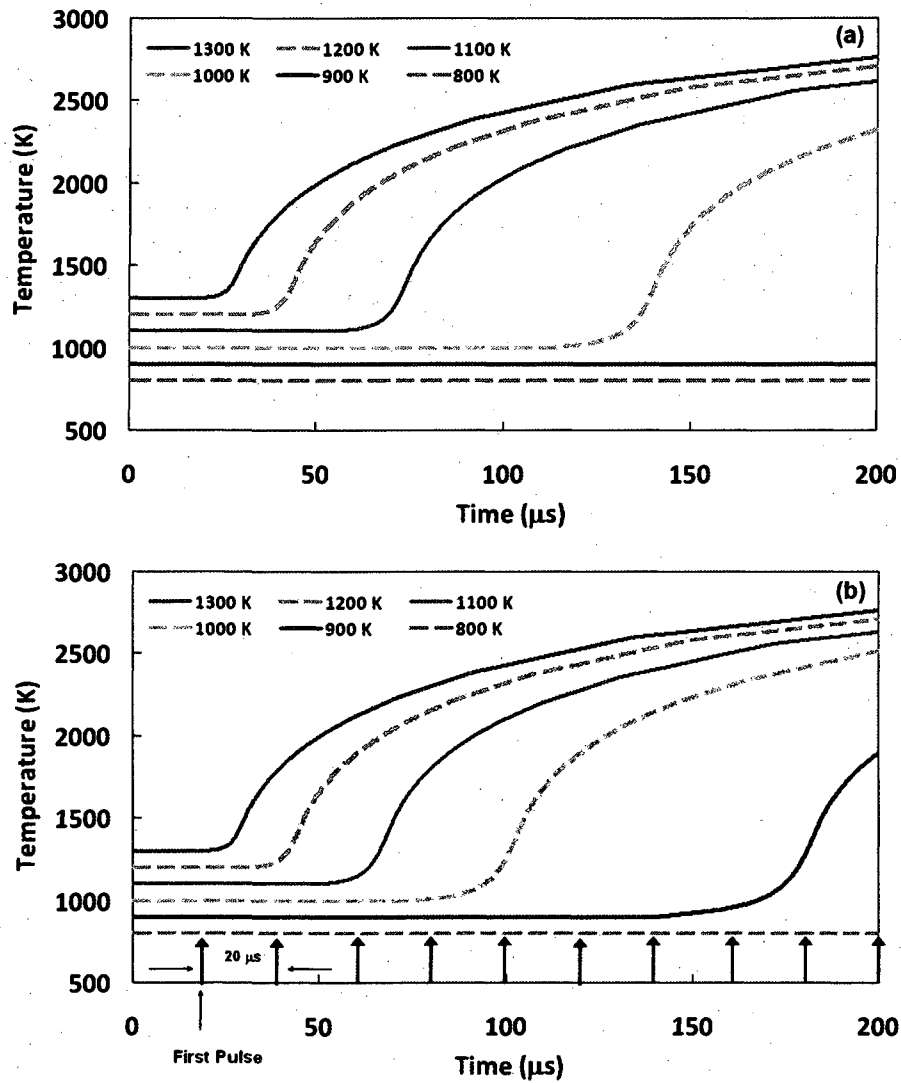


Figure 5.5 Temperature of the equimolar H_2/O_2 mixture vs. time: (a) without the pulsed plasma and (b) in the presence of the plasma (50 kHz and 10 W).

observed in Fig. 5.5 (b) with the same initial mixture temperatures although the reduction of ignition delay by the plasma is negligible under high temperature conditions over 1200 K. Approximately 40 μs of the ignition delay time reduction is achieved by the application of the 10 W pulsed plasma at a 1000 K initial mixture temperature condition.

Figure 5.6, the graph of the radical concentrations in logarithmic scale as a function of time, depicts that only the first few plasma pulses are mostly responsible for the ignition of the flammable mixture in 200 μs under the given temperature and concentration condition (900 K equimolar H_2/O_2 mixture). The blue, red and black curves represent the concentration history of H, O and OH radicals, respectively. The bold solid curves illustrate the radical concentrations in the presence of the pulsed plasma and the lighter dashed curves represent those in the absence of the plasma. The first plasma pulse is applied at 20 μs , and the timing of the pulses are indicated by black downward arrows. The first plasma pulse causes a significant jump in the radical concentration when compared to that concentration without the plasma while no hint

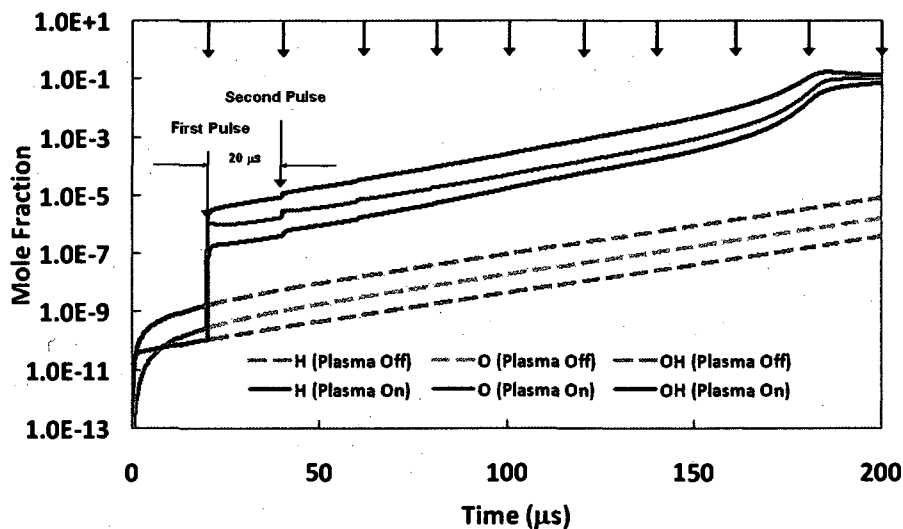


Figure 5.6 A graph of the mole fractions of the radicals (H, O and OH) vs. time under 900 K initial temperature condition (equimolar H_2/O_2 mixture).

of the radical seeding by the fourth and the following pulses is observed. The effect of the second and third plasma pulses also appears negligible compared to the effect of the first pulse because the trends of the exponentially increasing radical concentrations after the application of the first pulse are not changed by the following pulses. The concentration peaks of the three radicals appear at approximately 180 μs when the abrupt temperature rise, indicating the ignition of the mixture, is observed in Fig. 5.5 (b).

The radical supply due to the first plasma pulse represented by the sudden increment of the mole fractions of O, H and OH radicals at 20 μs is only on the order of 10^{-6} . However, with the flammable mixture (H_2/O_2), the radical production becomes on the order of 10^{-1} in mole fractions due to the combustion reaction triggered by the pulsed plasma in a very short time (200 μs). As a result, the pulsed plasma becomes a much more productive radical source in harmony with the flammable mixture as discussed in Section 4.1.

On the other hand, a mixture of 500 K initial temperature (which is lower than the minimum temperature for auto-ignition), requires multiple plasma pulses (10 W and 50 kHz) for ignition. As shown in Fig. 5.7, the build-up of O radicals by the plasma pulses is evident while the base line of the H radical concentration stays almost steady. The difference is due to the faster decay of the H radical under this condition between the plasma pulses. In other words, the H radical has a shorter radical recombination time scale than that of the O radical. However, the recombination reaction is an exothermic reaction releasing heat to the mixture, which implies that the energy deposition from the plasma is accumulated in the mixture although the H radical build-up is not remarkable during the 200 μs time span. As a result, the accumulated energy and the radicals will be able to initiate the combustion of the mixture assisted by the multiple plasma pulses at some time later than 200 μs . The OH radical build-up is also depicted in the graph although its mole fraction is quite low. The OH radical production aided by the H/O seeding from the plasma, modeled as the H/O radical supplier, is shown in detail in Section 5.3.4.

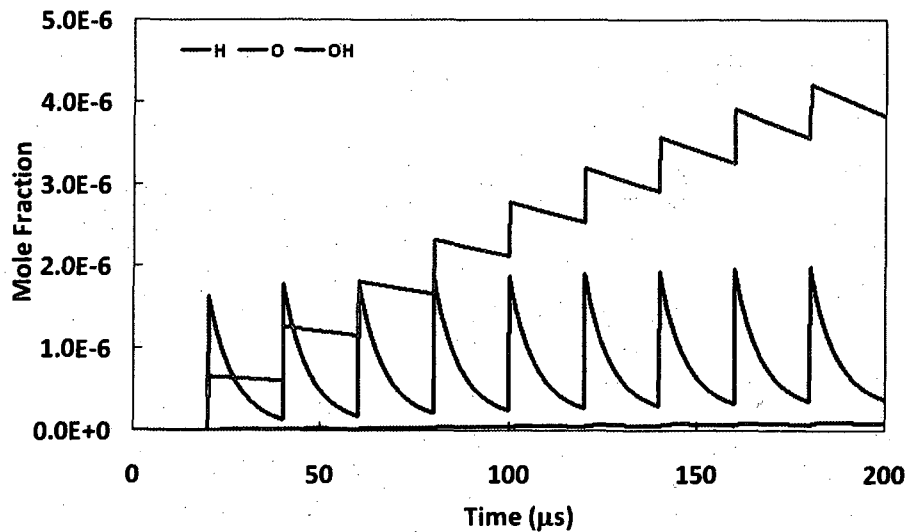


Figure 5.7 A graph of the mole fractions of the radicals (H, O and OH) vs. time under 500 K initial temperature condition (equimolar H₂/O₂ mixture).

5.3.3. Effect of Plasma Power

The effect of the pulsed plasma of higher power up to 100 kW is illustrated in the graph of Fig. 5.8. The initial mixture temperature is fixed at 900 K and the plasma power is varied from 10 W to 100 kW. As expected, the ignition delay time gets shorter with increasing the plasma power. A plasma of power higher than 5 kW (100 mJ per pulse) causes an immediate temperature rise with the first plasma pulse applied at 20 μs. According to the plasma model described in Section 5.1.2, the production of dissociated atom radicals is proportional to the plasma power. Therefore, a 10 kW plasma corresponds to a thousand times the radical supply to the mixture in comparison to the 10 W plasma, providing confirmation that the radicals provided by the plasma source may play an important role in reducing the ignition delay time. It is further found that going from 10 W to 10 kW plasma power reduces the temperature rise time by only a factor of 3.

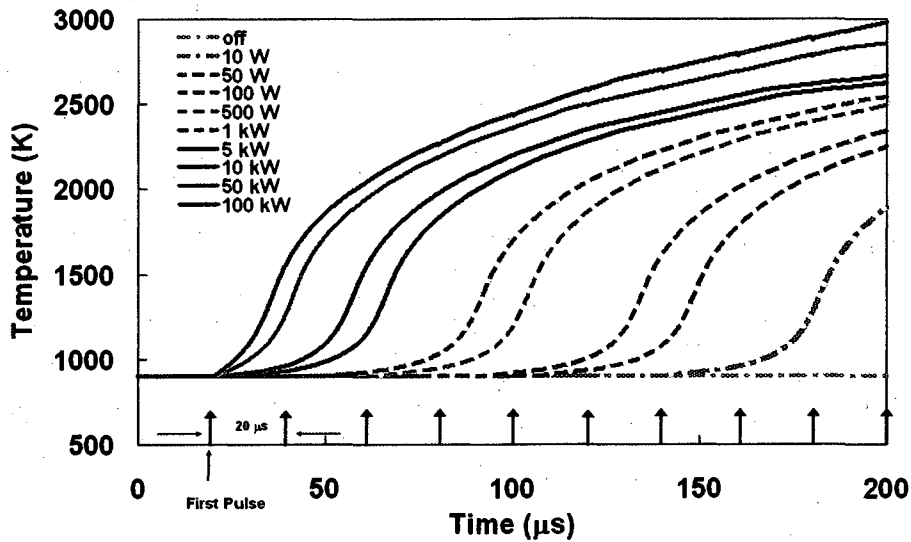
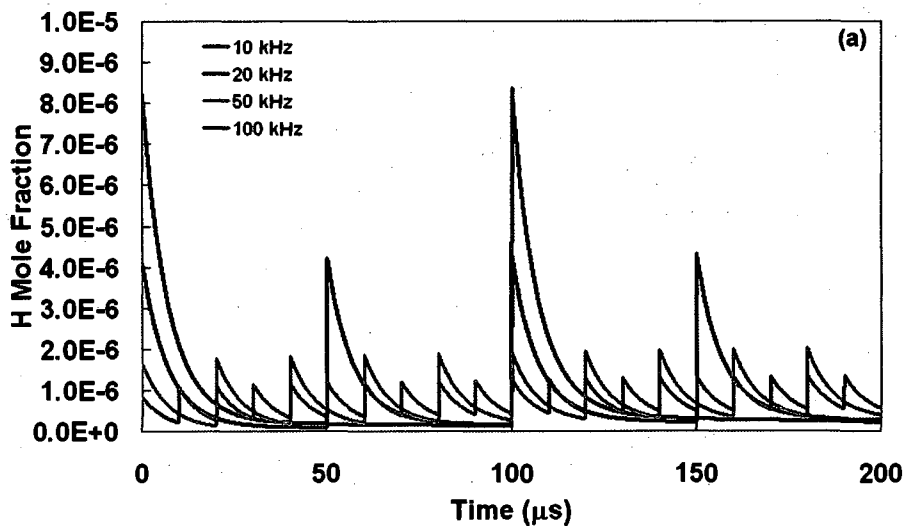
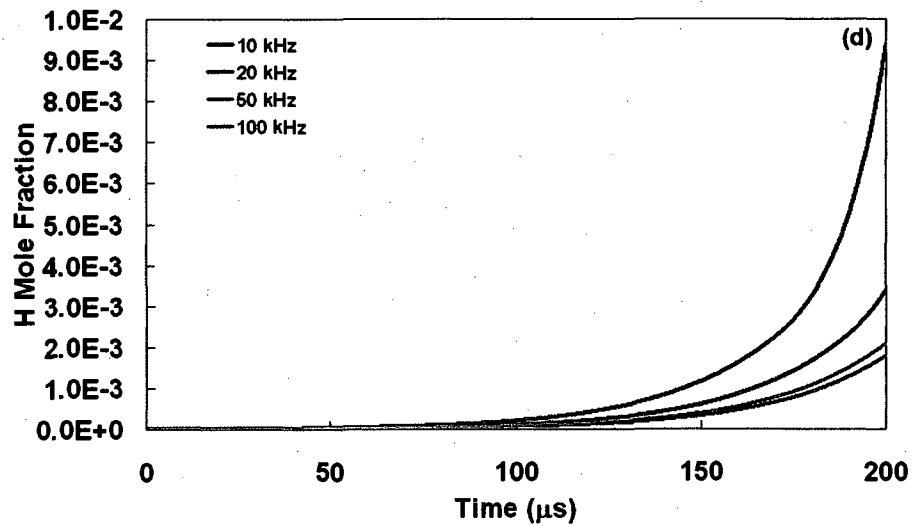
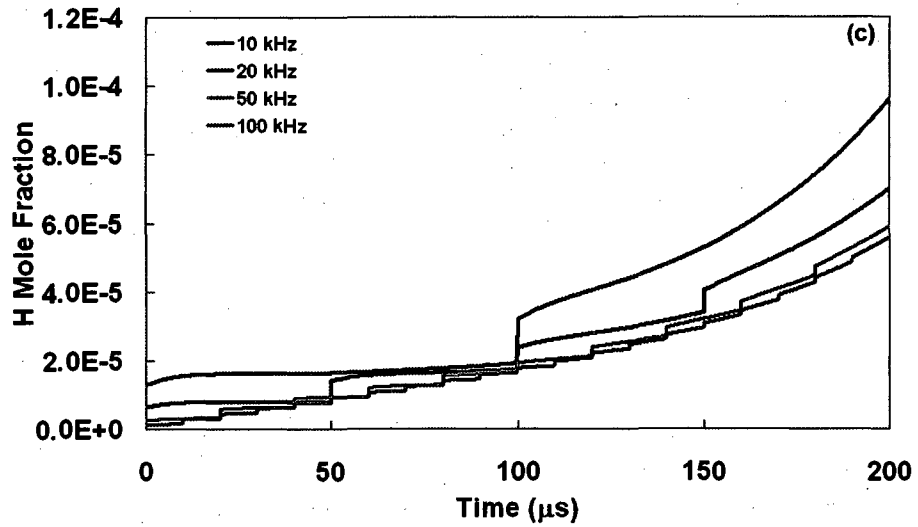
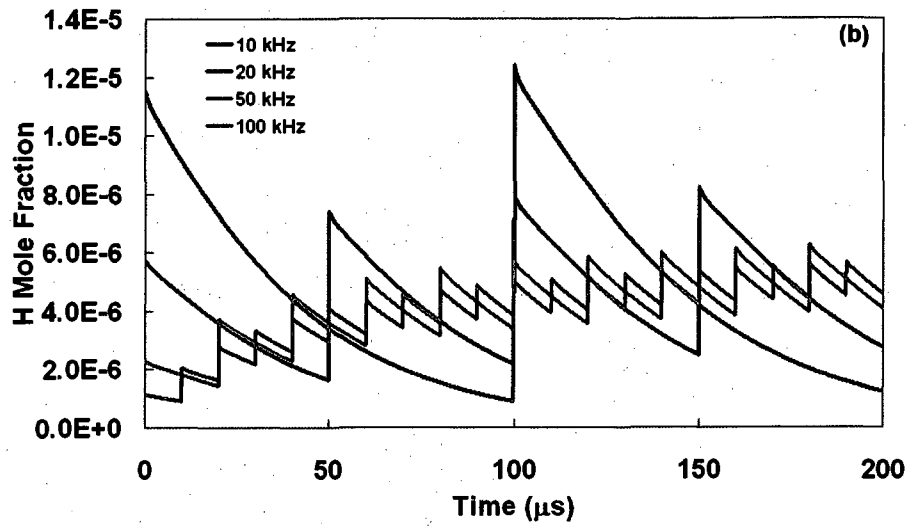


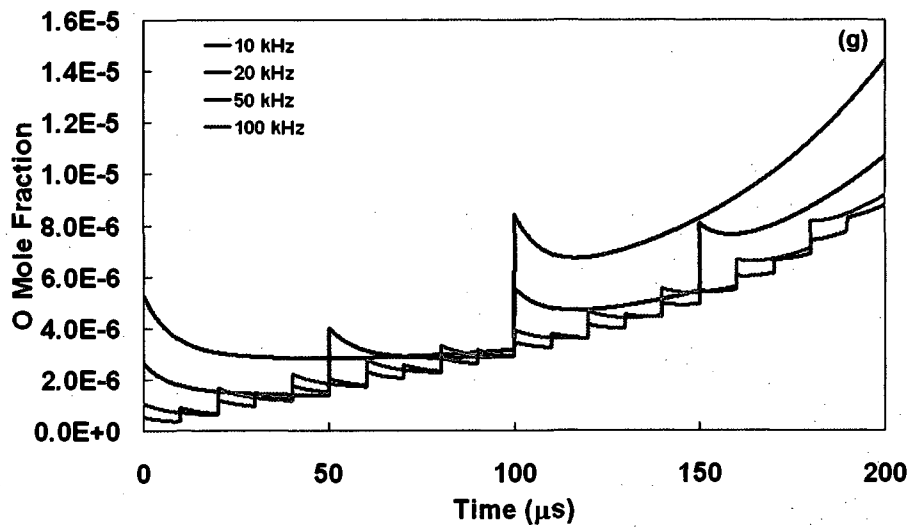
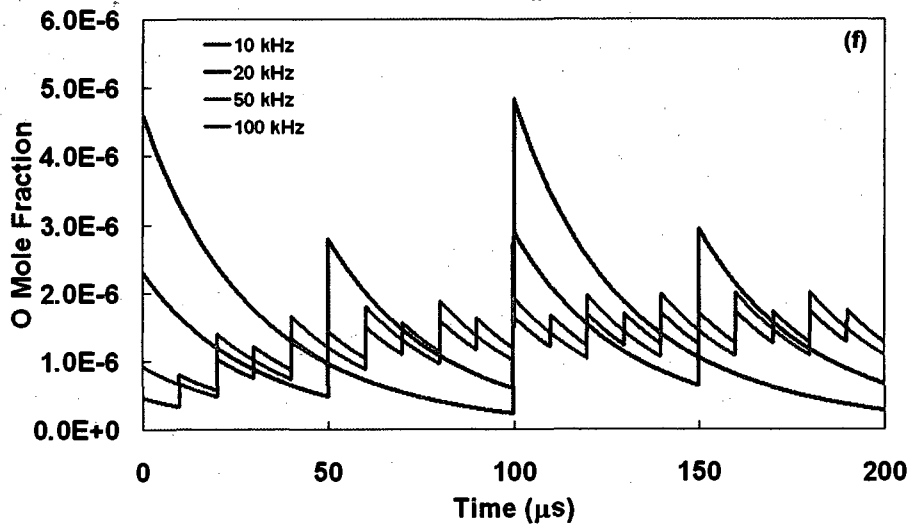
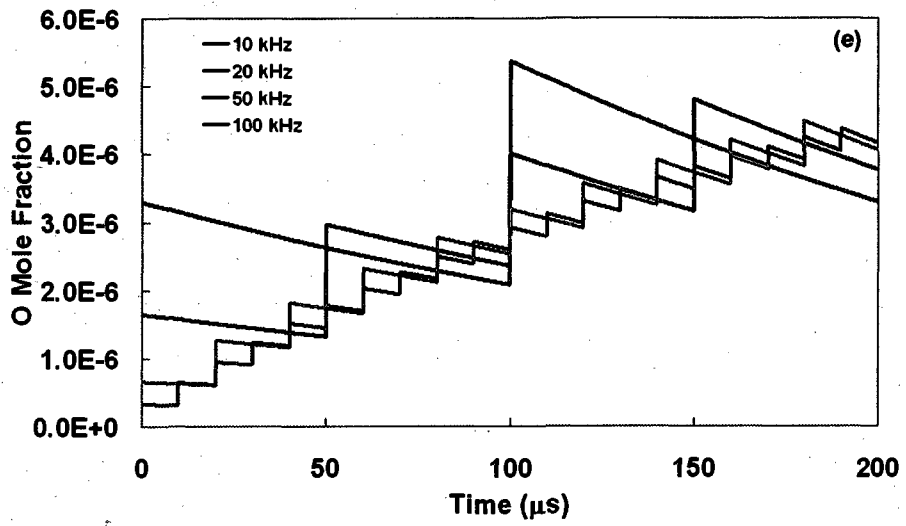
Figure 5.8 A graph of the temperature of the equimolar H_2/O_2 mixture vs. time with the pulsed plasma (50 kHz) of varying plasma power from 10 W to 100 kW.

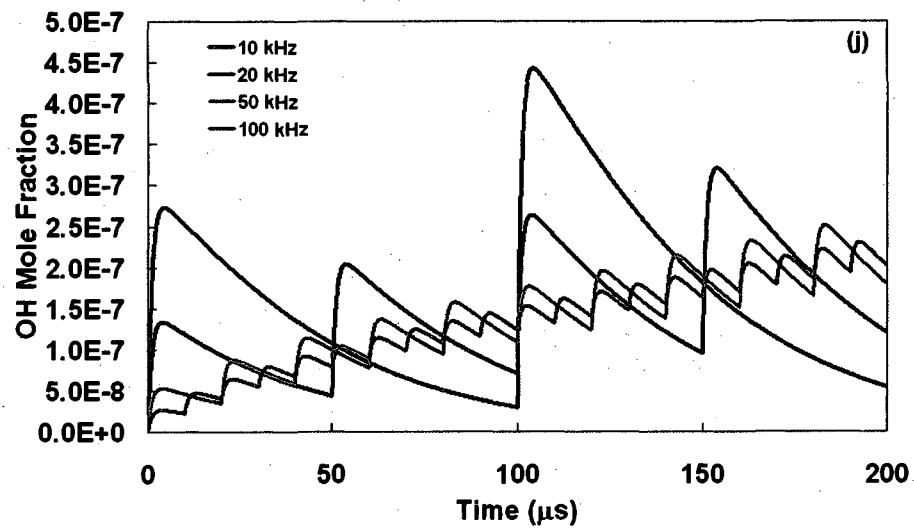
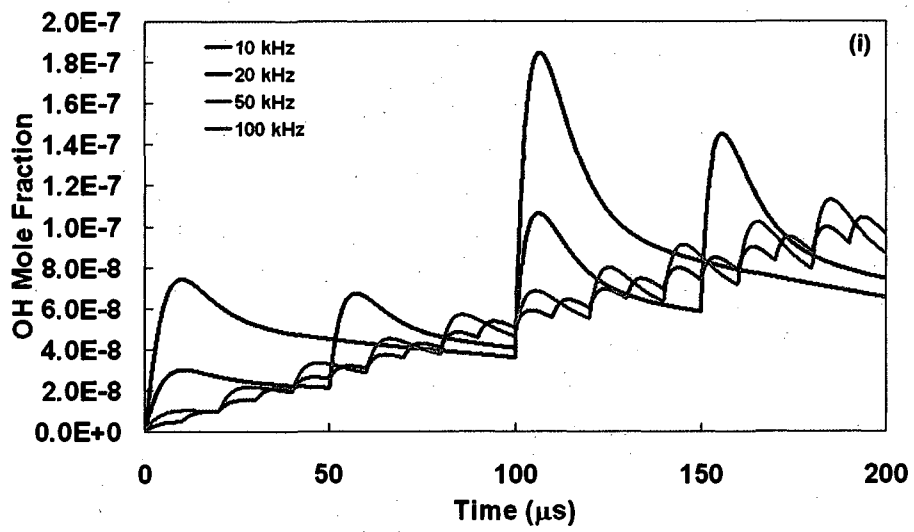
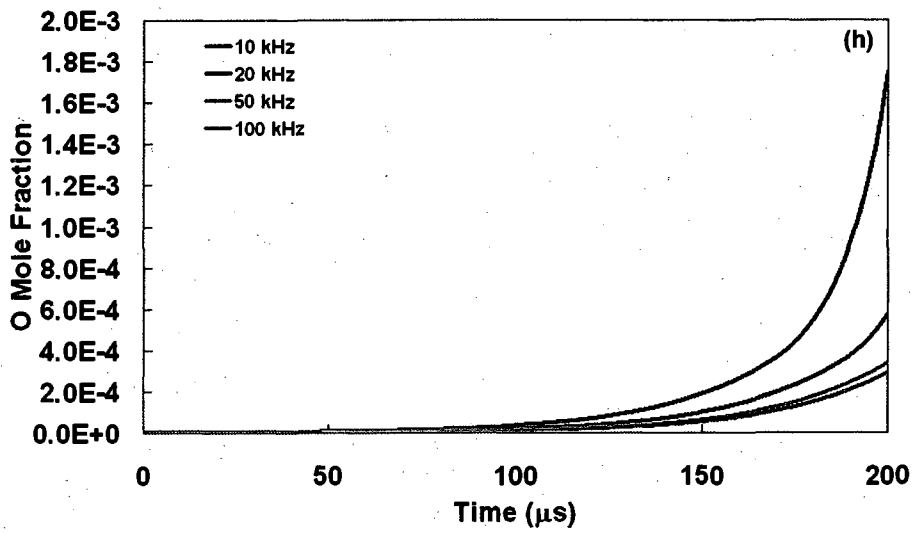
5.3.4. Effect of Plasma Frequency

The effect of plasma pulse frequency at a fixed plasma power (10 W) is shown in Fig. 5.9. The graphs of Fig. 5.9 (a) – (d) are for H, Fig. 5.9 (e) – (h) are for O and









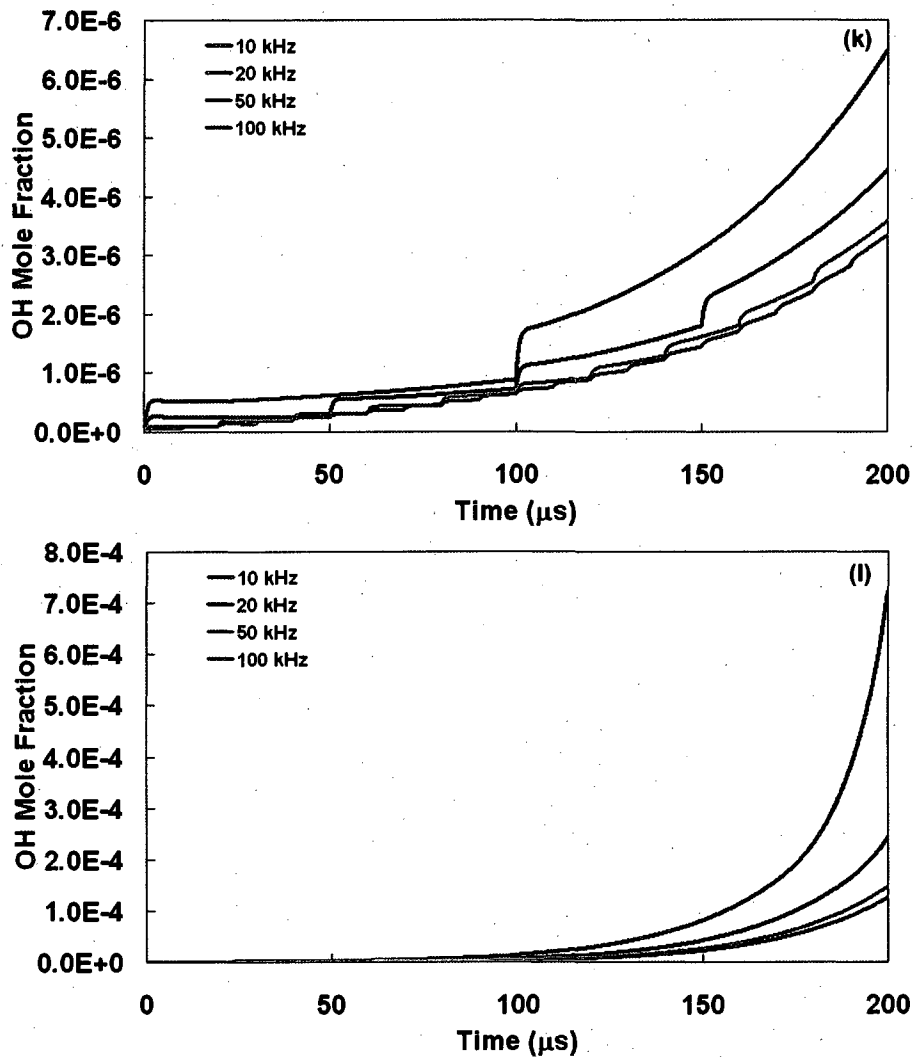
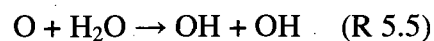
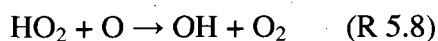
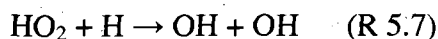


Figure 5.9 Graphs of radical ((a) – (d): H, (e) – (h): O and (i) – (l): OH) mole fractions vs. time with the pulsed plasma of varying frequency from 10 kHz to 100 kHz under (a), (e) and (i): 500 K, (b), (f) and (j): 700 K, (c), (g) and (k): 800 K, and (d), (h) and (l): 850 K initial mixture (equimolar H_2/O_2) temperature conditions.

Fig. 5.9 (i) – (l) are for OH radical concentration. The plasma pulse frequency is varied from 10 kHz to 100 kHz under (a), (e) and (i): 500 K, (b), (f) and (j): 700 K, (c), (g) and (k): 800 K, and (d), (h) and (l): 850 K initial temperature conditions of the equimolar H₂/O₂ mixture. For the comparison of the radical production in the simulation time span (200 μs), the first pulses of the various frequency plasmas are applied at the time of t = 0 μs. The radical production by one plasma pulse decreases with an increase in the frequency because the energy deposition by one plasma pulse is inversely proportional to the frequency for the fixed plasma power constraint. However, the troughs of the radical mole fractions are deeper under lower frequency conditions (in Figs 5.9 (a), (b), (e), (f), (i) and (j)) because the radical concentration decays during the longer time period (longer pulse period) with lower frequency. On the other hand, no trough in the radical mole fraction appears under the higher temperature mixture conditions (800 K in Figs 5.9 (c), (g) and (k), and 850 K in Figs 5.9 (d), (h) and (l)) and the combustion reaction, shown as the exponential radical concentration increase, is initiated in Figs 5.9 (d), (h) and (l). Similar to the case explained in Section 5.3.2, only the first plasma pulse or a few following pulses are needed to initiate combustion of the mixture at 850 K initial temperature (Figs 5.9 (d), (h) and (l)) while more plasma pulses are required for the ignition at the lower initial temperature cases as shown in Figs 5.9 (a), (b), (c), (e), (f), (g), (i), (j) and (k). It is noteworthy that the OH is not produced by the plasma itself as modeled in Section 5.1. The OH is produced by chain (R 5.3 – 5.5)/recombination (R 5.6) reactions and H/O reactions with product species such as HO₂ and H₂O₂ (R 5.7 – 5.11). These reactions (Li et al. (2004)) are prompted by the sudden increase of H/O radicals supplied by the plasma. Therefore, the OH concentration peaks appear slightly delayed from the plasma pulsing time.





In this simulation, the plasma energy deposited into the mixture during the time span (200 μs) is the same in all of the frequency conditions. However, the radical concentrations at the end of the time period are different. In Figs 5.9 (a), (b), (e), (f), (i) and (j) when the radical consumption reactions are faster than the radical production reactions of the mixture during the period between the plasma pulses, the higher frequency plasma provides more radicals as a result of the same energy deposition (2 mJ in 200 μs). On the contrary, the radical production with the lower frequency plasma is greater in Figs 5.9 (c), (g) and (k) under the higher initial mixture temperature condition (800 K). In this case, radical production is faster than the consumption. As a result, the radical concentration increases between the plasma pulses. In Figs 5.9 (d), (h) and (l), the mixture is ignited earlier with the lower frequency plasma because, under this high temperature condition, only the first plasma pulse is needed to initiate the combustion reaction as shown in Fig. 5.6 (900 K initial temperature condition) and the energy deposition from the first plasma pulse is greater for lower frequency condition. Consequently, the effect of the plasma frequency, in terms of the radical production, varies depending on the initial temperature of the mixture.

Another issue to be considered for the estimation of the plasma frequency effect is the radical removal effect by convection in the presence of gas flows through the plasma region. Presumably, a continuous radical source or a high frequency pulsed radical source is beneficial for sustaining reactions with the fast radical removal from the plasma region. Especially in supersonic flows, the radical removal by convection is fast enough to be considered even with the high frequency pulsed plasma used in the current study (50 kHz). The estimation of the minimum plasma frequency for

sustaining the combustion reactions is beyond the scope of this study. However, as shown in the Section 4.3.6, it is experimentally proven that a pulsed plasma of 50 kHz frequency is capable of sustaining combustion in a Mach 2.4 flow.

5.4. Modeling of Dual Fuel Jet Injection

The simulation conducted in this section is aimed at the validation of the phenomena observed on a flat wall with dual hydrogen fuel jet injection in Chapter 4.

5.4.1. Assumptions and Simulation Procedure

Figure 5.10 summarizes the simulation procedure and the assumptions made to analyze the complex reacting flow phenomena as a zero dimensional reaction process

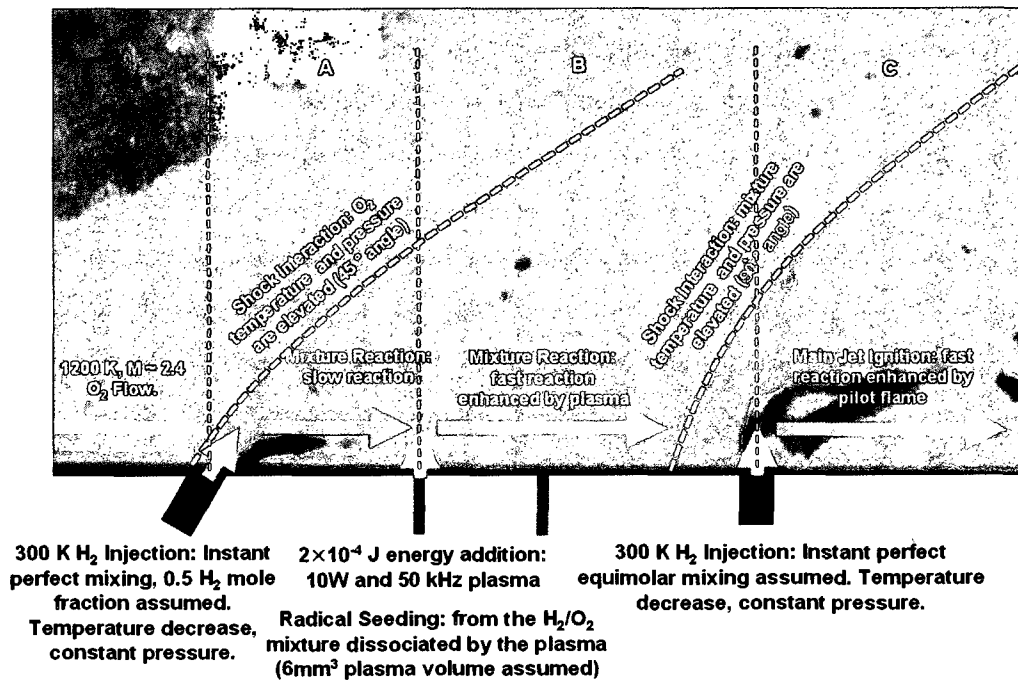


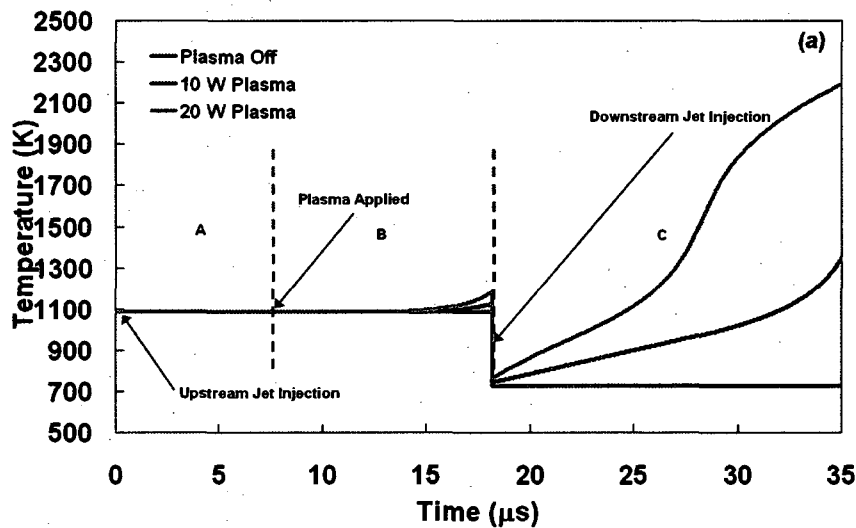
Figure 5.10 Simulation procedure and assumptions for validation of the flat wall model with the dual fuel jet injection configuration.

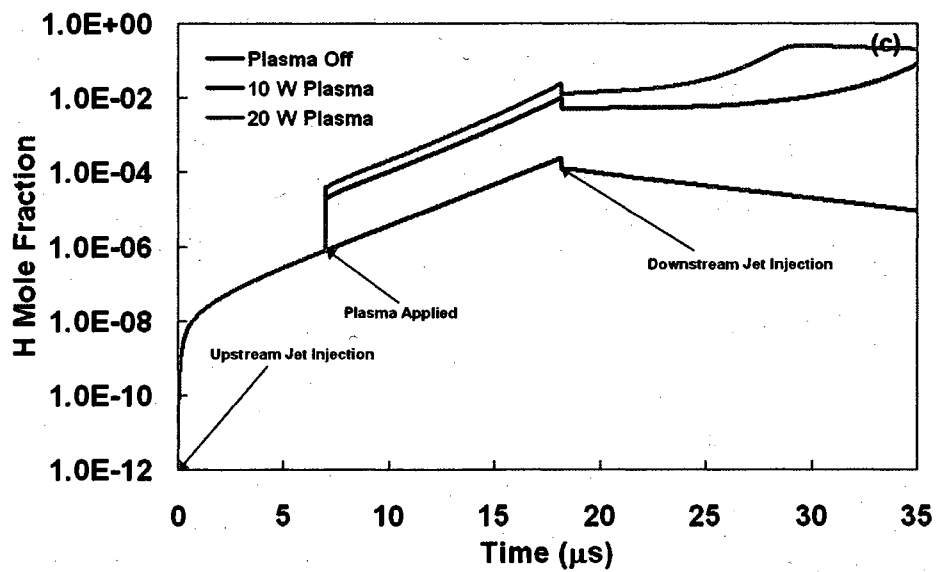
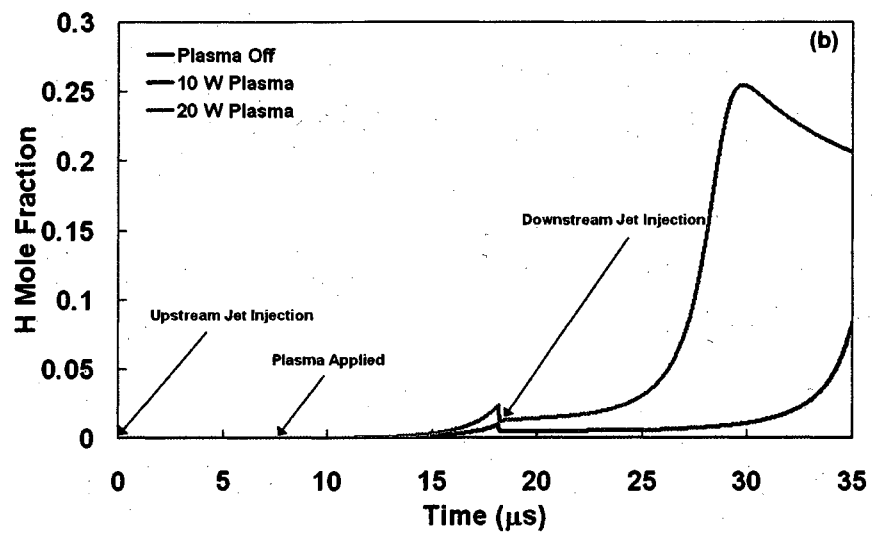
simulating the reactions occurring in a small volume moving on the surface of the model. Molecular diffusion, mixing, expansion waves behind the shocks and heat transfer are not considered, and instant (perfect) mixing is assumed within the volume, constant enthalpy (besides plasma energy deposition and fuel jet injection), nominal fuel concentrations, and shock angles are prescribed, in some cases, as guided by experiments.

As described in Fig. 5.10, the region of interest of this study is divided into three parts: the upstream jet injection, the seeding of the dissociated species from the pulsed plasma and the downstream jet injection. The use of the pure oxygen supersonic flow ($Ma \sim 2.4$, $T_{static} \sim 1200$ K, $P_{static} \sim 25$ kPa and $h_0 \sim 2.5$ MJ/kg) generated by the expansion tube is assumed in the simulation with negligible oxygen molecule dissociation (order of 10^{-11}) before the injection of the upstream jet. The freestream flow, with elevated temperature and pressure by the jet induced bow shock (nominally assumed 45° angle), is instantly mixed with the upstream fuel jet (300 K hydrogen) resulting in an equimolar H_2/O_2 mixture; mixing with the cold hydrogen fuel causes the mixture temperature to drop. Then, the mixture moves to the cathode region at 80 % of the freestream flow speed near the surface. In region A, between the upstream jet and the cathode, the mixture undergoes slow initiation reactions. The O and H radicals produced by the pulsed plasma (10 W, 50 kHz and 6 mm^3 volume) are supplied to the mixture (2×10^{-4} J energy deposition via the supply of the dissociated radicals) when the mixture arrives at the cathode region. Due to the radical seeding, rather faster reactions occur in region B between the cathode and the downstream jet and, in some cases, the pilot flame igniting the downstream jet flame is ignited in this region. The radical containing mixture meets the downstream jet induced bow shock (nominally 90° angle assumed) followed by the instant mixing with the 300 K hydrogen fuel injected by the downstream jet nozzle; the mixing causes an abrupt temperature drop at the fuel injection point. The same mole fraction of the hydrogen fuel from the downstream jet and the mixture is assumed in the leeward side of the jet. Finally, the reactions occur while the mixture travels through region C at the downstream of the downstream jet.

5.4.2. Ignition of the Pilot Flame by the Pulsed Plasma

Figure 5.11 shows the temperature (Fig. 5.11 (a)) and radical concentration (Figs 5.11 (b), (c), (d) and (e)) time histories of the H_2/O_2 mixture in the small volume travelling over the surface of the model. The temperature and the radical concentrations of the mixture increase in region B in the presence of the plasma while they remain almost unchanged without the plasma, which is coincident with the experimental observation in Fig. 4.8. It is noteworthy that the radical production of the plasma is only on the order of 10^{-6} while the radical concentration in front of the downstream jet (the boundary between the region B and the region C) is on the order of 10^{-2} . As discussed in Chapter 4, the plasma effect is clearly amplified by the combustion reaction in region B (the pilot flame). Figure 5.11 (b), the H radical concentration versus time, describes well the amplification of the radical production in region B and its effect on the downstream jet flame. Figure 5.11 (c): H, (d): O and (e): OH illustrate in more detail the time evolution of the radicals with logarithmically scaled radical concentrations. The one plasma pulse applied at around $7 \mu s$ causes the sudden increase in the radical concentrations to initiate fast radical production reactions (pilot flame) in region B, which is consistent with the result shown in Fig.





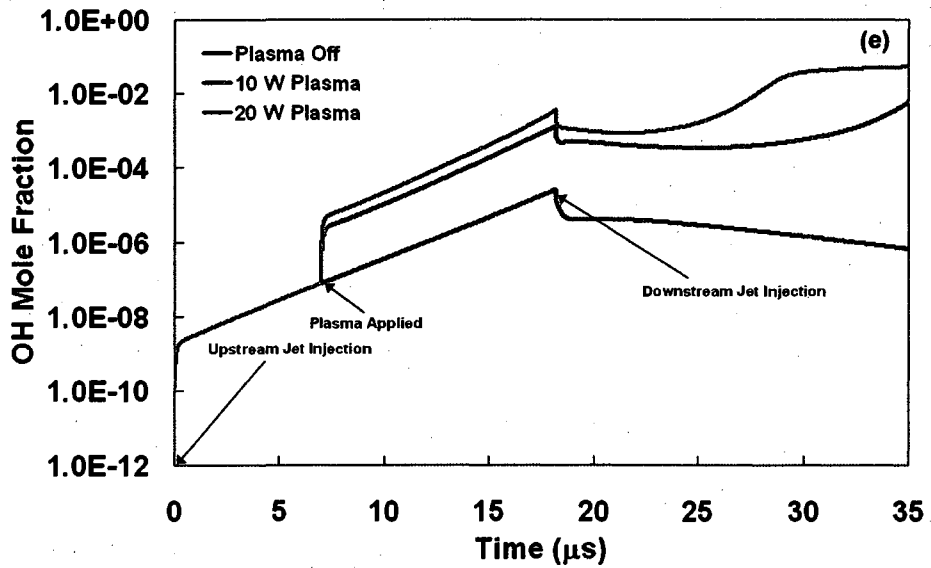
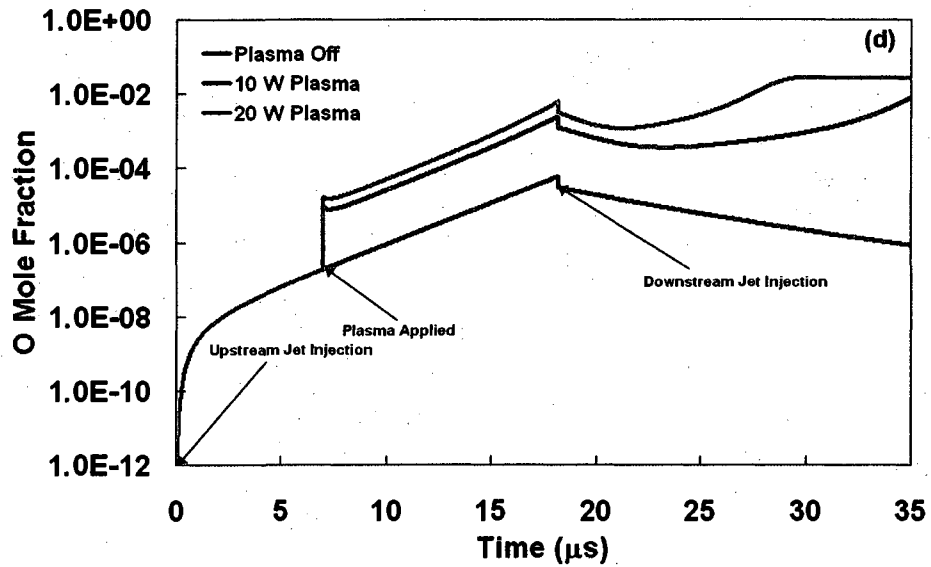


Figure 5.11 Graphs of (a) temperature and radical ((b) and (c): H, (d): O, and (e): OH) mole fractions as a function of time revealing the effect of the dissociated radicals produced by the pulsed plasma.

5.6: only one plasma pulse is primarily responsible for the ignition in a 900 K equimolar H₂/O₂ mixture. The three radicals (H, O and OH) show similar trends, the ignition at region C with the plasma and the concentration decay in the absence of the plasma after the downstream jet injection, although differences in the production/consumption rate and the absolute concentration values of the radicals are observed. In addition, the higher plasma power (20 W) causes a greater increase in temperature and the radical concentrations in front of the downstream jet, which implies the higher plasma power produces a more effective radical source aided by the combustion reaction (the pilot flame). Finally, the effect can be extended (propagated) into the freestream flow region by the addition of a downstream jet which will be explained in the next section.

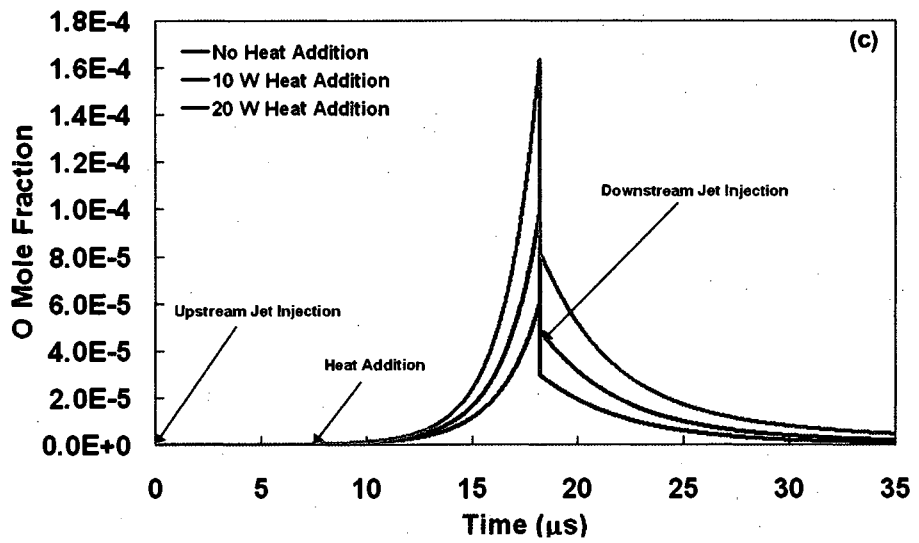
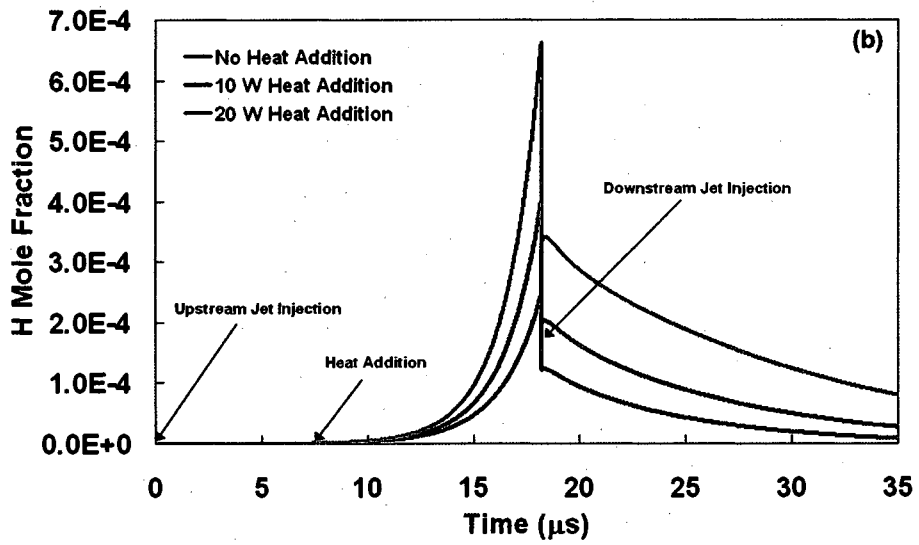
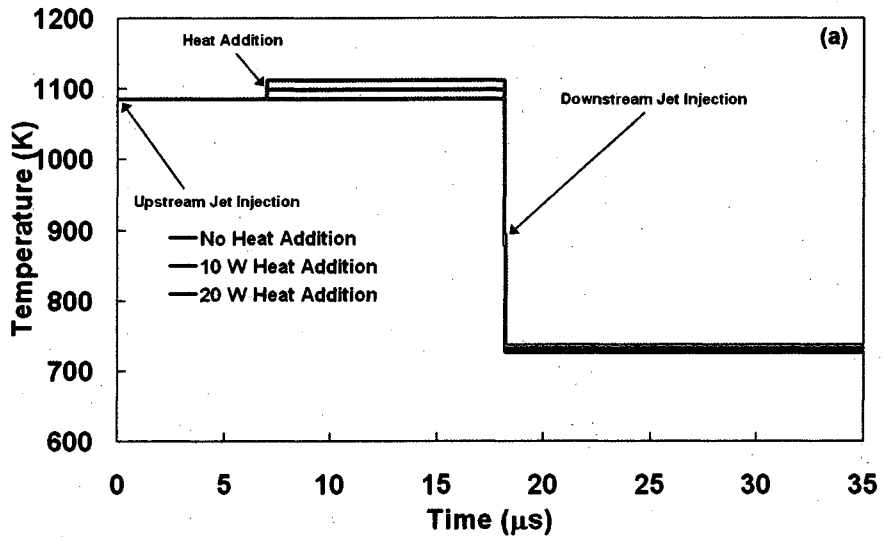
5.4.3. Ignition of the Downstream Jet Flame by the Pilot Flame

The difference between the plasma on and off cases becomes more obvious in region C as shown in Figs 5.11. The temperature and the radical concentration differences of the two cases are magnified again, in the downstream jet flame region; immediate temperature and radical concentration rises are observed in the presence of the plasma while these remain steady without the plasma. The observation is consistent with the experimental result presented in Chapter 4. This reveals that a low power plasma (10 W) is capable of igniting the downstream jet flame in the duel fuel jet injection configuration despite its negligible energy deposition compared to the combustion energy release (order of 10^{-5} as explained in Section 4.3.5). It is noteworthy that the fuel/oxidizer mixture of approximately 700 K static temperature at the downstream jet injection point is ignited immediately (abrupt temperature rise at the point in the presence of the plasma) aided by the radicals supplied from the pilot flame. The effect of the pilot flame is comparable to the effect of the plasma of much higher power (over 10 kW) as observed in Fig. 5.8 although only 10 W or 20 W plasma power is deposited into the mixture. This confirms the enhancement on the plasma effect by the combustion occurring in region B. Also, the increase in the

plasma power from 10 W to 20 W makes a remarkable difference in the temperature and the radical production in the leeward side of the downstream jet, suggesting further enhancement of the plasma effect due to the use of the higher plasma power. Consequently, the result of this simulation provides evidence that the use of the higher power plasma can extend the applicable flow condition of the dual fuel jet injection configuration.

5.4.4. Effect of Heat Addition

Figure 5.12 illustrates the temperature and the radical concentration histories when the power of the plasma is released as heat energy without the electron impact dissociation reactions. The heat release at the cathode region is simulated as a continuous heat source; the swept volume through the discharge region while the mixture passes by the region B ($3.2 \times 10^{-8} \text{ m}^3$: the discharge of a 2 mm arch stretched over the surface, 1 mm discharge diameter and 16 mm distance between the cathode and the downstream jet) is heated by the heat source. The instant temperature rise by the heat release is assumed at the cathode position, expressed in Fig. 5.12 (a) as a step temperature rise. The temperature rise is calculated to be approximately 10 K to 20 K by the 10 W to 20 W heat addition, representing an increase of 1 % to 2 % in the static temperature. However, no ignition is observed after downstream jet fuel injection even with this heat addition as shown in Fig. 5.12 (a) although the effect of the heat addition is evident in the radical production (Figs 5.12 (b): H, (c): O and (d): OH). As shown in Fig. 5.12 (b), the 20 W heat addition produces 2.5 times more H radicals than the radical production in the region without the heat addition. A similar trend is also observed with O (Fig. 5.12 (c)) and OH (Fig. 5.12 (d)). Nevertheless, the radicals are recombined and consumed in the region C due to the temperature decrease caused by the cold (300 K) downstream fuel jet injection. The result reveals that the power used by the plasma to produce dissociated radicals is more effective in initiating the combustion reactions in a short time span than the same amount of energy deposition as heat.



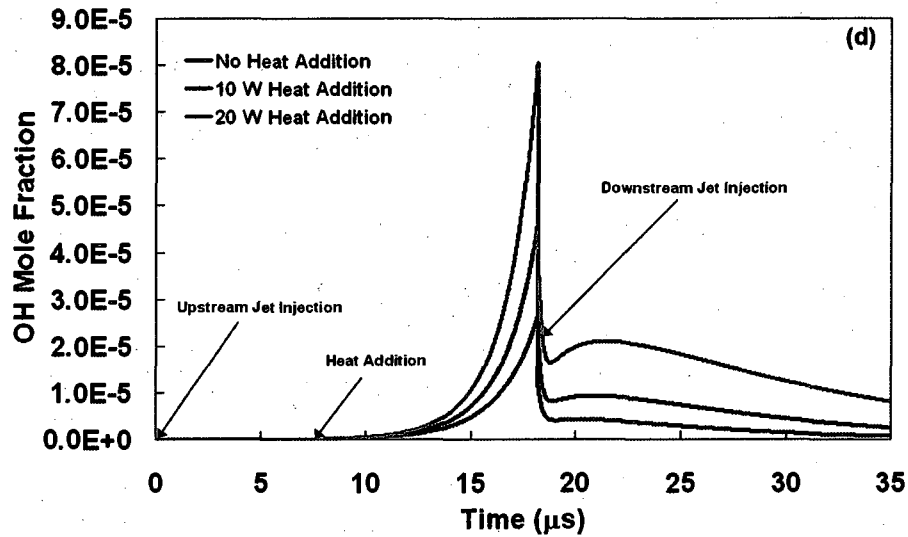


Figure 5.12 Graphs of (a) temperature and radical ((b) H, (c) O and (d) OH) mole fractions as a function of time showing the effect of heat energy deposition (the same amount of the energy of one plasma pulse).

5.5. Summary

The simplified numerical method utilized in this chapter validated the experimental results and estimated the prospective use of the plasma of variable frequency and power. The results of the simulations are summarized as follows:

- A higher temperature H_2/O_2 mixture has a shorter ignition delay time.
- The pulsed plasma (10W and 50 kHz) is capable of reducing ignition delay time of the flammable mixtures significantly when the initial mixture temperature is in the range between 900K and 1200 K.

- Under relatively high initial mixture temperature conditions (> 850 K), the plasma (10 W) can ignite the mixture with only one or just a few plasma pulses.
- A plasma of higher power further reduces the ignition delay time: 10 kW plasma can immediately ignite 900 K equimolar H_2/O_2 mixture.
- The investigation of the effect of the plasma frequency with a fixed power (10 W) reveals that the better choice of the frequency for flame ignition and sustainability depends on the conditions of the flammable mixture: the initial temperature of the mixture and the convection speed of the flow removing the radicals from the plasma region.
- The simplified zero dimensional simulation of the dual fuel jet injection model describes well the experimental result; the upstream jet flame ignition assisted by the pulsed plasma (only one plasma pulse) and the downstream jet flame ignition by the upstream jet flame.
- A pilot flame as the radical source amplifies the radical production of the plasma.
- The pulsed plasma is effective in flame ignition serving as a radical source, but not as a heat source.

The numerical analysis conducted in this chapter suggests that a high power pulsed plasma is capable of expanding applicable flow conditions of plasma assisted combustion to harsher conditions. One of the motivations of this study is flame stabilization at the low enthalpy regimes in supersonic flow, as expected in the combustor of hypersonic aircrafts under low Mach number flight. This enhancement is critical as there have been demonstrated difficulties in starting scramjet engines under low Mach number flight conditions. The simulation described here confirms that the nonequilibrium plasma can be enhanced by the supply of the flammable mixture into

the discharge region. It also confirms that even the low power plasmas studied experimentally can be effective in stabilizing combustion reactions under harsher conditions when the flammable mixture's flow condition adjacent to the plasma is further optimized.

Chapter 6 Conclusions

In this study, the effectiveness of flame stabilization methods utilizing a nonequilibrium nanosecond pulsed plasma in supersonic flows is investigated. The jet flame regions are visualized using OH PLIF imaging, while the overall supersonic flow fields are characterized using Schlieren imaging. The jet flames in the supersonic crossflows are ignited and sustained or assisted by the pulsed plasma in a cavity located in the leeward side of the jet and also on a flat wall without the cavity. In this chapter, the results of the experiments and the numerical modeling/validation of the plasma assisted flame stabilization mechanism are summarized. Based on the results, recommendations for future work are presented.

6.1. Experimental Results

The experimental results presented in Chapter 3 and Chapter 4 are summarized in this section.

6.1.1. Cavity Flame Stabilization

- The conventional cavity flame stabilization method was tested. The application of this method resulted in flame ignition in the leeward side of an oblique hydrogen jet; the cavity flame is auto-ignited during the expansion tube test time (300 – 500 μ s) when the enthalpy of the freestream flow is higher than 2 MJ/kg.
- Coincident with the previous studies conducted by Heltsley et al. (2008) and Ben-Yakar (2001), a filamentary flame in the windward side of the hydrogen jet, over the cavity region, is observed when the supersonic crossflow enthalpy is higher than 3

MJ/kg. The cavity flame and the filamentary flame are separated by the trajectory of the jet core, which is not ignitable due to its high fuel concentration.

- The nanosecond pulsed plasma applied in the cavity enhanced the cavity flames. It was confirmed that a reduction in the ignition delay time of the flammable mixture within the cavity is achieved by use of the pulsed discharge plasma.
- The applicability of this plasma assisted combustion technique to general hydrocarbon fuels was confirmed by observation of plasma assisted ethylene jet flame ignition in the cavity.
- The inherent drawback of the plasma assisted cavity flame stabilization methods was revealed in the Schlieren images, which indicate the presence of undesirable shockwaves that are induced by the cavity. These shockwaves are the primary source of the stagnation pressure loss in supersonic flows. Also, the OH PLIF images show that the plasma's effect on the flame is localized within the cavity and its vicinity, indicating that there is limited jet flame propagation into the supersonic freestream.

6.1.2. Flat Wall Flame Stabilization

- A new novel method using dual fuel jet injection on a flat wall was suggested to separate the two roles played by conventional fuel jet combustion in crossflows. These two roles include the production of the radical source and the enhancement of the flame propagation into the supersonic freestream. It was believed that this method can further enhance the effect of the pulsed plasma and to suppress unwanted shockwaves caused by the geometric alterations such as cavities.
- The dual fuel jet injection configuration when aided by the pulsed plasma (placed between the two jets) was found to successfully stabilize the jet flames in pure oxygen supersonic crossflows. The pulsed plasma was applied at the leeward side of the

upstream jet to ignite/enhance a pilot flame, forming a plasma assisted pilot flame radical source that was subsequently effective in enhancing/sustaining the combustion of the downstream jet flame in its windward/leeward side. In addition, it was found that, as intended, the downstream fuel jet facilitates the jet flame propagation.

- The 50 kHz nanosecond pulsed plasma used in this current study was effective in sustaining the jet flames during the whole test time even between plasma pulses.
- Ethylene jet flames were also ignited on flat walls by this proposed flame plasma-assisted dual-jet ignition method.

6.2. Modeling and Simulation Results

The scope of the experiment was determined by limitations in the pulsed power source used in the current study. The maximum power and frequency of the plasma generator was 10 W and 50 kHz, respectively. Therefore, the prospective uses of these nonequilibrium pulsed plasmas for various operation conditions need to be evaluated by modeling and numerical simulations. Such simulations are able to guide in identifying which operation conditions might apply under expanded conditions. The simulations were also used to validate experimental results. The results of the modeling and the simulations are summarized as follows:

- The ignition delay time of an H_2/O_2 mixture varied as a function of its initial temperature with the mixture of higher initial temperature having a shorter ignition delay time. These simulations were conducted under the initial temperature conditions higher than the auto-ignition temperature.
- With the pulsed plasma modeled as a radical source dissociating H_2 and O_2 to produce H and O by electron impact, it was found that the pulsed plasma (10W and 50 kHz) is capable of reducing the ignition delay time of the H_2/O_2 mixture. The

reduction is achieved by the periodic (20 μs period) H and O radical seeding into the mixture.

- Only the first plasma pulse of 0.2 mJ energy was needed to produce enough H and O radicals to ignite the H_2/O_2 mixture (100 mm^3 volume) in 200 μs when the initial mixture temperature is higher than 850 K.

- The use of a higher average power plasma (up to 100 kW) with 50 kHz pulse frequency was simulated. It was found that the higher power plasma pulse further reduces the ignition delay time. An immediate ignition of a 900 K equimolar H_2/O_2 mixture is observed with a 10 kW plasma.

- The use of the plasma pulses of different frequencies (up to 100 kHz) with a fixed power (10 W) was simulated. It was found that the effect of the frequency on flame ignition and flame holding depends on the initial temperature of the H_2/O_2 mixture. A higher frequency plasma produces more H and O in a 200 μs time span under low temperature conditions (500 K – 800 K), while a lower frequency pulse, having a higher energy per pulse (to hold the total plasma power constant), ignites the high temperature mixtures (900 K) faster.

- A simplified zero dimensional simulation validated the experimental results obtained with the dual fuel jet injection. In the time span (30 μs) of the simulation, only one plasma pulse is applied and the upstream/downstream jet flames are ignited in the presence of the plasma pulse while no ignition (temperature rise nor significant exponential increment of H/O radicals) is observed in the absence of the plasma.

- It was found that the pilot flame as the radical source amplifies the radical production of the plasma. H/O radicals produced by one plasma pulse ($\sim 10^{-6}$ mole fraction) trigger the radical production of the upstream jet flame ($\sim 10^{-2}$ mole fraction).

- A comparison of the pulsed plasma as a radical source with the heat addition of the same energy as that of one plasma pulse revealed that the pulsed plasma is effective in flame ignition serving as a radical source, but not as a heat source.

6.3. Recommendations for Future Research

The scope of the current study can be summarized as follows: i) a study of the effect of a combination of plasma enhancement and a cavity on flame stabilization and flame holding in a supersonic conditions, ii) a study of the capability of relatively low power pulsed plasmas in flame stability enhancement using dual fuel jet injection, and iii) numerical simulations which validate and expand the potential use of this dual jet method. These studies provide guidance for future research, further enhancement of flame stability and practical applications of the methods tested in this study. Two particular extensions of these studies are described below.

Dual fuel jet injection with cavity: In Chapter 3, it was found that the drawbacks of the cavity originate from the use of the single jet as well as the undesirable shockwaves induced by the cavity. These result in localized plasma effects in the vicinity of the cavity and stagnation pressure loss. Despite these drawbacks, cavity flame stabilization methods are shown to be capable of producing favorable flow conditions for flame holding in these supersonic environments. Therefore, a study utilizing the merits of cavities is still valuable to guarantee reliable scramjet engine performance in harsh flight conditions.

As shown in Chapter 4, the use of the dual fuel jet injection configuration can enhance the flame propagation into the supersonic freestream flow. Hence, the cavity flame stabilization method can also be improved by adding a downstream jet whereby the cavity flame serves as the radical source (pilot flame) igniting the downstream jet. Figure 6.1 shows the schematic of the dual-jet configuration with a cavity. The pilot flame in the cavity triggered by the plasma may be capable of further extension of the

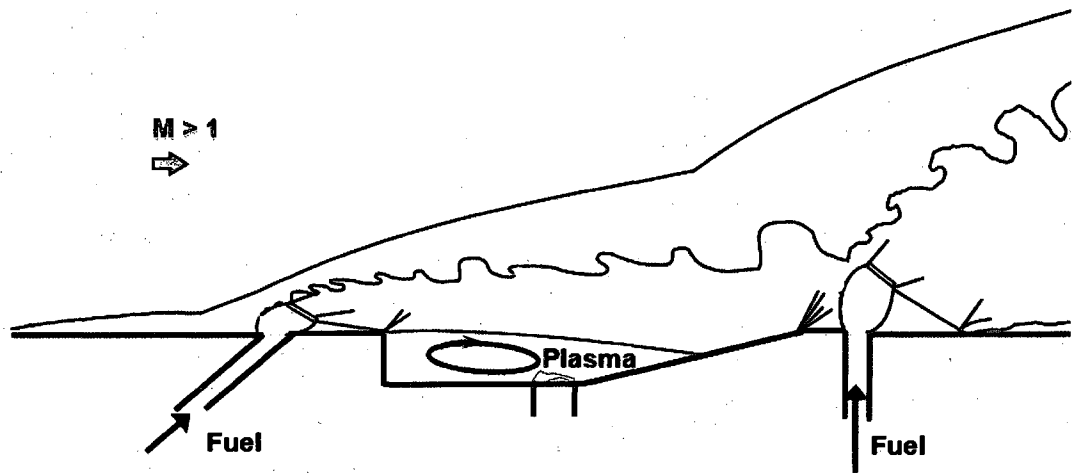


Figure 6.1 A schematic of the dual-jet configuration with a cavity.

method to lower enthalpy flows because the cavity pilot flame would produce more radicals stabilizing the downstream jet flame compared to the case without the cavity.

Multiple fuel jet injection: The experimental results presented in Chapter 4 confirmed the capability of the dual fuel jet injection configuration on a flat wall assisted by the pulsed plasma, igniting and sustaining jet flames with minimized stagnation pressure loss. The capability of the method originates from the use of the upstream jet flame as a pilot flame that ignites the downstream jet. Presumably, multiples of these configurations can further increase the total combustion power by injecting more fuel into the combustor, which is essential for practical application. Also, the use of the oblique jets lessens the stagnation pressure loss in supersonic flow. Therefore, multiple oblique fuel jet injections would be a better solution for maximizing the engine performance and thrust.

Figure 6.2 presents a schematic of the multiple oblique jet injection configuration. As shown with the experimental results presented in Chapter 4, the first oblique jet would be effective in producing a pilot flame when it is a subsonic jet. The

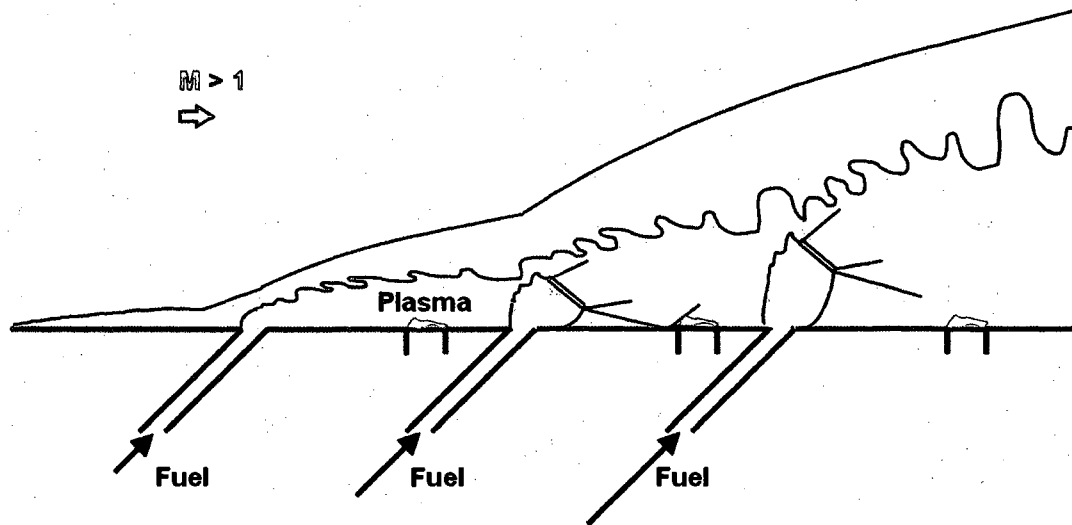


Figure 6.2 A schematic of the multiple oblique fuel jet injection configuration.

following series of the oblique jets could have increasing jet momentum ratios (J) to achieve higher fuel flow rate and the enhancement of jet flame propagation. Further flame stabilization can be achieved by adding the pulsed plasmas in the leeward side of the jets.

Appendix A High Speed Switch Circuit

High speed switching circuits are utilized to produce a high voltage (50 V) pulse (high speed switch circuit #1), to chop long pulse signals to make short pulses (high speed switch circuit #2) and to choose a pulse from a train of repetitive short pulses (high speed switch circuit #3). This appendix presents the detailed specifications of the circuit components and the performance of the circuit.

A.1. Field-Effect Transistor (FET)

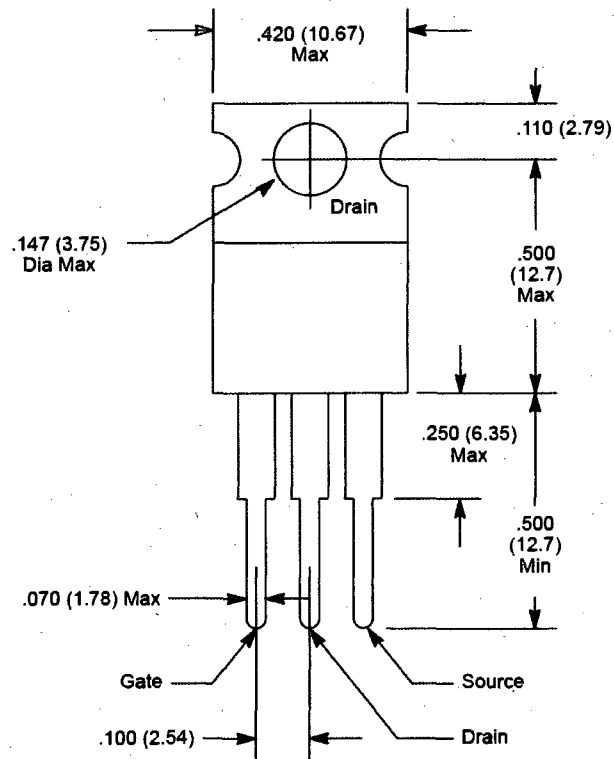


Figure A.1 A schematic of the MOSFET (NTE 2385).

FET is a kind of transistor, more frequently used than bipolar transistors when 1) very high input impedance, 2) a bidirectional analog switch, 3) a simple current source or 4) a voltage controlled resistance is required (Hayes et al. (1989)). In this study, the FET is used to build the bidirectional high speed analog switches. Among the various types of the FETs, n-channel enhancement metal-oxide-semiconductor field-effect transistor (MOSFET) is chosen for this application. Figure A.1 presents the shape and the detailed parts of the MOSFET (NTE, Model 2385: n-channel enhancement mode high speed switch with 23 ns rise time and 20 ns fall time). The MOSFET has three nodes which are gate, drain and source nodes. The source node is connected to a common ground (0 V) and the gate node receives gating/controlling signals. The voltage difference between the gate and the source nodes (V_{GS}) controls the current flowing from the drain to the source (I_D). I_D flows when V_{GS} exceeds a certain voltage level, particularly, in the case of n-channel enhancement MOSFET (e.g. V_{GS} should be lower than a value to activate a p-channel enhancement MOSFET). I_D can be varied primarily by V_{GS} , or partly by V_{DS} (voltage difference between the drain and the source) depending on the range of the voltages at the gate and drain nodes. Then the I_D can be transformed into a voltage signal by adding a resistor at the drain or the source node.

A.2. High Speed Switch Circuit

Figure A.2 shows the simple design of the high speed switch circuit. The gate and the drain nodes are connected to a DC power supply or pulse generators producing voltage pulses (e.g. 0 V – 5 V (gate) and 0 V – 20 V (drain) for the high speed switch circuit #2). When V_{GS} is 5 V, the circuit is activated and the current (I_D) flows from the drain to the source. Then V_{out} becomes a non-zero output voltage signal because the resistor added at the source causes voltage difference between the output (the source node) and the common ground. The resistance of the resistor placed at the source is varied to achieve designed voltage level of the output signal.

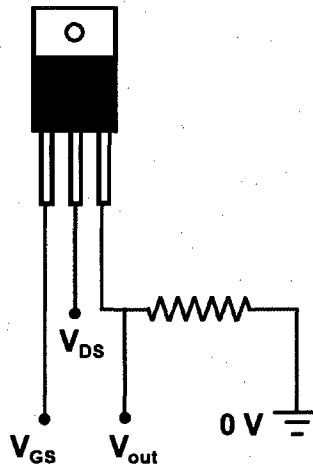


Figure A.2 A schematic of the high speed switching circuit.

The drain of the switch circuit #1 is connected to the 50 V DC power supply while a 9 ms width and 5 V pulse is provided to the gate node. The resulting output signal is the 50 V and 9 ms width voltage pulse for the high speed solenoid valve (see Section 2.2.3). In the switch circuit #2, 20 V, 50 kHz and 10 μ s width pulses are applied to the drain, and the 5 V, 50 kHz and 100 ns width pulses synchronized with the 20 V pulses are supplied to the gate node. The resulting output is the 20 V, 50 kHz and 100 ns width voltage pulses required for the plasma pulse generator (see Section 2.3). The switch circuit #3 selects one pulse from the pulse train applied to the gate of the switch circuit #2. The pulse train goes to the drain and a single pulse from the pressure sensor at the driven section of the expansion tube (see Section 2.4) transformed into a 5 V and 20 μ s width pulse is applied to the gate. Then the resulting output voltage pulse is a 5 V and 100 ns width pulse selected within the 20 μ s time period of the gate signal.

Appendix B Nanosecond Pulse Generator

In the current study, a nanosecond pulse generator (FID Technology, model F1112) is used to produce pulsed plasma discharges. A photograph of the pulse generator is presented in Fig. B.1. The output pulse width of the pulse generator is fixed at approximately 10 – 20 ns while the peak voltage and the repetition rate of the pulses are adjustable using a DC power supply (connected to port 1 in Fig. B.1) and a high speed switching circuit (connected to port 2, see Appendix A) producing trigger pulses of 20 V peak voltage and 100 ns pulse width operated by a pulse/delay generator, respectively. Approximately 150 V DC of the power supply corresponds to 15 kV peak voltage of the output pulses with the current experimental setup and conditions. The maximum allowable pulse repetition rate is 100 kHz although 50 kHz was set as the maximum frequency in this study for safety. An additional DC power supply providing 12 V DC (connected to port 3, the maximum current is set to be 4 A) operates the cooling system including four cooling fans attached below the circuit of the pulse generator. The two output ports (ports 4 and 5) of the pulse generator provide synchronized positive and negative nanosecond voltage pulses, respectively.

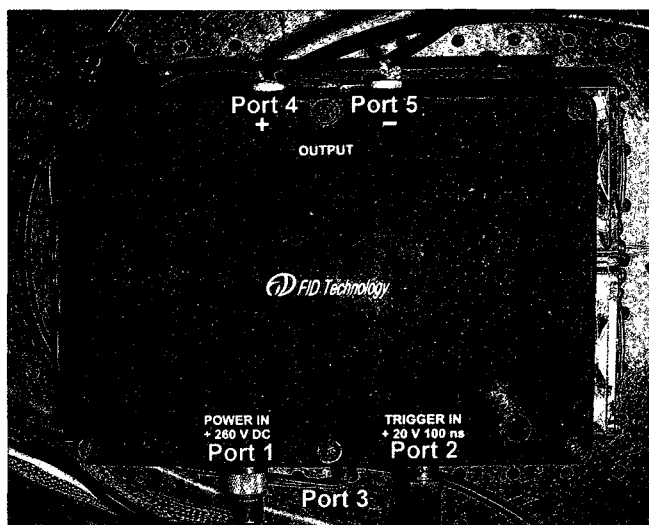


Figure B.1 A photograph of a high voltage nanosecond pulse generator (FID Technology, Model F1112).

Appendix C Electromagnetic Interference Shielding

One of the most difficult aspects of the experiment is protecting devices (e.g., computers, delay generators and solenoid valves) from electromagnetic interferences induced by the pulsed plasma. Two methods are used to block the electromagnetic interferences in this study, which are electrical insulation of the metallic parts of the expansion tube from the plasma devices and blocking the electromagnetic waves using metal (copper mesh and aluminum plate) cages.

Peak voltages measured on the test section surrounding the pulsed plasma is on the order of 10 V when the pulsed plasma is generated because it is the closest part of the expansion tube to the plasma receiving the electromagnetic waves. In addition, current leaking in the test section from high voltage cables, connected to electrodes generating the plasma, is observed. The voltage pulses originating from the test section subsequently travel through the metallic parts of the tube. The tube is grounded and electrically insulated utilizing dielectric materials (e.g., ceramic and wood) when a device is attached on the tube. Therefore, the tube acts as a Faraday cage.

Extra Faraday cages are used for further protection of devices vulnerable to the interferences such as solenoid valves. The Faraday cages are grounded metal boxes made of copper mesh and aluminum plates. The thickness of the plates facing the plasma discharge is 1 cm and the mesh size is 1 mm \times 1 mm. The cables in the vicinity of the test section are covered by aluminum foil and wound around by bare copper wires which are grounded. Figure C.1 shows a Faraday cage (protecting a high speed solenoid valve indicated by blue dotted rectangle in Fig. C.2), a ceramic plate for electrical insulation of the cage, a copper mesh and shielded cables.

Some devices (e.g., delay generators and high speed switching circuits) are often affected by the interferences despite the protection. Therefore, they are moved to another room (room 2 indicated by red dotted lines in Fig. C.2) separated by a concrete wall and a metal door. The cables from the room to the expansion tube are routed underneath the floor of the room (blue colored lines in Fig. C.2). The noisy

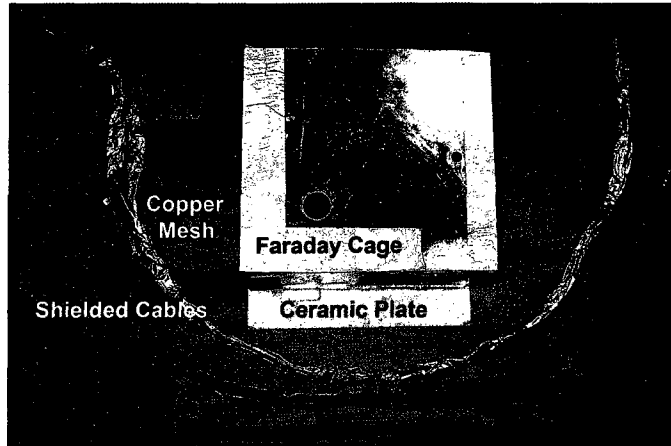


Figure C.1 A photograph of a Faraday cage, a ceramic plate, a copper mesh and shielded cables.

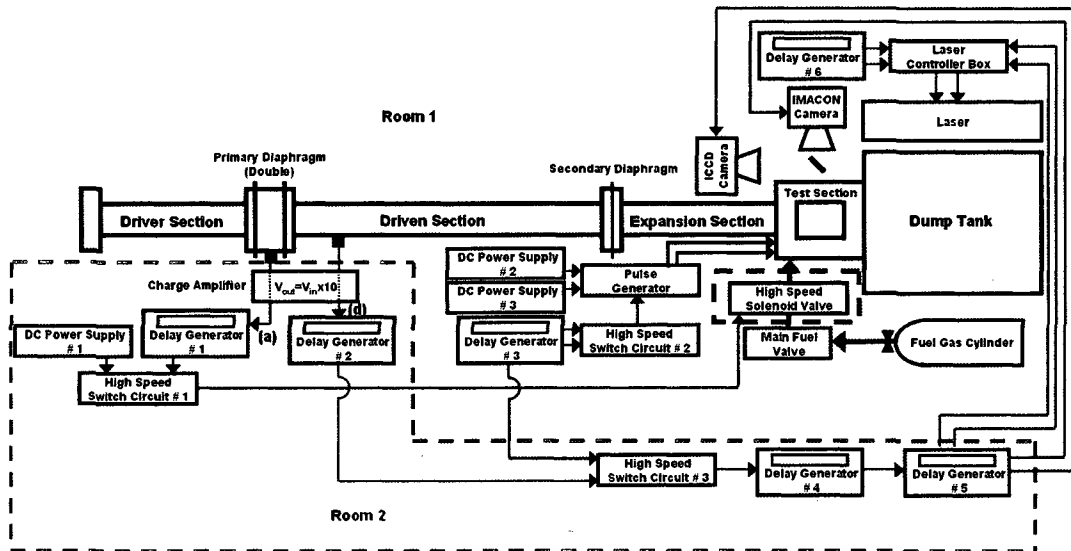


Figure C.2 A schematic of the fuel delivery system and the expansion tube synchronization system indicating the devices in a separate room (room 2) and cables (blue solid lines) underneath the floor.

signals from the expansion tube affected by the plasma become clean pulses selected by delay generators having adjusted voltage thresholds. These selected pulses are used as trigger signals for diagnostics devices.

List of References

- Adelgren, R. G., H. Yan, G. S. Elliott, D. D. Knight, A. A. Zheltovodov, and M. Ivanov (2003). Localized flow control by laser energy deposition applied to Edney IV shock impingement and intersecting shocks, *41st AIAA Aerospace Sciences Meeting and Exhibit*, Reno, NV.
- Alcock, J. L., L.C. Shirvill, and R.F. Cracknell (2001). Compilation of existing safety data on hydrogen and comparative fuels. Technical report of the European Community, *5th Framework Programme (1998-2002)*, contract no. ENK6-CT2000-00442.
- Anderson, C. D. and J. A. Schetz (2005). Liquid-fuel aeroramp injector for scramjets. *J. Propulsion and Power* 21, pp. 371 – 374.
- Andreadis D., A. Drake, J. L. Garrett, C. D. Gettinger, and S. S. Hoxie (2002). Design considerations of ISTAR hydrocarbon fueled combustor operating in air augmented rocket, ramjet and scramjet modes. *11th AIAA/AAF International Conference on Space Planes and Hypersonic Systems and Technologies*, Orleans, France.
- Bao, A., Y. G. Utkin, S. Keshav, G. Lou, and I. V. Adamovich (2007). Ignition of ethylene-air and methane-air flows by low-temperature repetitively pulsed nanosecond discharge plasma. *IEEE Trans. Plasma Sci.* 35, pp. 1628 – 1638.
- Ben-Yakar A. and R. K. Hanson (2001). Cavity flame-holders for ignition and flame stabilization in scramjets: an overview. *J. Propulsion and Power* 17, pp. 869 – 877.
- Biturin, V.A., I. B. Klementyeva, A. N. Bocharov, and A. I. Klimov (2007). Magnetically driven electrical discharges in high speed reacting flows for the MHD assisted mixing and combustion. *45th AIAA Aerospace Sciences Meeting and Exhibit*, Reno, NV, AIAA 2007-1024.

Boeuf, J. P., L. C. Pitchord, and W. L. Morgan (1996). SIGLO-KINEMA Software, BOLSIG. Available: <http://www.siglo-kinema.com/bolsig.htm>.

Boulos, M. I., P. Fauchais, and E. Pfender (1994). Thermal plasmas, volume 1. Plenum Press, NY.

Bozhenkov, S. A., S.M. Starikovskaia, and A.Yu. Starikovskii (2003). Nanosecond gas discharge ignition of H₂ and CH₄ containing mixtures. *Combust. Flame* 133, pp. 133 – 146.

Broadwell, J. E. and R. E. Breidenthal (1984). Structure and mixing of a transverse jet in incompressible flow. *Journal of Fluid Mechanics* 148, pp. 405 – 412.

Brown, M. S., R. A. Forlines, and B. N. Ganguly (2007). Filamentary pulsed-DC discharges in methane-containing mixtures. *45th AIAA Aerospace Sciences Meeting and Exhibit*, Reno, NV, AIAA 2007-823.

Bychkov, V. L., A. Yu. Lomteva, A. A. Kudryavtsev, E.A. Bogdanov, and A.L. Kuranov (2007) Air-hydrocarbon mixture ionization processes for optimization of ignition description. *45th AIAA Aerospace Sciences Meeting and Exhibit*, Reno, NV, AIAA 2007-1385.

Cathey, C. D., T. Tang, T. Shiraishi, T. Urushihara, A. Kuthi, and M. A. Gundersen (2007). Nanosecond plasma ignition for improved performance of an internal combustion engine. *IEEE Trans. Plasma Sci.* 35, pp 1664 – 1668.

Chung, S., C. C. Lin and E. T. P. Lee (1975). Dissociation of the hydrogen molecule by electron impact. *Phys. Rev. A* 12, pp 1340 – 1349.

Corrigan, S. J. B. (1965). Dissociation of molecular hydrogen by electron impact. *Journal of Chem. Phys.* 43, pp. 4381 – 4386.

Curran, E. T. (2001). Scramjet engines: the first forty years. *Journal of Propulsion and Power* 17, no. 6, pp. 1138 – 1148.

- Davies, W. R. and L. Berstein (1969). Heat transfer and transition to turbulence in the shock-induced boundary layer on a semi-infinite flat plat. *Journal of Fluid Mechanics* 36, pp. 87 – 112.
- Do, H., M. G. Mungal, and M. A. Cappelli (2008). Jet flame ignition in a supersonic crossflow using a pulsed nonequilibrium plasma discharge. *IEEE Trans. Plasma Sci.* 36, pp 2918 – 2923.
- Esakov, I. I., L. P. Grachev, K. V. Khodataev, V. A. Vinogradov, and D. M. Van Wie (2006). Propane–air mixture combustion assisted by MW discharge in a speedy airflow. *IEEE Trans. Plasma Sci.* 34, pp. 2497 – 2506.
- Fabela, J. L. T., J. O. Pacheco-Sotelo, M. P. Pacheco, J. S. Benítez-Read, R. López-Callejas, G. Zisis, and S. Bhosle (2007). Modeling the voltage drop across the cathode sheath in HPS. *IEEE Trans. Plasma Sci.* 35, pp. 1104 – 1110.
- Fang, T., M. Ding, and J. Zhou (2008). Supersonic flows over cavities. *Front. Energy Power Eng. China* 2(4), pp. 528 – 533.
- Fay J. E. and T. Rossmann (2006). Mixing measurements of transverse and oblique sonic jets in supersonic cross flow. *44th AIAA Aerospace Sci. Meeting and Exhibit*, Reno, NV, AIAA 2006-1230.
- Fons, J. T., J. S. Allen, R. S. Schappe, and C. C. Lin (1994). Production of electronically excited N_2^+ ions by electron impact on N_2 molecules. *Phys. Review A* 49, pp. 927 – 932.
- Gokulakrishnan, P., S. Pal, M. S. Klassen, A. J. Hamer, R. J. Roby, O. Kozaka, and S. Menon (2006). Supersonic combustion simulation of cavity-stabilized hydrocarbon flames using ethylene reduced kinetic mechanism. *42nd AIAA/ASME/SAE/ASEE Joint Propulsion Conference & Exhibit*, Sacramento, CA, AIAA 2006-5092.
- Goldfeld, M. A. and E. V. Orlik (2005). The research of laminar-turbulent transition in hypersonic three dimensional boundary layer. *J. Thermal Sci.* 14, no. 2, pp 103 – 107.

Goldfeld, M. A., S. S. Katsnelson, and G. A. Pozdnyakov (2007). Plasma initiation of the chemical reactions in a supersonic stream on the example of hydrogen and natural gas combustion reaction. *Proc. 8th Int. Symp. on Experimental and Computational Aerothermodynamics of Internal Flows*, Lyon, France, ISAI8-0016.

Gross, R. A. and W. Chinitz (1960). A study of supersonic combustion. *Journal Aerospace Sci.* 27, no. 7, pp. 517. – 524, 534.

Gruber, M. R., J. M. Donbar, C. D. Carter, and K. Y. Hsu (2004). Mixing and combustion studies using cavity-based flameholders in a supersonic flow. *J. Propulsion and Power* 20, pp. 769 – 778.

Hayakawa, A. and R. Goto (1941). On explosive reactions of gases, II. spark ignition of oxyhydrogen gas at low pressures. *Review of Phys. Chem. of Japan* 15f, no. 2, pp 117 – 125.

Helenbrook, B. T., H. G. Im, and C. K. Law (1998). Theory of radical-induced ignition of counterflowing hydrogen versus oxygen at high temperatures. *Combust. Flame* 112, pp. 242 – 252.

Heltsley, W. N., J. A. Snyder, A. J. Houle, D. F. Davidson, M. G. Mungal, and Ronald K (2006). Design and characterization of the Stanford 6 inch expansion tube. *42nd AIAA/ASME/SAE/ASEE Joint Propulsion Conf. and Exhibit*, Sacramento, CA, AIAA 2006-4443.

Heltsley, W. N., J. A. Snyder, C. C. Cheung, M. G. Mungal, and R. K. Hanson (2007). Combustion stability regimes of hydrogen jets in supersonic crossflow. *43rd AIAA/ASME/SAE/ASEE Joint Propulsion Conf. and Exhibit*, Cincinnati, OH, AIAA 2007-5401.

Jeong, E., S. O'Byrne, I. Jeung, and A. F. P. Houwing (2006). Cavity flame-holder experiments in a model scramjet engine. *14th AIAA/AHI Space Planes and Hypersonic Systems and Technologies Conference*, AIAA-2006-7918.

Kawai, S. and S. K. Lele (2007). Mechanisms of jet mixing in a supersonic crossflow: a study using large-eddy simulation. *Center for Turbulence Research Annual Research Briefs*, pp. 353 – 365.

Kazmar., R. R. (2005). Airbreathing hypersonic propulsion at Pratt & Whitney – overview. *AIAA/CIRA 13th International Space Planes and Hypersonics Systems and Technologies*, AIAA 2005-3256

Kim, K. M., S. W. Baek, and C. Y. Han (2004). Numerical study on supersonic combustion with cavity-based fuel injection. *International Journal of Heat and Mass Transfer* 47, pp. 271 – 286.

Kim, W., H. Do, M. G. Mungal, and M. A. Cappelli (2006). Flame Stabilization Enhancement and NO_x Production using Ultra Short Repetitively Pulsed Plasma Discharges. *44th AIAA Aerospace Sciences Meeting and Exhibit*, Reno, NV, AIAA 2006-560.

Kim, W., H. Do, M. G. Mungal, and M. A. Cappelli (2006). Plasma-discharge stabilization of jet diffusion flames. *IEEE Trans. Plasma Sci.* 34, pp. 2545 – 2551.

Kim, W., H. Do, M. G. Mungal, and M. A. Cappelli (2007). Investigation of NO production and flame structure in plasma enhanced premixed combustion. *Proc. Combust. Inst.* 31, pp 3319 – 3326.

Kim, W., H. Do, M. G. Mungal, and M. A. Cappelli (2008). Optimal discharge placement in plasma-assisted combustion of a methane jet in cross flow. *Combust. Flame* 153, pp 603 – 615.

Kim, W., M. G. Mungal and M. A. Cappelli (2008). Formation and role of cool flames in plasma-assisted premixed combustion. *App. Phys. Lett.* 92, 051503

Knight, D. D., Y. F. Kolesnichenko, V. Brovkin, and D. Khmara (2007). High speed flow control using microwave energy deposition. *16th Australasian Fluid Mechanics Conference*, Gold Coast, Queensland, Australia.

- Leonov, S. B., D. A. Yarantsev, A. P. Napartovich, and I. V. Kochetov (2006). Plasma-assisted combustion of gaseous fuel in supersonic duct. *IEEE Trans. Plasma Sci.* 34, pp. 2514-2525.
- Li, J., Z. Zhao, A. Kazakov, and F. L. Dryer (2004). An updated comprehensive kinetic model of hydrogen combustion. *International Journal of Chemical Kinetics* 36, pp. 566-575.
- Lin, K, C. Tam, I. Boxx, C. Carter, K. Jackson, and M. Lindsey (2007). Flame characteristics and fuel entrainment inside a cavity flame holder in a scramjet combustor. *43rd AIAA/ASME/SAE/ASEE Joint Propulsion Conference and Exhibit*, Cincinnati, OH, AIAA 2007-5381.
- Liu, J., F. Wang, G. Li, A. Kuthi, E. J. Gutmark, P. D. Ronney, and M. A. Gundersen (2005). T Transient plasma ignition. *IEEE Trans. Plasma Sci.* 33, pp 326 – 327.
- Longmire, E. K. AND J. K. Eaton (1992). Structure of a particle-laden round jet. *J. Fluid Mech.* 236, pp. 217-257.
- Lutz, M. A. (1973). The Glow to arc transition - a critical review. Technical report from Hughes Research Laboratories.
- Macheret, S. O., M. N. Shneider, and R. B. Miles (2002). Modeling of air plasma generation by repetitive high-voltage nanosecond pulses. *IEEE Trans. Plasma Sci.* 30, pp 1301 – 1314.
- Maddalena, L., T. L. Campioli, and J. A. Schetz (2005). Experimental and computational investigation of an aeroramp injector in a mach four cross flow. *AIAA/CIRA 13rd Int. Space Planes and Hypersonics Systems and Tech. Conf.*, Capua, Italy, AIAA-2005-3235.
- Mintoussov, E. I., A. A. Nikipelov, S. S. Starikovskaia, and A. Yu. Starikovskii (2006). Liquid fuel atomization and heterogeneous combustion of fuel-oxidizer

mixtures using nanosecond discharge. *44th AIAA Aerospace Sciences Meeting and Exhibit*, Reno, NV, AIAA-2006-614.

Morsy, M. H., Y. S. Ko, and S. H. Chung (1999). Laser-induced ignition using a conical cavity in CH₄-air mixtures. *Combust. Flame* 119, pp. 473 – 482.

Naidis, G. V. (1997). Modelling of plasma chemical processes in pulsed corona discharges. *J. Phys. D: Appl. Phys.* 30, pp. 1214 – 1218.

Pancheshnyi, S. V., D. A. Lacoste, A. Bourdon, and C. O. Laux (2006). Ignition of propane-air mixtures by a repetitively pulsed nanosecond discharge,” *IEEE Trans. Plasma Sci.* 34, pp. 2478 – 2487.

Penetrante, B. M., M. C. Hsiao, B. T. Merritt, G. E. Vogtlin, P. H. Wallman, M. Neiger, O. Wolf, T. Hammer, and S. Broer. (1996). Pulsed corona and dielectric-barrier discharge processing of NO in N₂. *Appl. Phys. Lett.* 68 (26), pp. 3719-3721.

Pilla, G. P., D. Galley, D. A. Lacoste, F. Lacas, D. Veynante, and C. O. Laux (2006). Stabilization of a turbulent premixed flame using a nanosecond repetitively pulsed plasma. *IEEE Trans. Plasma Sci.* 34, pp 2471 – 2477.

Popov, N. A. and I. A. Kossyi (2007). Effect of nonequilibrium excitation of hydrogen-oxygen mixture on ignition. *45th AIAA Aerospace Sciences Meeting and Exhibit*, Reno, NV, AIAA-2007-1031

Rasmussen, C. C., J. F. Driscoll, C. D. Carter, and K. Y. Hsu (2005). Characteristics of cavity-stabilized flames in a supersonic flow. *J. Propulsion and Power* 21, pp. 765 – 768.

Rogers, R. C., D. P. Capriotti, and R. W. Guy (1998). Experimental supersonic combustion research at NASA Langley. *20th AIAA Advanced Measurement and Ground Testing Tech. Conf.*, Albuquerque, NM, AIAA-98-2506.

- Roudakov, A. S., V. L. Semenov, V. I. Kopchenov, and J. W. Hicks (1996). Future flight test plans of an axisymmetric hydrogen-fueled scramjet engine on the hypersonic flying laboratory. *7th International Spaceplanes and Hypersonics Systems & Technology Conference*, Norfolk, Virginia, AIAA 96-4572
- Roy, M. (1959). Supersonic propulsion by turbojets and by ramjets. *Advances in Aeronautical Sciences* 1, p. 112.
- Satheesh, K. and G. Jagadeesh (2007). Effect of concentrated energy deposition on the aerodynamic drag of a blunt body in hypersonic flow. *Physics of Fluids* 19, 031701.
- Settles, G. S. (2006). Schlieren & shadowgraph techniques. Springer-Verlag, Berlin, Heidelberg, and New York.
- Smith, S. H. and M. G. Mungal (1998). Mixing, structure and scaling of the jet in crossflow. *Journal of Fluid Mechanics* 357, pp. 83 – 122.
- Starikovskaia, S. M. (2006). Plasma assisted ignition and combustion. *J. Phys. D: Appl. Phys.* 39, pp. R265–R299.
- Starikovskii, A. Yu. (2004). Plasma supported combustion. *Proc. 30th Int. Symp. Combust.*, p. 326.
- Stiesch, G. (2003). Modeling engine spray and combustion processes. Springer, New York, NY.
- Varey, R. H., J. Smalley, P. H. Richards, C. F. Gozna and D. T. Swift-hook (1971). Molecular dissociation in a constricted glow discharge. *J. Phys. D: Appl. Phys.* 4, pp. 1520 – 1526.
- Vincent-Randonnier, A., S. Larigaldie, P. Magre and V. Sabel'nikov (2007). Plasma assisted combustion: effect of a coaxial DBD on a methane diffusion flame. *Plasma Sources Sci. Technol.* 16, pp. 149–160.

Vroom, D. A. and F. J. de Heer (1969). Production of excited atoms by impact of fast electrons on molecular hydrogen and deuterium. *Journal of Chem. Phys.* 50, pp. 580 – 590.

Waltrup, P. J. (1992). Airbreathing propulsion for missile and projectiles. AGARD-CP-526, Paper 8.

Wronski, Z. (2005). Dissociation of nitrogen in the plasma-cathode interface of glow discharges. *Vacuum* 78, pp. 641–647.

Zhukov, V.P., A.E. Rakitin, and A.Yu. Starikovskii (2007). Detonation initiation by high-voltage pulsed discharges. *45th AIAA Aerospace Sciences Meeting and Exhibit*, Reno, NV, AIAA 2007-1029.